Ultracold Fermi Gas with Repulsive Interactions

ARCHIVES
MASSACHUSETTS INSTITUTE OF TECHNOLOGY
APR [illegible]
LIBRARIES

by

Ye-Ryoung Lee

Submitted to the Department of Physics
in partial fulfillment of the requirements for the degree of

Doctor of Philosophy

at the

MASSACHUSETTS INSTITUTE OF TECHNOLOGY

September 2012

© Massachusetts Institute of Technology 2012. All rights reserved.

Author ....
Department of Physics
August 10, 2012

Certified by ....
Wolfgang Ketterle
John D. MacAurthur Professor of Physics
Thesis Supervisor

Accepted by ....
John Belcher
Professor of Physics, Associate Department Head for Education

Ultracold Fermi Gas with Repulsive Interactions

by

Ye-Ryoung Lee

Submitted to the Department of Physics
on August 10, 2012, in partial fulfillment of the
requirements for the degree of
Doctor of Philosophy

Abstract

This thesis presents results from experiments of ultracold atomic Fermi gases with repulsive interaction.

Itinerant ferromagnetism was studied by simulating the Stoner model with a strongly interacting Fermi gas of ultracold atoms. We observed nonmonotonic behavior of lifetime, kinetic energy, and size for increasing repulsive interactions, which is in good agreement with a mean-field model for the ferromagnetic phase transition. However, later research showed the absence of enhanced spin fluctuation, which is definitive evidence against the ferromagnetic phase transition. Still, our work triggered a lot of research on repulsive interactions in ultracold Fermi gases.

A quantitative approach is taken to study ultracold Fermi gases with repulsive interaction. This is done by careful measurements of density profiles in equilibrium. First, Pauli paramagnetism is observed in trapped atomic samples which have an inhomogeneous density due to the harmonic confinement potential. We experimentally measure the susceptibility of ideal Fermi gas. This research shows that ultracold atoms can serve as model systems to demonstrate well-known textbook physics in a more ideal way than other systems. Then, Fermi gases with repulsive interactions are characterized by measuring their compressibility as a function of interaction strength. The compressibility is obtained from in-trap density distributions monitored by phase contrast imaging. For interaction parameters $k_F a > 0.25$ fast decay of the gas prevents the observation of equilibrium profiles. For smaller interaction parameters, the results are adequately described by first-order perturbation theory. A novel phase contrast imaging method compensates for dispersive distortions of the images.

Thesis Supervisor: Wolfgang Ketterle
Title: John D. MacAurthur Professor of Physics

To my Lord, Jesus
my love, Kyeong-Jae
and my dearest family

Acknowledgments

"For I know the plans I have for you" declares the Lord,
"plans to prosper you and not to harm you, plans to give you hope and a future.
Then you will call on me and come and pray to me, and I will listen to you.
You will seek me and find me when you seek me with all your heart.
I will be found by you" declares the Lord...
Jeremiah 29:11-14

Thank you Jesus, my joy and my strength.

First, I sincerely thank my advisors, Wolfgang and Dave. Your advice and support has made this work possible. Thank you for giving me this research opportunity. I thank Wolfgang for his dedication, passion, patience, and continuous encouragement and support. You are truly the best at providing direction and motivation. I thank Dave for his enthusiasm and passion for physics. This has always been a source of inspiration to me. I have learned a great deal from both of you.

I am thankful that I shared the lab with great people.

It was such a blessing to work with Myoung-Sun during the last phase of my study. His understanding of physics and calm and diligent personality encouraged me a lot and helped me finally exit the revolving door.

Tout joined the group 3 years later than I joined. It was great to have an extremely energetic and enthusiastic lab mate. I thank him for bringing energy to the lab and also for his kindness, warm heart, patience, endless curiosity and optimism.

I have started grad school at the same time as Caleb. I am thankful that I had such a nice friend as a lab mate. It was very comforting to have shared most of my journey with Caleb, who is always calm and nice.

I thank Jae for helping me get through some hard times. His encouragement and advice was a source of support. I shared great time in the lab at nights enjoying discussion with him about physics and life.

My first physics project in the lab was the ferromagnetism project with Gyu-boong. His enthusiasm for physics and his diligence inspired me. I thank him for supporting me joining this amazing group and guiding me through.

I thank Timur for bringing new energy into our team with his relaxed attitude and charming personality. I was always amazed by Tonys ability to accomplish any tasks perfectly. I am confident that he will go on to do amazing research. I also thank Gregory for experimental assistance. I would also like to thank all past members of BEC3 including Tom, Sebastian, and Michele.

Yong has been a mentor for me throughout my time in MIT. He not only answered all my physics questions, but also provided guidance regarding all my concerns in and outside the lab. I truly admire his intelligence, enthusiasm for physics, wisdom, generosity, and diligence.

Andre, or in short An, was my office mate when I first joined Ketterle group. We became close friends since. He was always there to give comforting conversation whenever I had hard time at MIT. My life in the lab was enriched and brightened by our friendship.

Whenever I needed help desperately at late nights in the lab, Christian was always there to willingly share his wisdom. I really appreciated your help.

I thank Jongchul for his constant encouragement and support. He was kind enough to lend his time and help out with any questions that I had. Thank you for all the fun times we had outside the lab.

I thank all the other people in the hallway for always being kind and helpful friends. I thank BEC1 including Ariel, Mark, and Christian for sharing nights in the lab over the curtain with loud music and Feshbach field interference. I thank BEC2, including Aviv, Ed, Jon, Jit kee, Yingmei, and Dan for providing all the equipments and technical advices. I thank BEC4, Fermi1, and Vladans group including Hiro, David, Patrick, Gretchen, Chen, Jeewoo, Peyman, Vladan, Monika, Haruka, Ian, and Marko for their support. I also thank Joanna for her assistance and smiles.

Outside the lab, I express my gratitude to Beacon City Church and all my friends at MIT and Harvard. I also thank my friends back in Korea.

I would like to thank my family, who has always loved, supported, and believed in me. Without them, I would not be where I am today. I love you all very much.

I am deeply blessed to be a child of my parents, Seunghee and Insun, and to be a sister of Ye-Eun. I am secure because I know that they are always there to pour out endless love, comfort and encouragement. Thank you for being the best parents in the world who I respect the most, and for being the best sister whom I am so proud of. I would also like to thank my in laws, Jong-Kun, Soyeon, and Seong-Jae for their love, support, and prayer. Your encouragement was truly meaningful to me.

Finally, I give my special thanks to my husband, my guardian angel and my best friend, Kyeong-Jae. Without his prayer, support, caring, understanding, sacrifice, patience, comforts, and love, I would never have completed this thesis. I am so thankful to have shared 6 years at MIT with you. I must be the luckiest person because you are my husband! I love you with all my heart.

Contents

1 Introduction **17**

1.1 Ultracold Fermi Gases 17

1.1.1 Ultracold Atomic Gases 17

1.1.2 Quantum Simulator 18

1.2 Repulsive Interaction 19

1.3 Equation of States 21

1.4 Experiment 22

2 Quantum Statistical Mechanics for Ultracold Fermi Gases **25**

2.1 Bosons and Fermions 25

2.2 Quantum Statistical Mechanics for Boson and Fermion 26

2.3 Fermi gases in a harmonic trap 28

2.4 Interaction Effect : Perturbation limit 28

3 Itinerant Ferromagnetism in a Fermi Gas of Ultracold Atoms **31**

3.1 Itinerant Ferromagnetism and Stoner Model 31

3.2 Experimental Procedure 34

3.3 Itinerant Ferromagnetism in a Fermi Gas of Ultracold Atoms 36

3.4 Further Development 40

4 Pauli Paramagnetism in an Ideal Fermi Gas **41**

4.1 Pauli Paramagnetism: Ultracold Atomic Gas vs Solid State System . 42

4.2 Experimental Procedure 47

4.3 Susceptibility Measurement 49
4.4 Susceptibility Measurement in Systems with Interaction 53

5 Compressibility of an Ultracold Fermi Gas with Repulsive Interactions 55
5.1 Experimental Procedure 57
5.2 Loss Rate 57
5.2.1 Loss Rate Estimation 57
5.2.2 Loss Rate Measurement 58
5.3 Compressibility Measurement 58
5.3.1 Measurement Method 60
5.3.2 Temperature Measurement 62
5.3.3 Interaction Effect 63
5.4 Dispersive Effect in Phase-Contrast Imaging 65
5.4.1 Phase-Contrast Imaging 66
5.4.2 Compensation for Dispersive Effect 66
5.4.3 Imaging Focus Fine Tuning 69
5.5 Discussion 69
5.5.1 Molecular Fraction in the Density Profile 69
5.5.2 Interaction Strength Limitation 71
5.5.3 Outlook 72

6 Conclusion 73

A Tips for Precise Imaging 75
A.1 Imaging Beam Intensity 75

B Exact Breit-Rabi Formula for the Ground States of ^{6}Li 77

C RF Antenna in BEC3's Main Chamber 79

D Itinerant Ferromagnetism in a Fermi Gas of Ultracold Atoms 81

E Compressibility of an Ultracold Fermi Gas with Repulsive Interactions 87

List of Figures

1-1 Feshbach resonance in ^{6}Li between the two lowest hyperfine states $|F = 1/2; m_F = 1/2\rangle$ and $|F = 1/2; m_F = -1/2\rangle$ 20
1-2 ^{6}Li hyperfine structure 22

3-1 Simple mean-field model of a two-component Fermi gas 33
3-2 Mean-field prediction of ferromagnetism 34
3-3 The experimental procedure 35
3-4 Atom loss rate 37
3-5 Kinetic energy measurement 38
3-6 Cloud size and molecular fraction 39

4-1 Comparison between a free electron gas and two-component Fermi gases in the study of magnetism 43
4-2 Comparison between a free electron gas and two-component Fermi gases trapped in the spherical harmonic trapping potential 46
4-3 Simulated density profiles of two-component Fermi gases in a spherical harmonic trap at zero temperature 48
4-4 Double-shutter phase contrast imaging with two different imaging frequencies 49
4-5 Experimentally obtained density profiles 51
4-6 Susceptibility at high magnetic field 52

5-1 Characterizing atomic loss for increasing repulsive interactions 59

5-2 Determination of the compressibility of repulsively interacting Fermi gases 61
5-3 Measured temperature, normalized compressibility, and interaction effect on compressibility at various interaction strengths 64
5-4 Phase-contrast imaging of a balanced spin mixture in states $|1\rangle$ and $|2\rangle$ 67
5-5 Dispersion effect in phase-contrast imaging 68
5-6 Imaging Focus Fine Tuning. 70

C-1 Dimensions of RF antenna in BEC3's main chamber 79

List of Tables

4.1 Comparison between a free electron gas and two-component Fermi gases in the study of magnetism 42

B.1 Constants for ^{6}Li Breit-Rabi formula 77

Chapter 1

Introduction

1.1 Ultracold Fermi Gases

1.1.1 Ultracold Atomic Gases

At very low temperature where the quantum coherence length is comparable to the inter-particle distance, particles obey quantum statistics. In quantum statistics, there are two kinds of particle: bosons and fermions. Bosons follow the Bose-Einstein statistics, and fermions follow the Fermi statistics.

According to Bose-Einstein statistics, a large fraction of the bosons occupy the lowest energy level at very low temperature. This state of matter is called Bose-Einstein condensate (BEC), and it was first predicted by Satyendra N. Bose and Albert Einstein in 1924 [9, 21]. The first experimental realization of Bose-Einstein condensate was achieved in 1995 [2, 16]. This was done by cooling ultracold dilute atomic gases of ^{87}Rb [2] and ^{23}Na [16] to less than 1 μK above the absolute zero temperature. The cooling was done by using laser cooling and magnetic trapping techniques [20, 33].

The achievement of Bose-Einstein condensate in ultracold atoms not only enabled the exciting researches on Bose-Einstein itself [1, 6, 7, 41, 42, 56], but also enabled achieving the quantum degenerate Fermi gases [17].

Experiments with ultracold Fermi gases have explored many-body physics with strong interactions using Feshbach resonance or optical lattices. They have demonstrated long-predicted phenomena like the BEC-BCS crossover [34] and Lee-Huang-Yang corrections to the energy of degenerate gases [46, 47, 62]. Experiments have also explored novel quantum phases like fermions with unitarity limited interactions [34, 36], population imbalanced Fermi gases [48, 75] and Hubbard models in optical lattices [8, 23].

1.1.2 Quantum Simulator

Novel quantum materials such as high temperature superconductors, graphenes, and colossal magneto-resistance materials are considered as potential driving force behind further development of technology. Even though understanding the physics behind these materials is crucial for improving their properties and developing applications, it is very difficult because of complexity in strongly interacting many-electron systems. Theoretical studies suggests simple model systems in order to explain the physics, but these systems cannot be verified directly by experiment on existing materials. In addition, synthesizing new materials mimicking the simple models is based on trial and error approaches.

Experiments using ultracold atomic gases are a new approaches to solve this problem. Using the tools and precision of atomic physics, ultracold atomic samples can be prepared to realize simple Hamiltonians. This concept of quantum simulator was first proposed by Richard Feynman [22]. The main benefit of experiments with ultracold atoms is the controllability. The density of atoms can be varied over three orders of magnitude. The atoms can be prepared in different hyperfine states, which in turn can represent different spin states of electrons. The trapping potential to hold the atomic gases can be manipulated and controlled easily, so that various lattice structures can be produced using optical lattices. The atomic sample is extremely pure unlike the materials containing impurities or defects used in condensed matter experiments. The interactions can be controlled using well understood Feshbach resonances. Usually, interactions in ultracold gases are fully described by the scattering length, which is a zero-range approximation greatly simplifying the theoretical description.

This approximation is valid since the diluteness of the atomic gases implies a particle separation much larger than the short range of the van-der-Waals interactions. This almost exact characterization of the interactions by a single parameter, the tunability of interaction strength, and precise experimental control over cold atoms systems have made them an ideal testbed for many-body quantum calculations.

In this thesis, this controllability of ultracold atoms is used to simulate the simple model system of ferromagnetism, the textbook model system of free electron gas with and without interaction.

1.2 Repulsive Interaction

The important recent developments in cold atom science reviewed in section 1.1.1 were realized in Fermi gases with strong attractive interactions. Fermi gases with repulsive interactions didn't capture much attention mainly because they are unstable against three-body recombination into weakly-bound molecules [52]. Nevertheless, fermions with repulsive interactions have been the focus of much recent work due to the prediction of a phase transition to a ferromagnetic state for sufficiently strong interactions [5, 19, 37, 66, 71]. Motivated by these predictions, experimental researches on fermions with repulsive interactions were done, and they are presented in this thesis.

As in Fig. 1-1, a Feshbach resonance couples a molecular bound state with an unbound state of two free atoms. A magnetic field changes the energies of two free atoms relative to the molecular state and thereby controls the interatomic interaction strength. The experiment with attractive interaction has been done on the ground state branch (or so-called lower branch) in Fig. 1-1(b). The fermi gases with repulsive interaction are realized on the the first excited branch (or so-called upper branch) of a Feshbach resonance where decay is always possible into the lower branch which consists of weakly bound molecular states with binding energy $\hbar^2/ma^2$ with a being the scattering length. The molecules are formed through three-body collisions, and the collision rate is proportional to $n^2a^6\max(T, T_F) = (k_Fa)^6n^{2/3}$ [18, 52].

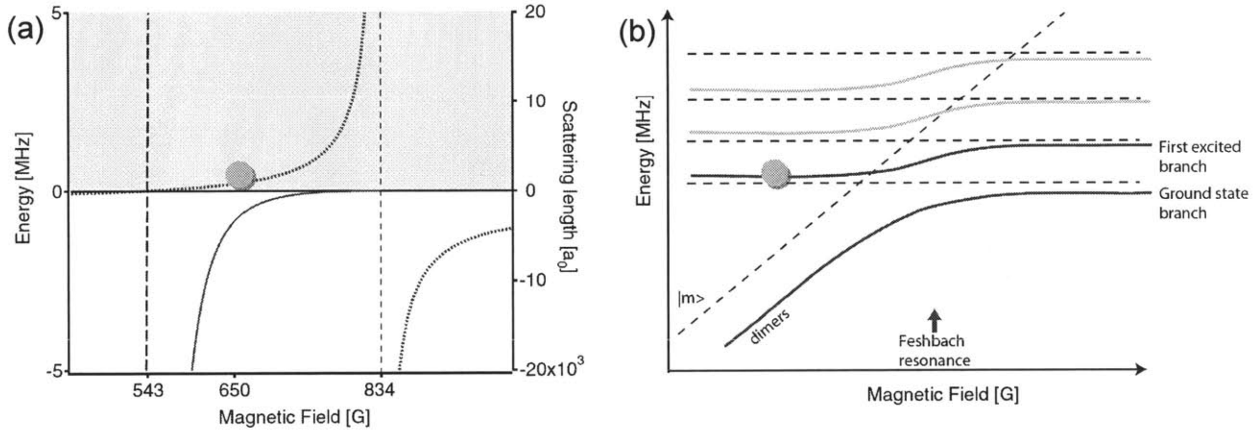

Figure 1-1: Feshbach resonance in ^{6}Li between the two lowest hyperfine states $|F=1/2; m_F=1/2\rangle$ and $|F=1/2; m_F=-1/2\rangle$.(a) The red line shows the molecular binding energy, and the blue dash lines show the scattering length. (b) The blue line below the Feshbach resonance represents the excited state where the interaction is repulsive.

1.3 Equation of States

A system is characterized by its equation of state. The equation of state can be expressed in different forms involving various thermodynamic variables including density, energy, pressure, temperature and entropy. For cold atom experiments, density, chemical potential (through the trapping potential) and temperature are directly accessible to measurement.

In the first thermodynamic studies of ultracold Fermi gases, the thermodynamic quantities of the whole trapped gas was measured. The trapping potential induces inhomogeneity in ultracold experiments while most theoretical calculations assumes homogeneous systems. Thus, the comparison between experiments and theoretical calculations require integral over the whole trap. Integration smoothes sharp features, so that it could conceal evidences of phase transitions and make different theoretical predictions indistinguishable.

However, using local density approximation, the ultracold gas can be locally described as a homogeneous gas. That is, each local point in the gas can be considered as homogeneous systems with different conditions. Therefore, the inhomogeneity problem in ultracold experiments can be resolved by accurate measurement of the thermodynamic variables at each point in the trap.

This new level of quantitative comparison between theory and experiment was recently reached by careful measurements of density profiles from which the equation of state could be determined. These techniques were first proposed by Chevy [12] and Bulgac [10] and implemented by Shin [61]. Further improvements [27, 28, 36, 44–46] resulted in impressive accuracy without adjustable parameters. These results hinge on accurate measurements of the equilibrium atomic density distribution. In this thesis, we extend these work to ultracold Fermi gases with repulsive interaction. In addition, we use ultracold Fermi gases as model systems to demonstrate well-known textbook physics of free electron gas in a more ideal way than other systems.

1.4 Experiment

The details on the experimental setup and production of a strongly interacting degenerate gas of ^{6}Li can be found in Ref. [25, 34]. The design and construction of our apparatus is thoroughly described in Ref. [13]. The most recent upgrade to from BEC apparatus to Bose-Fermi mixture apparatus has been reviewed in Ref. [14, 30]. Here, we will only briefly review the procedure.

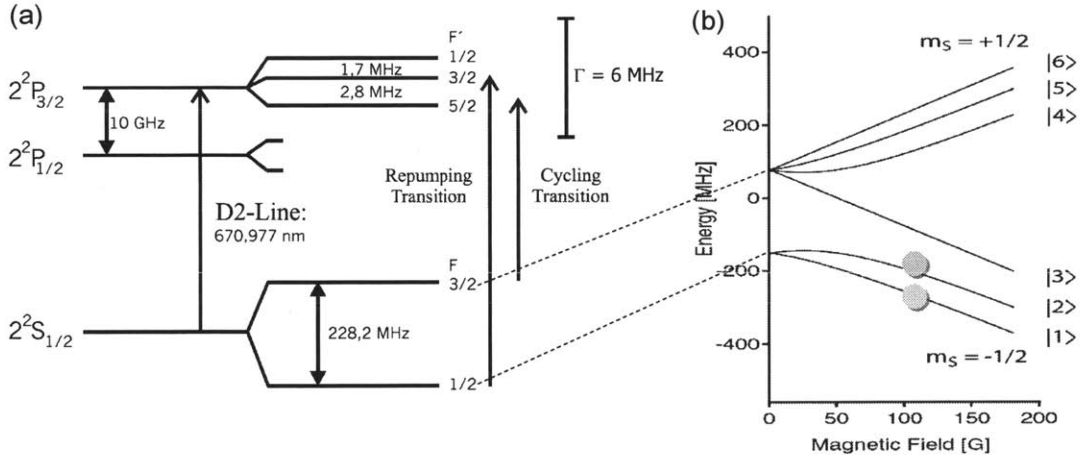
(a)
$2^2P_{3/2}$
$2^2P_{1/2}$
$2^2S_{1/2}$
10 GHz
F'
1/2
3/2
5/2
1,7 MHz
2,8 MHz
Γ = 6 MHz
Repumping Transition
Cycling Transition
D2-Line:
670,977 nm
F
3/2
1/2
228,2 MHz
(b)
$m_S = +1/2$
$m_S = -1/2$
|6>
|5>
|4>
|3>
|2>
|1>
Energy [MHz]
400
200
0
-200
-400
0
50
100
150
200
Magnetic Field [G]

Figure 1-2: ^{6}Li hyperfine structure. (a) Energy level diagram for laser cooling. (b)A repulsive two-component Fermi gas is prepared in the two lowest hyperfine states, $|1\rangle$ and $|2\rangle$ states (corresponding to the $|F = 1/2; m_F = 1/2\rangle$ and $|F = 1/2; m_F = -1/2\rangle$).

An atomic vapor is created in an heated oven containing solid ^{23}Na, a boson, and ^{6}Li, a fermion. This two-species atomic vapor is collimated by a nozzle and a collimation aperture. A Zeeman slower is used to slow down the thermal atomic beam, and the slowed atomic beam is loaded into a dual species Magneto-Optical Trap (MOT). In order to avoid spin-exchange collisions causing unwanted heating, ^{23}Na and

^{6}Li atoms are optically pumped into their respective stretched states, $|F = 2; m_F = 2\rangle$ and $|F = 3/2; m_F = 3/2\rangle$, and they are microwave swept in the presence of bias field for purification. The atoms are loaded into a magnetic trap of the Ioffe-Pritchard type. Evaporative cooling of ^{23}Na using microwave sweep leads to sympathetic cooling of ^{6}Li. At this point, we routinely produce a spin-polarized Fermi gas of $\sim 5 \times 10^6$ atoms in the stretched state of $|F = 3/2; m_F = 3/2\rangle$, and ^{23}Na atoms are fully evaporated. The typical temperature of the sympathetic cooled ^{6}Li is T $\sim 0.5 T_F$ where T_F is the Fermi temperature.

The ^{6}Li atoms are then loaded into a single-beam optical dipole trap and transferred into the lowest hyperfine state $|F = 1/2; m_F = 1/2\rangle$ by a Landau-Zener radio-frequency (RF) sweep. Additional axial confinement is provided by magnetic field curvature. A desired population mixture of $|1\rangle$ and $|2\rangle$ spin states (corresponding to the $|F = 1/2; m_F = 1/2\rangle$ and $|F = 1/2; m_F = -1/2\rangle$ states at low magnetic field) is prepared by a Landau-Zener RF sweep at 300 G, followed by 500 ms wait time for decoherence and evaporative cooling in the optical trap. The Feshbach resonance at 834 G [34] is used to tune the repulsive interactions between $|1\rangle$ and $|2\rangle$. We increase the magnetic field in 200 ms to 528 G, where the scattering length is zero and our Fermi gas is non-interacting. The final trap has a depth of 4.1 μK and frequencies of $\omega_x = \omega_y =$ 390 Hz and $\omega_z =$ 34.7 Hz. The number of atoms per spin state is 8×10^5, which corresponds to a Fermi temperature T_F of 1.4 μK. Note that the experiment presented in chapter 3 was done in slightly different configuration. The mixture preparation of $|1\rangle$ and $|2\rangle$ spin states was done at 590 G instead of 300G, and the magnetic field was lowered to 300 G for decoherence. The wait time for decoherence was 1 s, and the field was ramped up back to 590 G. The final trap has a depth of 7.1 μK and frequencies of $\omega_x = \omega_y \simeq 300$ Hz and $\omega_z \simeq 70$ Hz.

Chapter 2

Quantum Statistical Mechanics for Ultracold Fermi Gases

2.1 Bosons and Fermions

In classical mechanics, we can always distinguish particles under physical observation and measurements. In quantum mechanics, particles can be indistinguishable because a detective's observations inevitably and unpredictably alter the state. This feature of quantum mechanics determines two kinds of fundamental particles: bosons and fermions.

Let us consider a collection of N indistinguishable particles. The wave function $\psi(r_1, r_2, .., r_N)$ represents the probability amplitude for finding N particles at the position of $r_1, r_2, .., r_N$. Since particles are indistinguishable, exchange of any pair of particles keeps the probability density invariant:

$$| \psi(r_1, .., r_i, .., r_j, .., r_N) |^2 = | \psi(r_1, .., r_j, .., r_i, .., r_N) |^2. \tag{2.1}$$

This results in two degenerate wave functions under particle exchange.

$$\psi(r_1, .., r_i, .., r_j, .., r_N) = \pm\psi(r_1, .., r_j, .., r_i, .., r_N) \tag{2.2}$$

For simplicity, let us consider two identical particles. Suppose $\psi_a(r_1)\psi_b(r_2)$ and $\psi_b(r_1)\psi_a(r_2)$ are two eigenstates of the two-particle system we consider. Then, the two wave functions satisfying Eq. 2.1 are

$$\psi_\pm(r_1, r_2) = A[\psi_a(r_1)\psi_b(r_2) \pm \psi_b(r_1)\psi_a(r_2)]. \tag{2.3}$$

These two wave functions represent bosons (symmetric wave function, ψ_+) and fermions (antisymmetric wave function, ψ_-). All particles with integer spin are bosons, and these particles obey Bose-Einstein statistics. All particles with half-integer spin are fermions, and these particles obey Fermi-Dirac Statistics. One characteristic of fermions is that they cannot occupy the same state, the famous "Pauli's exclusion principle." If $\psi_a = \psi_b$ in Eq. 2.3, $\psi_- = 0$. That is, probability of two identical fermions occupying the same state is zero.

2.2 Quantum Statistical Mechanics for Boson and Fermion

In grand canonical ensemble, the probability that the system is in any state with particle number N and energy E_{tot} is given by the Boltzmann factor $e^{-(E_{tot}-\mu N)/k_BT}$.

Let us consider a non-interacting many-particle system with single-particle energy E_i and n_i particles in energy state E_i. The grand canonical partition function Z for this system is then

$$Z = \sum_{n_i} \prod_i e^{-n_i(E_i-\mu)/k_BT}. \tag{2.4}$$

The average occupation number of state i is then

$$\langle n_i \rangle = k_BT\frac{\partial \ln Z}{\partial \mu} = \frac{1}{e^{(E_i-\mu)/k_BT} \mp 1} \tag{2.5}$$

with the upper sign corresponding to bosons, the lower sign to fermions. Eq. 2.5

represents the Bose-Einstein and Fermi-Dirac distributions introduced earlier.

From the Fermi-Dirac distribution, we can obtain the average particle number $N = \sum_i \langle n_i \rangle$. If we replace summations over i by corresponding integrations, the density becomes

$$n = -\frac{1}{{\lambda^3}_{dB}} \mathrm{Li}_{3/2}(-e^{\mu/k_B T}), \tag{2.6}$$

where $\lambda_{dB}=\sqrt{\frac{2\pi\hbar^2}{mk_BT}}$ is the thermal de Broglie wavelength and $\mathrm{Li}_{\mathrm{n}}(\lambda)$ is the n^{th}-order Polylogarithm, defined as

$$\mathrm{Li}_{\mathrm{n}}(\lambda) \equiv \frac{1}{\pi^n} \int \mathrm{d}^{2n} r \frac{1}{e^{r^2}/\lambda - 1}. \tag{2.7}$$

A useful formula for integrals over PolyLogarithms is

$$\int_{-\infty}^{\infty} \mathrm{d}x \mathrm{Li}_{\mathrm{n}}(\lambda e^{-x^2}) = \sqrt{\pi} \mathrm{Li}_{\mathrm{n}+\frac{1}{2}}(\lambda). \tag{2.8}$$

This formula is particularly useful when we obtain column or doubly integrated density profiles introduced later.

At zero temperature, the fermi occupation number (Eq. 2.5) is one for $E_i < \mu$, and zero otherwise. The limiting value of μ is called the fermi energy, E_F. In terms of density, $E_F = \frac{\hbar^2}{2m}(6\pi^2 n)^{2/3}$. From the definition, the density at zero temperature in terms of μ becomes

$$n = \frac{1}{6\pi^2} \left(\frac{2m\mu}{\hbar^2} \right)^{3/2}. \tag{2.9}$$

At low temperature limit $T \ll \mu$, one can use the Sommerfeld expansion to obtain the temperature corrections to the density equation in terms of $\frac{k_B T}{E_F}$ [68]. At high temperature limit $T \gg \mu$, one can use the virial expansion to express the density equation in terms of fugacity $e^{\beta\mu}$, where $\beta = 1/k_B T$.

2.3 Fermi gases in a harmonic trap

The density obtained is for a homogeneous system. In the experiments with ultracold atomic gases, atoms are held in a trapping potential and are thus inhomogeneous. The trapping potentials can usually be approximated described by a harmonic trap. Let us now consider particles confined in a harmonic trap, with trapping potential

$$V(\mathbf{r}) = \frac{1}{2}m(\omega_x^2 x^2 + \omega_y^2 y^2 + \omega_z^2 z^2), \tag{2.10}$$

where m is atomic mass, and ω_i is trapping frequency. In the local density approximation (LDA) the system can be described as locally homogeneous with a spatially dependent chemical potential $\mu_{loc} = \mu - V(\mathbf{r})$. This provides the density distribution in a harmonic trap, given temperature T and the chemical potential μ:

$$n(\mathbf{r}) = -\frac{1}{\lambda^3{}_{dB}}\mathrm{Li}_{3/2}\left(-e^{(\mu - V(\mathbf{r}))/k_B T}\right). \tag{2.11}$$

In experiments with ultracold atomic gases, in-trap density profiles are obtained in the form of column density. Column density $\tilde{n}(y,z)$ can be obtained by integrating this equation along one axis using Eq.2.8,

$$\tilde{n}(y,z) = \int_{-\infty}^{\infty} n(x,y,z)\mathrm{d}x = -\frac{m(k_B T)^2}{2\pi\hbar^3\omega_x}\mathrm{Li}_2\left(-e^{(\mu - V(y,z)/k_B T)}\right). \tag{2.12}$$

2.4 Interaction Effect : Perturbation limit

So far we considered non-interacting systems. Now let us consider a system with spin-half fermions with balanced population in each spin state interacting through a short-range s-wave interactions (contact interactions) with scattering length a. If the interaction is weakly repulsive, the ground-state energy can be exactly calculated within standard perturbation theory. At zero temperature, the total energy is given to second order in a by the following [38]:

$$E = \frac{3}{5} N E_F \left[1 + \frac{10}{9\pi} k_F a + \frac{4(11 - 2\ln 2)}{21\pi^2} (k_F a)^2 \right], \tag{2.13}$$

where N is total number of particles, and $k_F = (3\pi^2 \frac{N}{V})^{1/3}$. Then, the chemical potential is

$$\mu = \frac{\partial E}{\partial N} = E_F \left[1 + \frac{4}{3\pi} k_F a + \frac{4(11 - 2\ln 2)}{15\pi^2} (k_F a)^2 \right]. \tag{2.14}$$

Chapter 3

Itinerant Ferromagnetism in a Fermi Gas of Ultracold Atoms

This chapter presents our research on itinerant ferromagnetism in a strongly interacting Fermi gas of ultracold atoms. This experiment was the first experimental attempt at the repulsive side of Feshbach resonance. The research simulated a simple Hamiltonian which can not be simulated by solid experiments. The experiment was reported in the publication:

- Gyu-Boong Jo, Ye-Ryuoung Lee, Jae-Hoon Choi, Caleb A. Christensen, Tony H. Kim, Joseph H. Thywissen,David E. Pritchard and Wolfgang Ketterle
  Itinerant Ferromagnetism in a Fermi Gas of Ultracold Atoms
  Science 325 , 1521-1524 (2009). Included in appendix D.

More details on this research can be found in Gyu-Boong Jo's doctoral thesis [30].

3.1 Itinerant Ferromagnetism and Stoner Model

Iron, nickel, and cobalt can form permanent magnets, or are attracted to magnets. This kind of magnetism is caused when electron spins line up parallel with each other and is called *ferromagnetism.* Here, the electrons whose spins aligned to create the magnetic state are the conduction electrons which are not localized to any particular atoms in a metal. Thus, the magnetism of iron, nickel, and cobalt is called *itinerant* ferromagnetism.

The Stoner model and its extensions [70] have been used to describe itinerant ferromagnetism. Stoner assumed that the interaction between electrons can be seen as *screened* Coulomb interaction, which in turn can be estimated as a short-range repulsive interaction. This simplified model is not enough to explain real ferromagnets in a quantitative way [72]. However, this model can be realized and tested using Fermi gas of ultracold atoms instead of electrons [19].

Here we simulate the Stoner model using an ultracold Fermi gas of ^{6}Li atoms. The ^{6}Li atom has the total nuclear spin I=1 and the total electron spin S=1/2. Its ground state where angular momentum L=0 splits into six states under the external magnetic field. We use two lowest energy states, $|F = 1/2; m_F = 1/2\rangle$ and $|F = 1/2; m_F = -1/2\rangle$, to simulate two spin-states of an electron. The screened Coulomb interaction of electrons can be realized by the s-wave scattering caused by Feshbach resonance of the two pseudo-spin states of ^{6}Li atoms. Due to the angular momentum conservation one state cannot be converted to the other state unlike electrons. That is, the number of atoms in each state is fixed. Therefore, the net spin polarization is zero in case of balanced spin mixture, which corresponds to zero external magnetic field in solid state systems. More detailed comparison can be found in chapter 4.1.

Intuitively speaking, the Stoner model predicts ferromagnetism based on competition between kinetic energy and interaction energy. In order to understand this model, let us consider a simple mean-field model of a two-component Fermi gas.

The total energy of a two-component Fermi gas of density n_σ (for each spin state) in a volume V is

$$E_{total} = \sum_{\sigma=\uparrow,\downarrow} \frac{3}{5} V E_{F,\sigma} n_\sigma + g V n_\uparrow n_\downarrow, \tag{3.1}$$

where $E_{F,\sigma} n_\sigma = \frac{\hbar^2 k_{F,\sigma}^2}{2m}$ and $g = \frac{4\pi\hbar^2 a}{m}$. The first part of the equation comes from kinetic energy, and the second part comes from the interaction energy. Let us consider a

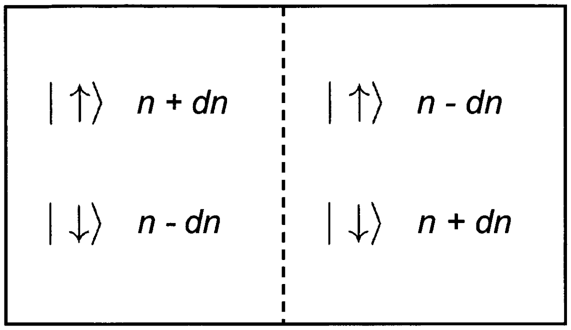
$|\uparrow\rangle$ n + dn
$|\downarrow\rangle$ n - dn
$|\uparrow\rangle$ n - dn
$|\downarrow\rangle$ n + dn

Figure 3-1: A simple mean-field model of a two-component Fermi gas. n is the density of the gas. We introduce local density imbalance dn in order to check the instability toward the ferromagnetic state.

locally polarized case while the net polarization is kept zero (see Fig. 3-1). We define the local magnetization of the Fermi gas, $\eta = \frac{dn}{n}$, where $dn = n_\uparrow - n_\downarrow$ and $n = n_\uparrow + n_\downarrow$. The total energy can be expressed using the local magnetization η as

$$E_{total} = E_F 2Vn \left[\frac{3}{10} \left((1+\eta)^{5/3} + (1-\eta)^{5/3} \right) + \frac{2}{3\pi} k_F a (1+\eta)(1-\eta) \right]. \tag{3.2}$$

The kinetic energy increases when the local magnetization increases. This increase max out when the cloud is fully polarized. In contrast, the interaction energy of the balanced cloud continuously increases when the interaction parameter $k_F a$ increase, and the interaction energy of the fully polarized cloud becomes completely zero. Therefore, the fully polarized case becomes energetically favorable when the increase in interaction energy becomes greater than the increase in the kinetic energy. This is the simple explanation behind Stoner model. The exact phase transition occurs when the curvature of the energy curve becomes zero at $\eta = 0$ (see Fig. 3-2 (a)), which gives the critical interaction strength $k_F a = \pi/2$.

We consider the thermodynamic quantities at constant volume for simplicity. However, the atoms trapped in a harmonic potential is more relevant at constant pressure. At constat pressure, the system reaches equilibrium when minimizing the enthalpy $H = E_{total} - PV$, where $P = -dE_{total}/dV$. Fig. 3-2 (b) shows magnetization, kinetic energy, volume, and enthalpy as a function of interaction parameter $k_F a$. At the phase transition, we can observe the onset of magnetization, the minimum in the kinetic energy, and the maximum in the size of the cloud. Thus these features can be interpreted as evidences for ferromagnetic phase transition.

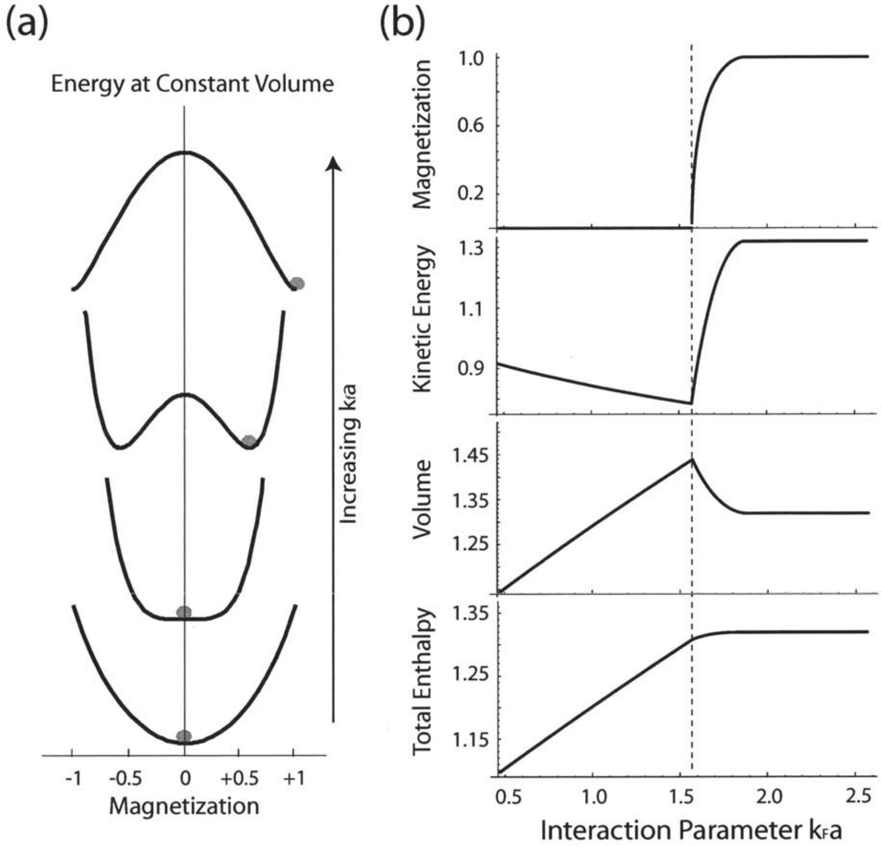

Figure 3-2: Mean-field prediction of ferromagnetism. (a) Total energy at different local magnetization η and interaction parameter $k_F a$. (b)Magnetization, kinetic energy, volume, and enthalpy as a function of interaction parameter $k_F a$. The ferromagnetic transition occurs at the dotted line.

3.2 Experimental Procedure

An evaporative cooled equal mixture of $|1\rangle$ and $|2\rangle$ spin states is prepared at 590 G as described in chapter 1.4. We increase the magnetic field in order to increase interaction strength. Due to eddy current, the fasted ramp to the target field was limited to 4.5 ms.

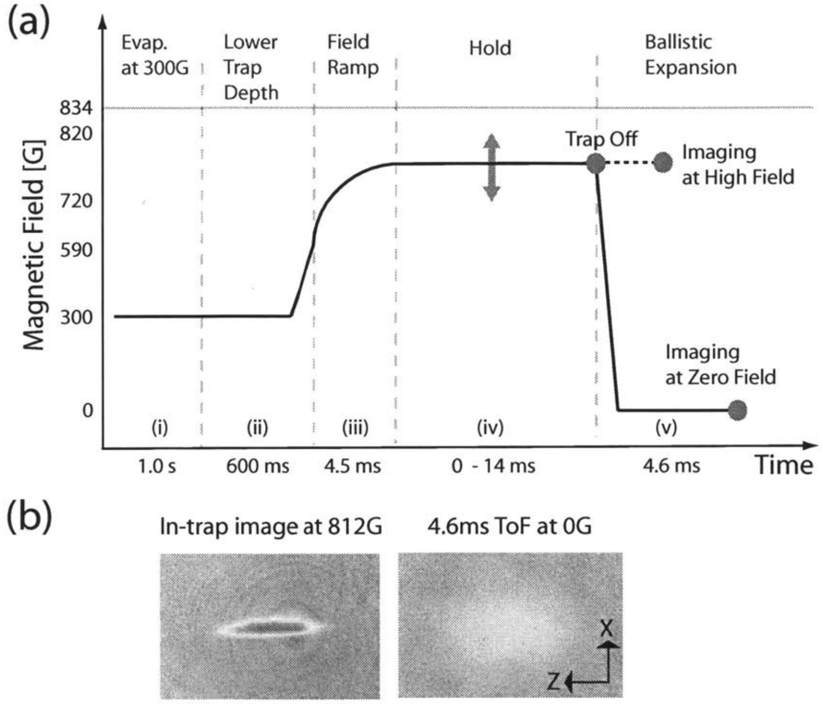
(a)
Evap. at 300G
Lower Trap Depth
Field Ramp
Hold
Ballistic Expansion
834
820
720
590
300
0
Magnetic Field [G]
Trap Off
Imaging at High Field
Imaging at Zero Field
(i)
(ii)
(iii)
(iv)
(v)
1.0 s
600 ms
4.5 ms
0 - 14 ms
4.6 ms
Time
(b)
In-trap image at 812G
4.6ms ToF at 0G
X
Z

Figure 3-3: The experimental procedure. (a) The sequence of the magnetic field ramp. (b) Image samples.

In order to measure the loss rate, we recorded the atom number for 2 ms right after the ramp. Then, we obtained the loss rate by fitting linearly over time because the initial loss rate can be approximated to be linear (see Fig. 3-4 (b),(c)). For kinetic energy and cloud size measurement, the optical trap and the magnetic fields were suddenly turned off. After 4.6 ms of ballistic expansion, we imaged the $|1\rangle$ state atoms at zero field. The kinetic energy was determined by $E_{kin} = \frac{3m\sigma^2{}_x}{2\triangle^2{}_{tof}}$, where σ_x is the Gaussian radial width and $\triangle_{tof}$ is the ballistic expansion time. The cloud size was determined by the Gaussian radial width σ_z. We measured the temperature by fitting finite temperature in-trap density profile right after the ramp.

3.3 Itinerant Ferromagnetism in a Fermi Gas of Ultracold Atoms

As we reviewed in the section 3.1, ferromagnetic phase transition shows the onset of magnetization, the minimum in the kinetic energy, and the maximum in the size of the cloud. Even though these features are not sufficient conditions for ferromagnetic phase transition, they are necessary conditions.

The onset of magnetization can be observed by measuring the loss rate because the loss rate is proportional to $n_\uparrow n_\downarrow a^6 max(T, T_F)(\propto 1-\eta^2)$ [52]. In Fig. 3-4, we observe decreasing loss rate for $k^0{}_F a > 2.2$ at $T = 0.12T_F$. If there is no magnetization, the loss rate should increase as the interaction strength increases. Therefore, this maximum in the loss rate indicates the onset of magnetization.

We also investigate thermodynamic quantities. In Fig. 3-5, we observe the minimum in the measured kinetic energy as in Fig. 3-2. In Fig. 3-6 (a), we observe the maximum in the measured size of the cloud as well.

Lastly the observed features depends on the temperature. As temperature of the system increase, the critical interaction strength $k^0{}_F a$ increases. In addition, the critical $k^0{}_F a$ is consistent for all three evidences at the same temperature.

The critical value of $k^0{}_F a$ we found is different from the value $\pi/2$ from the mean-field prediction in the section 3.1. The mean-field model assumed zero temperature and homogeneous density. In the experiment, the temperature is finite and the density is inhomogeneous in the harmonic trap. In addition, we determined the $k^0{}_F a$ from total atom number assuming zero temperature without interaction, where the real $k_F a$ depends on the local density at finite temperature with interaction. These condition count for the discrepancy in the critical $k_F a$. Theoretical works support the discrepancy in the critical $k_F^0 a$ by introducing the trap [37], Monte-Carlo simulation [11, 53], and the second-order correction to the mean-field interaction [15].

The most powerful evidence of the ferromagnetism would be the observation of the spin domains. However, we were unable to observe the spin domains using in-situ phase-contrast imaging. Based on the signal to noise ratio of ~ 10 and the $\sim 3\ \mu m$

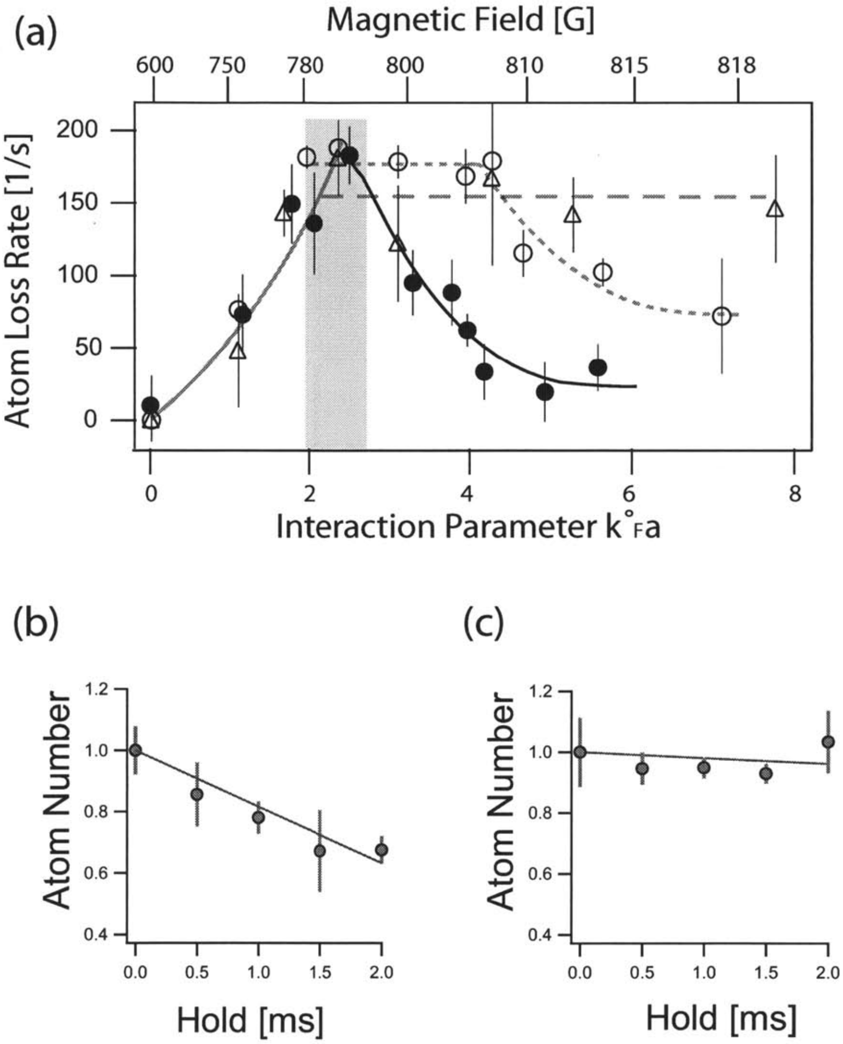

Figure 3-4: Atom loss rate. (a) Atom loss rate at different interaction strength $k^0{}_F a$ and at different temperatures of $0.55 T_F$(dashed curve), $0.22 T_F$(dotted curve), and $0.12 T_F$(solid curve) Note that the curves are guides to the eye assuming that the loss rate saturates. (b),(c) Loss rate determination.

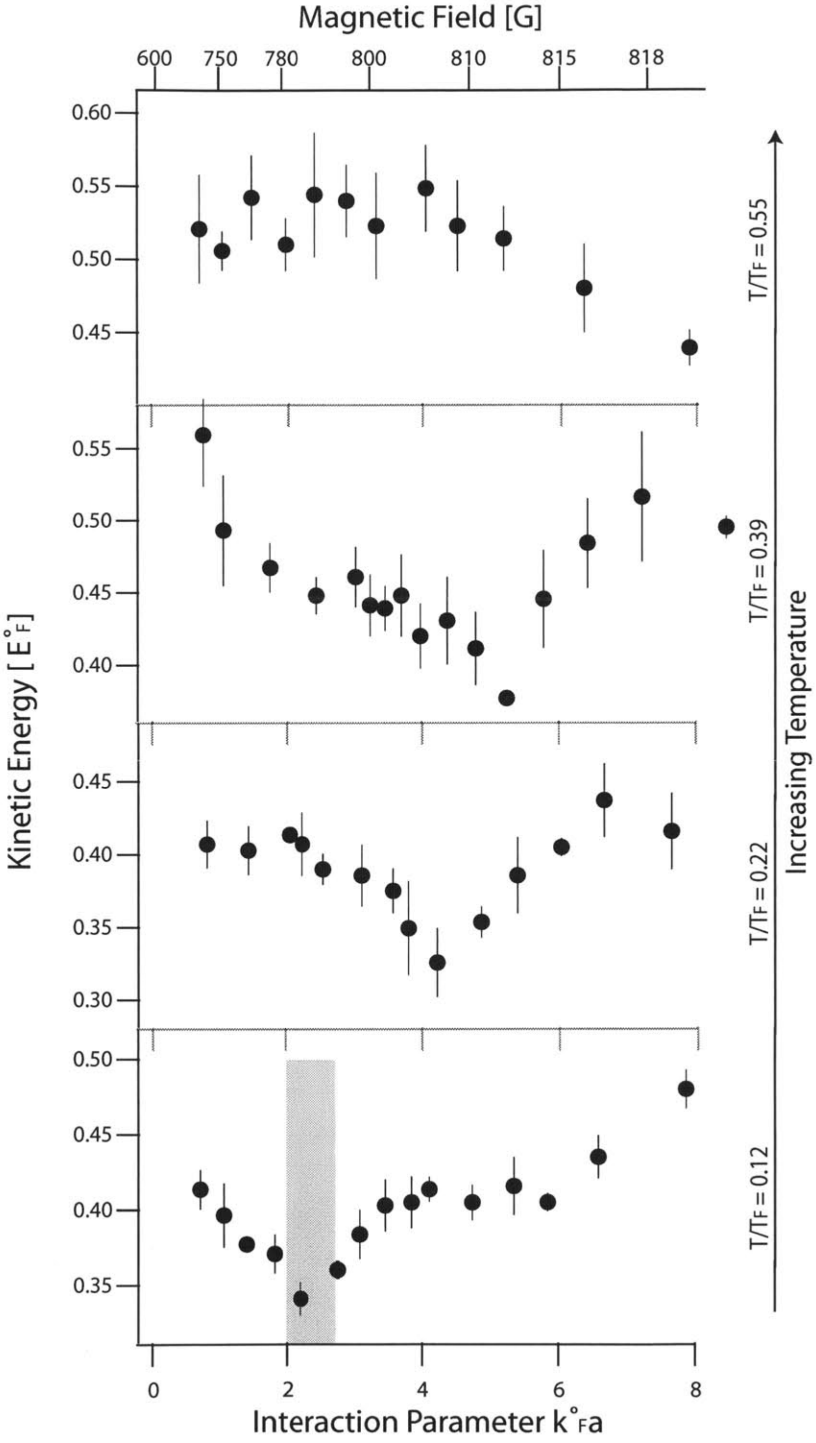

Figure 3-5: Kinetic energy measurement. The kinetic energy at different interaction strength ${k^0}_F a$ and at different temperatures.

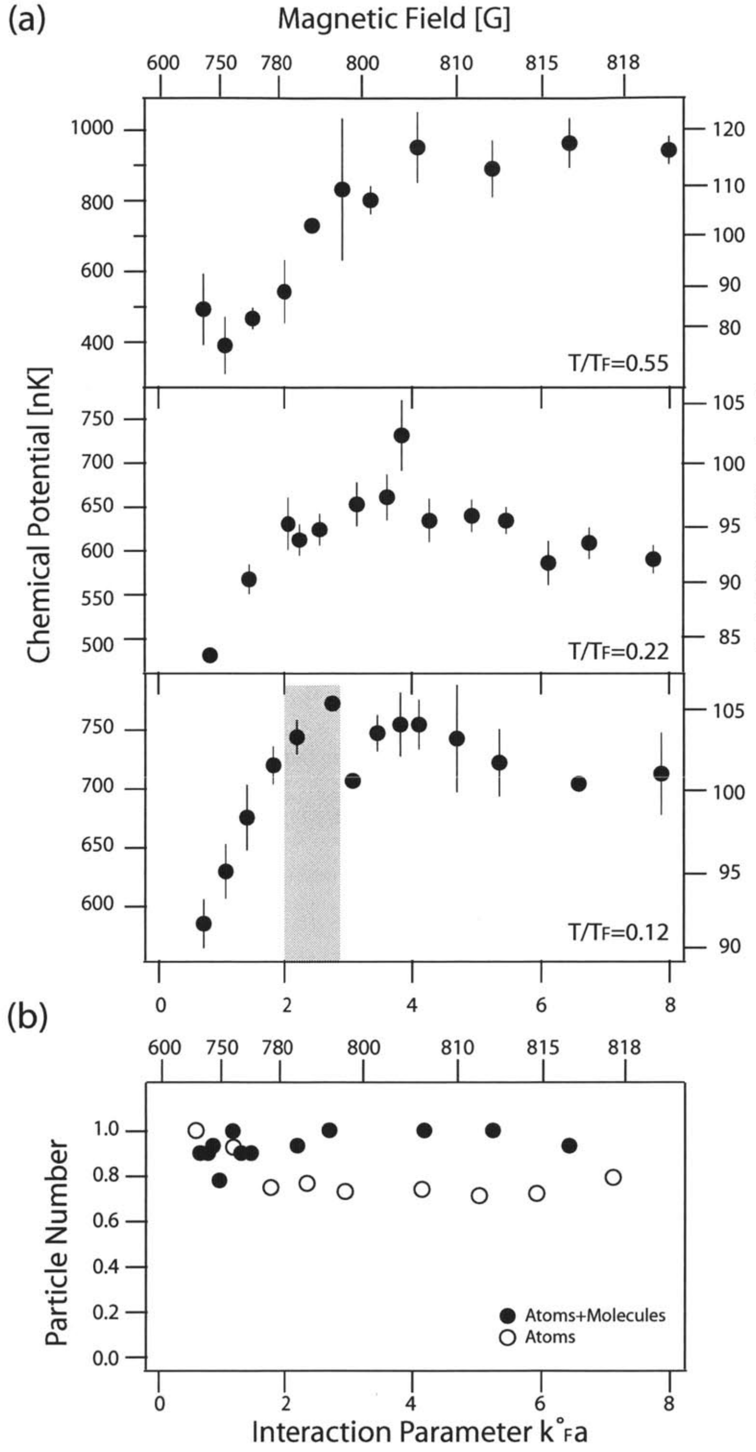

Figure 3-6: Cloud size and molecular fraction. (a) Cloud size at different interaction strength $k^0{}_Fa$ and at different temperatures. The chemical potential (b) Measured molecular fraction in the sample we used.

resolution of our imaging system, the upper limit of the domain volume is $\sim 5\ \mu m^3$ with ~ 50 atoms.

The main difference between this experiment and the Stoner model is the existence of the molecules in the sample. As in Fig. 3-6 (b), there is about 25 % of molecular fraction in the sample. Even though the molecules exit, the molecular fraction of the sample is constant from $k^0{}_F a > 1.8$ where we observed the evidences of the transition. Thus, the molecular fraction is not the reason behind the sudden changes. We confirmed this by conducting the kinetic energy measurement with about 60 % molecular fraction in the sample. We observed the minimum in the measured kinetic energy at the same $k^0{}_F a$.

We measured the temperature by fitting finite temperature in-trap density profile right after the ramp. Considering the trap frequency, 4.5 ms ramp is about a quarter of trap period, and it is only marginally adiabatic. Since the temperature fitting should be done to a sufficiently equilibrated profile, this can be done more accurately. In addition, at high field imaging, the atoms and molecules are indistinguishable [34]. Therefore, the density profile contains molecular density profiles resulting in errors. Actually, the lowest temperature accurately measured at repulsive side was about 0.2 T_F both in chapter 4 and in Ref. [57].

3.4 Further Development

A recent experimental study using 350 μs ramp to the target field observed that pair formation occurs on a very short time scale [57]. This work also showed the absence of a dramatic increase in spin fluctuations, which is evidence *against* the ferromagnetic transition. A theoretical study supports this finding by showing that the pairing growth rate is larger than that of ferromagnetic instabilities [51,65]. In addition, Ref. [51] has shown that the pairing instability can lead to similar experimental signatures as we have observed. In conclusion, it turned out that *no ferromagnetic phase* has been formed in our experiment. Still, our work stimulated a lot of interest for ultracold Fermi gases with repulsive interaction.

Chapter 4

Pauli Paramagnetism in an Ideal Fermi Gas

In chapter 3, we focused on the qualitative features to observe the evidences of the phase transition. We measured thermodynamic quantities of the whole trapped gas while the real atoms were held in a trapping potential and inhomogeneous. In this chapter, we focus on the more quantitative study of ultracold gases.

Using local density approximation, the ultracold gas can be locally described as a homogeneous gas. That is, each local points in the gas can be considered as homogeneous systems with different conditions. Therefore, the trapped gas can provide lots of useful information on the equation of state of the system.

A new level of quantitative comparison between theory and experiment was recently reached by careful measurements of density profiles from which the equation of state could be determined. These techniques were first proposed by Chevy [12] and Bulgac [10] and implemented by Shin [61]. Further improvements [27, 28, 36, 44–46] resulted in impressive accuracy without adjustable parameters. These results hinge on accurate measurements of the equilibrium atomic density distribution.

In these quantitative researches, ultracold atoms served as model systems for exploring novel and unknown many-body physics. On the other hand, we can also use the ultracold atoms as model systems to demonstrate well-known textbook physics in a more ideal way than other systems.

Here, we use the tunability of atomic interactions near Feshbach resonances to create a non-interacting Fermi gas with two components. This is an ideal realization of a free electron gas (FEG) with spin up and spin down components, as assumed in the simple theory of metals. We demonstrate how such an ideal Fermi gas will respond to external magnetic fields, which is described by Pauli paramagnetism.

In all previous studies of paramagnetism, the magnetization was weak since the applied magnetic field times the magnetic moment was much smaller than the Fermi energy [32, 58–60]. In addition, the measurements even in simple metals revealed major discrepancies to the predicted value due to interaction effects [32,58–60]. With ultracold atoms, we can easily realize the strong field case where the chemical potential difference is larger than the Fermi energy and therefore fully polarizes the gas. In addition, we can experimentally demonstrate Pauli paramagnetism in a truly non-interacting system which is exactly described by basic theory.

4.1 Pauli Paramagnetism: Ultracold Atomic Gas vs Solid State System

Table 4.1: Comparison between a free electron gas and two-component Fermi gases in the study of magnetism

Properties	**Free electron gas**	**Two-component Fermi gases**
Magnetization	$\mu_B(N_\uparrow - N_\downarrow)/V$	$\Delta n = (N_\uparrow - N_\downarrow)/V$
Magnetic field	External B field	$\Delta\mu = \mu_\uparrow - \mu_\downarrow$
Normalized Susceptibility	$\mu_B \partial(\Delta n/n)/\partial(B/E_F)$	$\partial(\Delta n/n)/\partial(\Delta\mu/E_F)$

Pauli paramagnetism explains the magnetization of a free electron gas with two spin states in the presence of an external magnetic field B neglecting the contribution from the orbital motions. In the presence of an external magnetic field B, the energy of a particle is given by

$$\varepsilon = \frac{p^2}{2m} \pm \mu_B B, \tag{4.1}$$

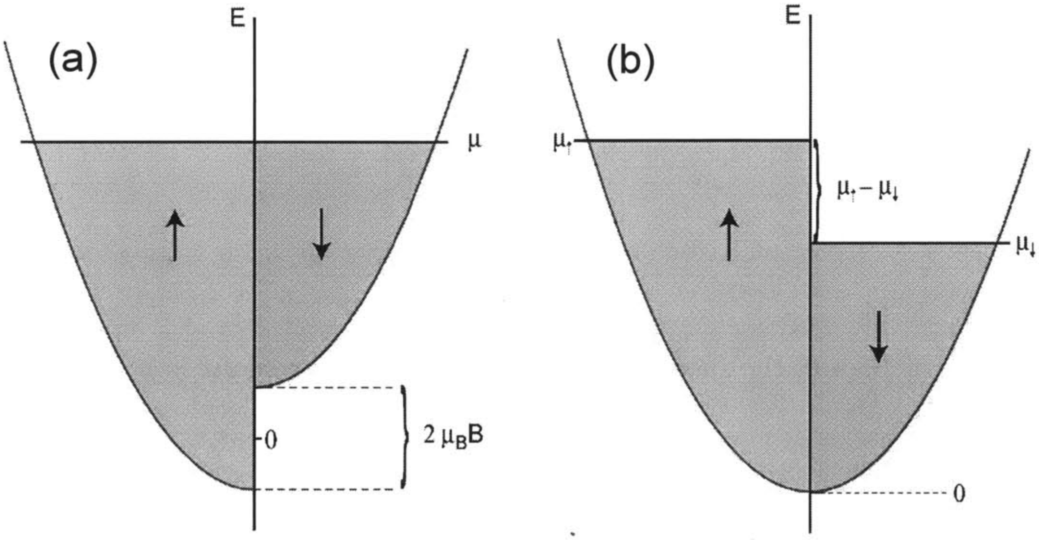

Figure 4-1: Comparison between a free electron gas(a) and two-component Fermi gases(b) in the study of magnetism. Curves show density of states for each spin states $g(E)$. (a) shows the response of free electron gases to the external magnetic field B. (b) shows the imbalanced two-component Fermi gases.

with upper sign corresponding to the antiparallel spin state, the lower sign to the parallel spin state the magnetic field B. The total number $N_{\uparrow(\downarrow)}$ of electrons in each spin state changes satisfying at zero temperature (T=0)

$$N_{\uparrow(\downarrow)} = \int_{\mp\mu_B B}^{\mu^g} g(E \pm \mu_B B) dE, \tag{4.2}$$

where $g(E)$ is the density of states and μ^g is the global chemical potential (see Fig. 4-1(a)). In an zero temperature ideal gas, the global chemical potential is the same as Fermi energy $E_F = \frac{\hbar^2(6\pi^2 n)^{2/3}}{2m}$, where $n = (n_\uparrow + n_\downarrow)/2$. The magnetization M is then given by

$$M = \mu_B(N_\uparrow - N_\downarrow)/V = \mu_B \Delta n. \tag{4.3}$$

The susceptibility of the electron gas is defined as

$$\chi = \frac{\partial M}{\partial B} = \mu_B \frac{\partial \Delta n}{\partial B}. \tag{4.4}$$

In the limit of $B \to 0$, the slice of energy thickness transferred $\Delta\epsilon$ is $\mu_B B$. Thus, the magnetization is

$$M = 2\mu_B g(E_F)\Delta\epsilon = 2\mu_B g(E_F)\mu_B B. \tag{4.5}$$

Therefore, we obtain the low-field susceptibility

$$\chi_0 = 2{\mu_B}^2 g(E_F) = 2{\mu_B}^2 \frac{3}{2}\frac{E_F}{n}. \tag{4.6}$$

In condensed matter physics, the normalized susceptibility $\overline{\chi}$ is often used as a dimensionless quantity. The susceptibility is normalized using χ_0:

$$\overline{\chi} = \chi/\chi_0 = \frac{1}{3}\frac{E_F}{n}\frac{\partial \Delta n}{\partial \mu_B B} = \frac{1}{3}\partial\left(\frac{\Delta n}{n}\right)/\partial\left(\frac{\mu_B B}{E_F}\right). \tag{4.7}$$

The last equation is valid because the average density n is constant.

Here we simulate this magnetism using an ultracold Fermi gas of ^{6}Li atoms. We use two lowest energy states, $|F = 1/2; m_F = 1/2\rangle$ and $|F = 1/2; m_F = -1/2\rangle$, to simulate two spin-states of an electron. As mentioned in chapter 3.1, one state cannot be converted to the other state unlike electrons. That is, the number of atoms in each state is fixed. Note that the real external magnetic field is not the source of the population imbalance (magnetization). The spins here can be regarded nuclear spins, hence the magnetic field here is only used to split the hyperfine state. Then, what is the relevant variable in the ultracold atoms that corresponds to the external magnetic field in the electron gas? In the two-component Fermi gases, the magnetization Δn is introduced by preparing different number of atoms in each state. The two different pseudo spin states have different chemical potentials, $\mu_\uparrow$ and $\mu_\downarrow$. In Fig. 4-1(b), we can observe the chemical potential difference between two states, $\Delta\mu = \mu_\uparrow - \mu_\downarrow$, corresponds to the energy shift due to the external magnetic field in the electron gas (Fig. 4-1(a)).

If we compare the corresponding equations, the number in each spin state at $T = 0$ is given by

$$N_{\uparrow(\downarrow)} = \int_0^{\mu^g_{\uparrow(\downarrow)}} g(E)dE = \int_{\mp\Delta\mu/2}^{\tilde{\mu}^g} g(E \pm \Delta\mu/2)dE, \tag{4.8}$$

where $\mu^g_{\uparrow(\downarrow)}$ is the global chemical potential of each component of gases. We define $\tilde{\mu}^g = (\mu_\uparrow + \mu_\downarrow)/2$ and $\Delta\mu = \mu_\uparrow - \mu_\downarrow$. By comparing this with Eq.(4.2), we again find that the chemical potential difference $\Delta\mu$ corresponds to the energy shift due to the magnetic field in the electron gas.

Let us now consider the *trapped* two-component Fermi gases. As we discussed in the previous section, we can treat each local position ($\vec{r}$) in the trap as homogeneous systems with the local chemical potential $\mu_{\uparrow(\downarrow)}(\vec{r}) = \mu^g_{\uparrow(\downarrow)} - V(\vec{r})$ and the local density $\mu_{\uparrow(\downarrow)}(\vec{r})$ using the local density approximation. Here, the chemical potential difference $\Delta\mu(\vec{r}) \equiv \mu_\uparrow(\vec{r}) - \mu_\downarrow(\vec{r})$ is the same throughout the cloud as in Fig.4-3(b). However, the meaningful measure of the chemical potential difference is its relative value to the Fermi energy, or the global chemical potential. Therefore, we can still define and measure the normalized susceptibility of the ultracold atoms corresponding to the Eq. 4.7 as

$$\overline{\chi} = \partial\left(\frac{\Delta n}{n}\right) / \partial\left(\frac{\Delta\mu}{E_F}\right) = \partial\left(\overline{\Delta n}\right) / \partial\left(\overline{\Delta\mu}\right), \tag{4.9}$$

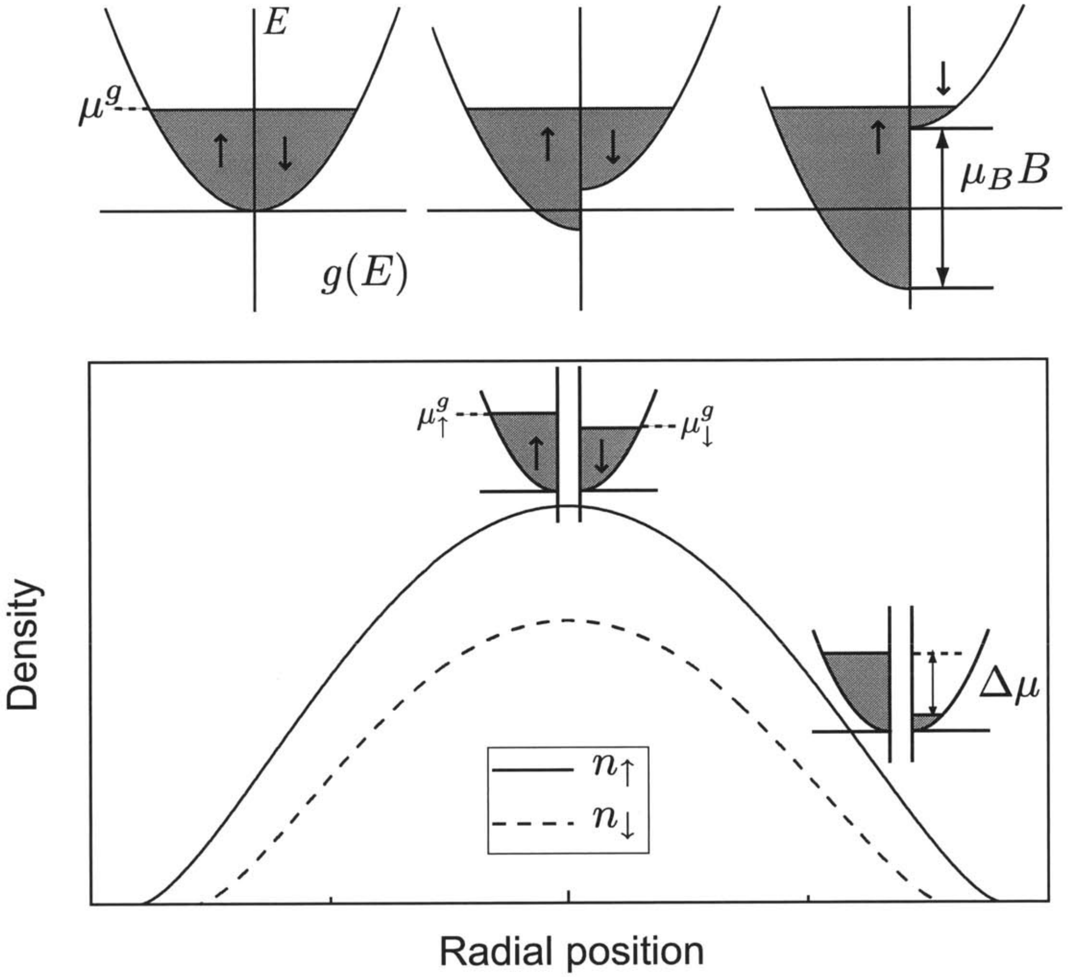

Figure 4-2: Comparison between a free electron gas and two-component Fermi gases trapped in the spherical harmonic trapping potential. Figures at the top shows the response of free electron gases to the external magnetic field B. $g(E)$ is the density of states. The figure at the bottom shows density distributions of two-component ultracold Fermi gases at zero temperature, $n_\uparrow$ and $n_\downarrow$. Each position in the trap corresponds to the different magnetization under different strength of the field, This is illustrated in diagrams inside the plot, where the gaps between two states represent non-interchangeability of spin state.

where we define $\overline{\Delta n} = (n_\uparrow - n_\downarrow)/n$ and $\overline{\Delta \mu} = (\mu_\uparrow - \mu_\downarrow)/E_F$. For fully polarized gas, $\overline{\Delta n} = 2$ and $\overline{\Delta \mu} = 2^{2/3}$. In the trapped gases, $\overline{\Delta n}$ and $\overline{\Delta \mu}$ changes throughout the cloud as in Fig. 4-3. Therefore, we can determine the normalized susceptibility $\overline{\chi}$ by measuring the slope from $\overline{\Delta n}$ versus $\overline{\Delta \mu}$ as in Fig. 4-3(d). The zero temperature normalized susceptibility in the limit of $\overline{\Delta \mu} \to 0$ (which is equivalent to $\Delta n \to 0$) is

$$\overline{\chi}_0 = \frac{E_F}{n} \partial(\Delta n)/\partial \left(\frac{\hbar^2 (6\pi^2)^{2/3}}{2m} \left((n + \Delta n)^{2/3} - (n - \Delta n)^{2/3} \right) \right) = \frac{3}{2}. \tag{4.10}$$

4.2 Experimental Procedure

An evaporative cooled imbalanced mixture of $|1\rangle$ and $|2\rangle$ spin states is prepared at 528 G where the interaction between two states is zero, as described in chapter 1.4.

In order to obtain the density profiles of each component of atoms, we use the double-shutter phase contrast imaging technique with two different frequencies. One is tuned to the middle of the two optical transition frequencies for $|1\rangle$ and $|2\rangle$ and the other is tuned closer to the state $|1\rangle$ by 12 MHz.

The normalized phase-contrast signal (for negligible absorption) is

$$\frac{I}{I_o} = 3 - 2\sqrt{2}\cos(\phi \pm \pi/4), \tag{4.11}$$

where the phase shift $\phi = -\frac{\tilde{n}\sigma_o}{2}\frac{\delta}{1+\delta^2}$, $\sigma_o = \frac{3}{2\pi}\lambda^2$, $\delta = \frac{\omega - \omega_o}{\Gamma/2}$, and $\tilde{n}$ is the column density [33]. The sign depends on laser detuning and the sign of the phase shift imparted by the phase plate. Using Eq. 4.11, we can determine the phase shift from the normalized phase-contrast signal. The phase shifts from two different frequencies are

$$\phi_1 = \frac{\sigma_o}{2}\frac{\delta_o}{1+{\delta_o}^2}\left(\tilde{n}_1 - \tilde{n}_2\right) \tag{4.12}$$

$$\phi_2 = \frac{\sigma_o}{2}\left(\frac{\delta_1}{1+{\delta_1}^2}\tilde{n}_1 - \frac{\delta_2}{1+{\delta_2}^2}\tilde{n}_2\right). \tag{4.13}$$

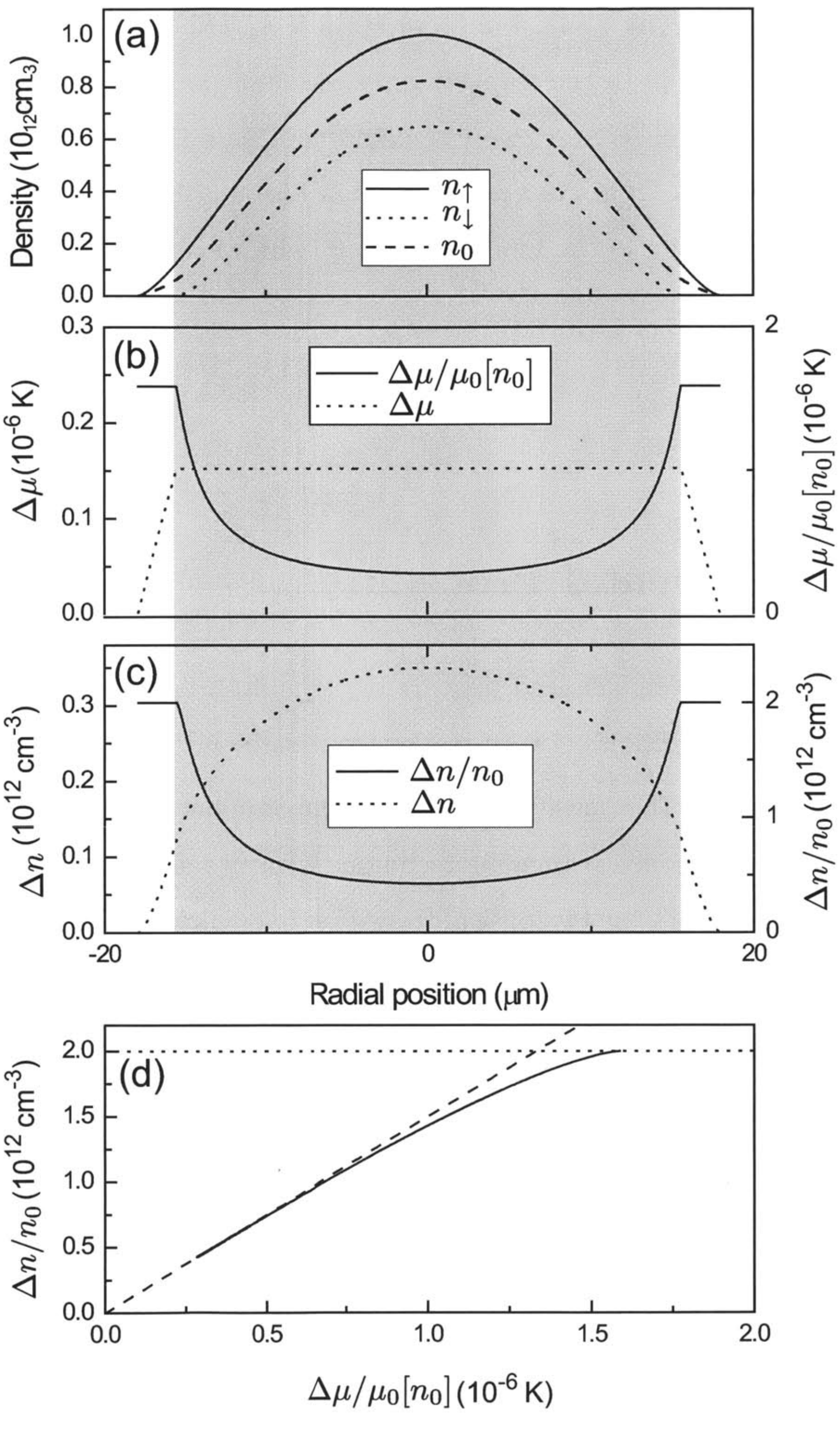

Figure 4-3: (a) Simulated density profiles of two-component Fermi gases in a spherical harmonic trap at zero temperature. The total population imbalance $\Delta \equiv (N_\uparrow - N_\downarrow)/(N_\uparrow + N_\downarrow) = 21\%$. The shaded and white regions correspond to the partially and fully polarized regions respectively. (b) The local chemical potential difference with and without the normalization. (c) The density difference with and without normalization. (d) $\overline{\Delta n}$ versus $\overline{\Delta\mu}$ from the density profile (a). The linear fit near the origin (the dashed line) gives the low field normalized susceptibility.

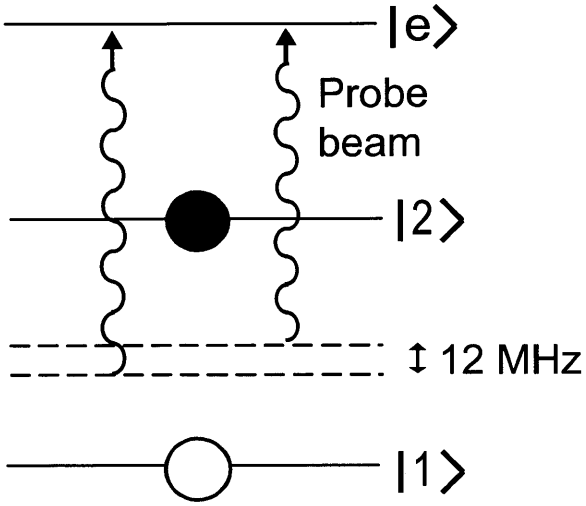

Figure 4-4: The double-shutter phase contrast imaging with two different imaging frequencies.

From this equation, we can find find the column density of each spin state.

If we normalized the phase shift by $\frac{\sigma_o}{2}\frac{\delta_o}{1+\delta_o{}^2}$, we can simplify the equation as

$$\overline{\phi}_1 = \tilde{n}_1 - \tilde{n}_2 \tag{4.14}$$

$$\overline{\phi}_2 = \alpha\tilde{n}_1 - \beta\tilde{n}_2. \tag{4.15}$$

We know the value of α and β from calculation, but we can also determine them experimentally by taking images of the pure $|1\rangle$ and $|2\rangle$ states.

4.3 Susceptibility Measurement

We measured line-of-sight integrated profiles of column density using in situ phase-contrast imaging [64]. The signal-to-noise was improved by averaging the four quadrants of the images around the center and by averaging the column density along equipotential lines (which are ellipses for the anisotropic harmonic oscillator potential).

Fig.4-5(a) is the column density distributions in two states, where the elliptical density profile is rescaled to be circular. These column density profiles are fitted with finite-temperature Fermi gas 2D distribution from Eq. 2.12,

$$\tilde{n}(r) = -\frac{m(k_BT)^2}{2\pi\hbar^3\omega_z}\mathrm{Li}_2\left[-\exp\left(\frac{\mu - V(r)}{k_BT}\right)\right]. \tag{4.16}$$

First, we fit the column density profile of the majority component, $|\uparrow\rangle$, and determine the temperature T and the global chemical potential $\mu^g_\uparrow$. Since the temperature T of the two components is the same, we fit the minority component to determine $\mu^g_\downarrow$ with the temperature constrained to be the temperature determined from the majority component fitting. Three-dimensional density profiles $n(r)$ in Fig.4-5(b) were reconstructed by applying the inverse Abel transformation to the column densities $\tilde{n}(r)$ [64].

The temperature was about 0.2 T_F. For finite but low temperatures, the low field susceptibility is

$$\overline{\chi} = \overline{\chi}_0\left[1 - \frac{\pi^2}{12}\left(\frac{T}{T_F}\right)\right] \tag{4.17}$$

from the Sommerfeld expansion [49].

As we can see in Fig. 4-5(c), we cannot use the derivative of $\overline{\Delta n}$ with respect to $\overline{\Delta\mu}$ at each position because of the noise. Thus, we use the linear fit of $\overline{\Delta n}$ as a function of $\overline{\Delta\mu}$ in order to determine the susceptibility. We accumulated $\overline{\Delta n}$ vs $\overline{\Delta\mu}$ plots from 20 images for averaging (see Fig. 4-5(c)). The linear fitting to the origin near the center of the profile gives $\overline{\chi} = 1.44$, which is in a good agreement with the theoretical value of 1.45 from Eq. 4.17 at $T/T_F = 0.2$.

Note that the local T/T_F and the local susceptibility changes within the fitting region as in Fig. 4-3(d) because the density n and the normalized chemical potential difference $\overline{\Delta\mu}$ changes within the fitting region. Thus, we limited the fitting region to where the deviation of the susceptibility is small within our experimental resolution. From simulation, the deviation in measured susceptibility from that of the center of the profile is about 4 %.

Even small difference in T/T_F at the center of the profile gets amplified near the wings of the profile as T_F decreases. In addition, the temperature dependence of the susceptibility is beyond the second order correction from the Sommerfeld expansion.

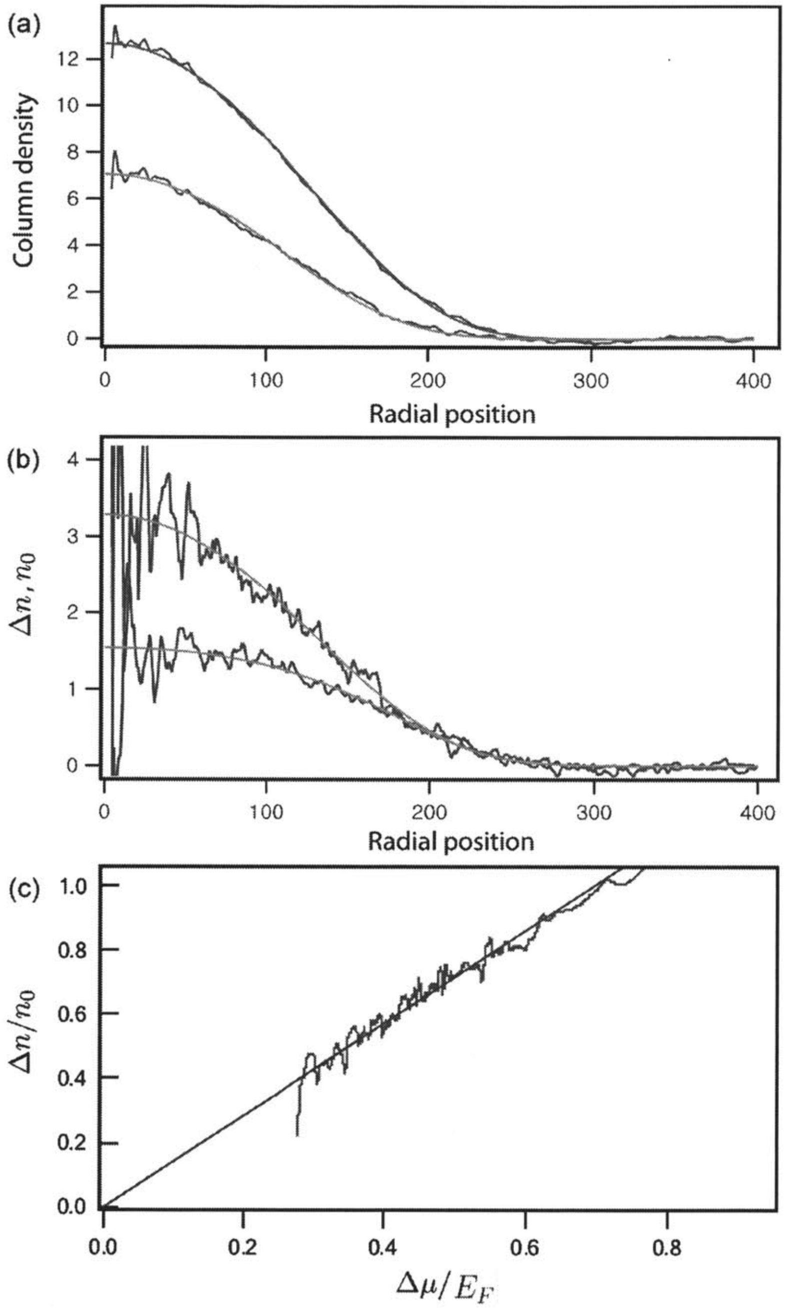

Figure 4-5: (a) Column density $\tilde{n}$. The temperature determined from the fit (solid curves) is about 0.2 T_F. (b) Red line shows difference of three dimensional densities Δn. Blue line shows average three dimensional density n_0 of the two states. Green lines are Δn and n_0 from theoretical calculation using the chemical potentials and the temperature obtained from (a). (c) The normalized three dimensional density difference is plotted as a function of the normalized chemical potential difference. The graph shows averaged plots from 20 profiles. We determine the susceptibility from the slope of the linear fitting to the origin. The measured $\overline{\chi}$ is 1.44.

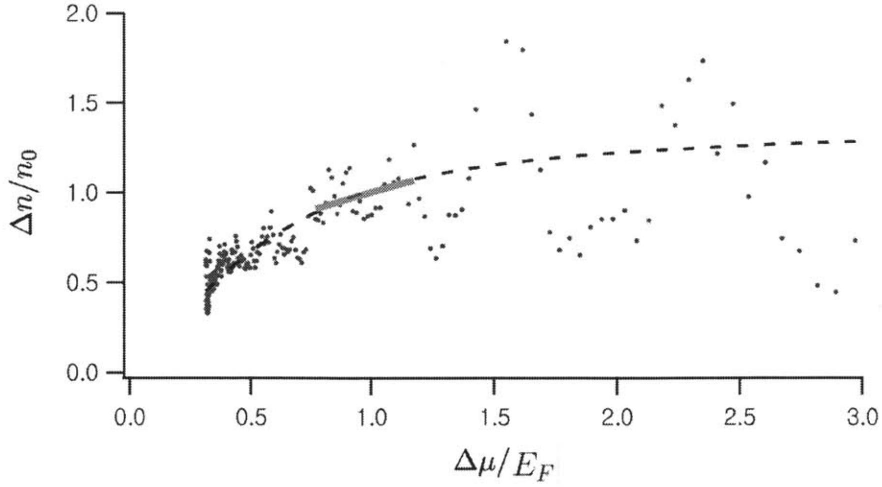

Figure 4-6: Susceptibility at high magnetic field. Points are data from a single image. Dashed line shows the plot from a simulation using the same parameters as the experiment. Solid line is the linear fitting of the data for susceptibility measurement around $\overline{\Delta\mu} = 1$.

Therefore, we cannot use accumulated plots for susceptibility measurement near the wings of the profile, which corresponds to the susceptibility at strong magnetic field. In order to measure the strong field susceptibility, we use a $\overline{\Delta n}$ vs $\overline{\Delta\mu}$ plot from a single profile (see Fig. 4-6). The linear fit around $\Delta\mu/E_F = 1$ gives $\overline{\chi} = 0.39$. Within the fitting range, T/T_F changes from 0.45 to 0.7. The susceptibility obtained from a simulation with the same parameters is 0.48. About 6 % error comes from the T/T_F and $\overline{\Delta\mu}$ changing fitting region. We observe that the susceptibility approaches zero as the chemical potential difference (corresponding the applied magnetic field times the magnetic moment) becomes comparable to the Fermi energy of the system.

We measured the ideal Pauli susceptibility in ultracold Fermi gases. Since we can control the interaction strength between two pseudo-spin states to be zero, it is possible to measure the Pauli susceptibility accurately while the experiments in condensed matter physics observed major discrepancies due to interaction effects. In addition, the strong field Pauli susceptibility can be measured where the chemical potential difference is comparable to the Fermi energy. This shows that the ultracold atoms can be a good tool to study basic physics of many-body systems.

4.4 Susceptibility Measurement in Systems with Interaction

In the previous section, we measured the susceptibility of the ideal gas. Let us now consider the interacting case. Recently, the susceptibility was measured for fermions with attractive interactions [45]. The susceptibility measurements on the repulsive side of interaction could address the possible existence of a ferromagnetic transition in a repulsive Fermi gas (in chapter 3 for which the spin susceptibility would diverge at the phase transition [54].

However, there are some complications with the repulsive side of interaction.

First, the two-component Fermi gases with repulsive interaction are unstable because they are realized on the so-called upper branch of a Feshbach resonance where decay is always possible into the so-called lower branch which consists of weakly bound molecular states. In order to observe the equilibrated density distribution, a favorable ratio of lifetime to equilibration time is required. Since the lifetime depends on the interaction strength, we have the upper limit for the interaction strength where we are able observe the equilibrated density profile.

Second, the achievable lowest temperature is much higher than that of attractive interaction case. The interaction strength between atoms at the preparation stage is much smaller in repulsive case, so that thermalization during evaporation is less effective. Then, why is this a problem? In Ref. [45], they used Thomas-Fermi radius in order to determine the global chemical potentials for each state. It was possible because the temperature is an order of magnitude lower than our case. Determining Thomas-Fermi radius only requires finding the radius where the density becomes zero. In finite temperature case, on the other hand, we need to fit at least some range of the profile in order to determine the global chemical potential. For non-interacting case, it is easy because we know exact function of the density profile. However, for strongly interacting case, the exact equation of state is unknown, so that we need to fit the wing of the cloud where the interaction is small enough for the known perturbation correction. In addition, the temperature can not be measured at the fully polarized wings as in Ref. [45] because the finite temperature profiles don't show the fully polarized features clearly, due to the extended wings.

In the next chapter, we check the upper limit for the interaction strength where we are able observe the equilibrated density profile. Then, we measure the compressibility of the Fermi gas with repulsive interaction. The compressibility measurement does not require the population imbalance nor the absolute value of the global chemical potentials. Thus, the compressibility can be measured more simply than the susceptibility when we introduce the repulsive interaction.

Chapter 5

Compressibility of an Ultracold Fermi Gas with Repulsive Interactions

As we reviewed in chapter 1.2, the two-component Fermi gases with repulsive interaction are unstable because they are realized on the so-called upper branch of a Feshbach resonance where decay is always possible into the so-called lower branch which consists of weakly bound molecular states. In order to observe the equilibrated density distribution, a favorable ratio of lifetime to equilibration time is required. Since the lifetime depends on the interaction strength, we have the upper limit for the interaction strength where we are able observe the equilibrated density profile.

Here we check the upper limit for the interaction strength where we are able observe the equilibrated density profile. Through this we test the feasibility of experiments requiring equilibrated density profiles of ultracold Fermi gases with repulsive interactions.

For weakly interacting gases, interaction effects can be explained by perturbative corrections (see chapter 2.4). For bosons, the first beyond mean-field correction, the so-called Lee-Huang-Yang term, could be observed, but corrections were necessary to account for the non-equilibrium profile since the time to sweep to strong interactions was not long compared to equilibration times and inverse loss rates [47].

Here we study fermions with repulsive interactions. Within a limited window for metastability, we can observe equilibrated clouds and characterize the repulsive interactions by obtaining the compressibility from observed profiles. We observe the linear term in $k_F a$ corresponding to mean-field energy for the first time in density profiles. In contrast to a Bose-Einstein condensate, the mean-field energy is smaller than the kinetic energy and also competes with thermal energy, and is therefore much more difficult to observe. The signal-to-noise ratio (and some heating) prevented us from discerning the second-order interaction term which is the Lee-Huang-Yang correction for fermions.

Our work features one technical novelty, a novel implementation of phase-contrast imaging to address dispersive distortions of the cloud. All studies mentioned above, with one exception [61], were conducted using resonant absorption where dispersion (an index of refraction different from one) is absent. However, this severely limits the cloud size and number of atoms to optical densities of a few. Phase-contrast imaging has many advantages. It can be applied to clouds with much larger optical densities by adjusting the detuning. Due to coherent forward scattering, the heating effect per detected signal photon is reduced by potentially a large number (which is equal to the resonant optical density divided by four [33]). This can e.g. be used for repeated nondestructive imaging. However, for precision studies of density profiles, small dispersive distortions of the density profile cannot be neglected. Previous work including Ref. [61] was not sensitive to this effect. We have developed an experimental technique to correct for dispersion.

The experiment was reported in the publication:

- Ye-Ryoung Lee, Myoung-Sun Heo, Jae-Hoon Choi, Tout T. Wang, Caleb A. Christensen, Timur M. Rvachov, and Wolfgang Ketterle
  Compressibility of an ultracold Fermi gas with repulsive interactions
  Phys. Rev. A 85, 063615 (2012). Included in appendix E.

5.1 Experimental Procedure

An evaporative cooled balanced mixture of $|1\rangle$ and $|2\rangle$ spin states is prepared at 528 G. In order to introduce repulsive interaction, we increase the magnetic field.

For loss rate measurements, the magnetic field is quickly ramped to the target field. For compressibility measurements, the field is ramped up over 50 ms and held for 30 ms to ensure thermal equilibrium before imaging. The molecular fraction in the density profile is determined by dissociating molecules with a magnetic field jump to 20 G above the Feshbach resonance, and comparing with the atom number after jumping to 528 G where the cross section for imaging molecules vanishes (see Ref. [74]).

5.2 Loss Rate

In this section, the feasibility of the experiment is tested through loss rate measurement. As expected we find only a limited window for metastability where we can observe equilibrated clouds and characterize the repulsive interactions by obtaining the compressibility from observed profiles. For interaction parameters $k_F a > 0.25$ fast decay of the gas prevents the observation of equilibrium profiles.

5.2.1 Loss Rate Estimation

To obtain thermodynamic parameters from atomic density profiles requires equilibration. One time scale for equilibration is set by the longest trap period, which is 30 ms for the axial direction. Ref. [47] studied the distortions of profiles of bosonic ^{7}Li due to non-adiabatic ramping of the scattering length. The authors found that ramping times longer than $\approx 6\pi/\omega$ (which is 90 ms for our parameters) led to only small deviations from equilibrium profiles. Here, ω is the smallest of trapping frequencies, which sets the timescale for equilibration. Assuming that losses sharply increase during the last 5 ms of the ramp towards stronger interactions and limiting tolerable losses to 10 % leads to an estimate of a maximum tolerable loss rate of about 0.02/ms. The fastest relaxation time for excitations created during a non-adiabatic ramp is $1/\omega$ (the damping time for a harmonic oscillator at critical damping). Allowing ~ 10 % loss during this time, leads to an identical estimate for the tolerable loss rate of $\sim$ 0.02/ms.

5.2.2 Loss Rate Measurement

We measured loss rate as a function of interaction strength ${k_F}^0 a$. Note that ${k_F}^0$ is the Fermi wave vector of the zero temperature noninteracting gas calculated at the trap center using total atom number. The real k_F is somewhat smaller because repulsive interactions and non-zero temperature lower the density.

First, in Fig. 5-1(a) we measured the number of atoms right before and after the fastest possible ramp (limited to 7 ms by eddy currents) to the target magnetic field. During the ramp to the target magnetic field of ${k_F}^0 a \approx 0.8$, ~ 35 % of the sample is lost. Measuring the loss rate at higher ${k_F}^0 a$ is difficult because most of the sample is lost even before reaching the target fields. The loss rate was determined by monitoring the drop in the number of atoms immediately after the field ramp. The results in Fig. 5-1(b) show that the measured loss rate reaches the maximum tolerable value of 0.02/ms at ${k_F}^0 a \approx 0.35$, limiting our measurements of equilibrium density profiles to smaller values of ${k_F}^0 a$. Furthermore, at the same values of ${k_F}^0 a$, the molecular fraction when we measure equilibrium density profiles exceeded 10 % (see Fig. 5-1(c)). As we shall discuss in section 5.5 the presence of a molecular component affects the compressibility measurement.

5.3 Compressibility Measurement

A system is characterized by its equation of state. The equation of state can be expressed in different forms involving various thermodynamic variables including density, energy, pressure, temperature and entropy. For cold atom experiments, density, chemical potential (through the trapping potential) and temperature are directly accessible to measurement. In the weakly interacting regime, the interaction manifests

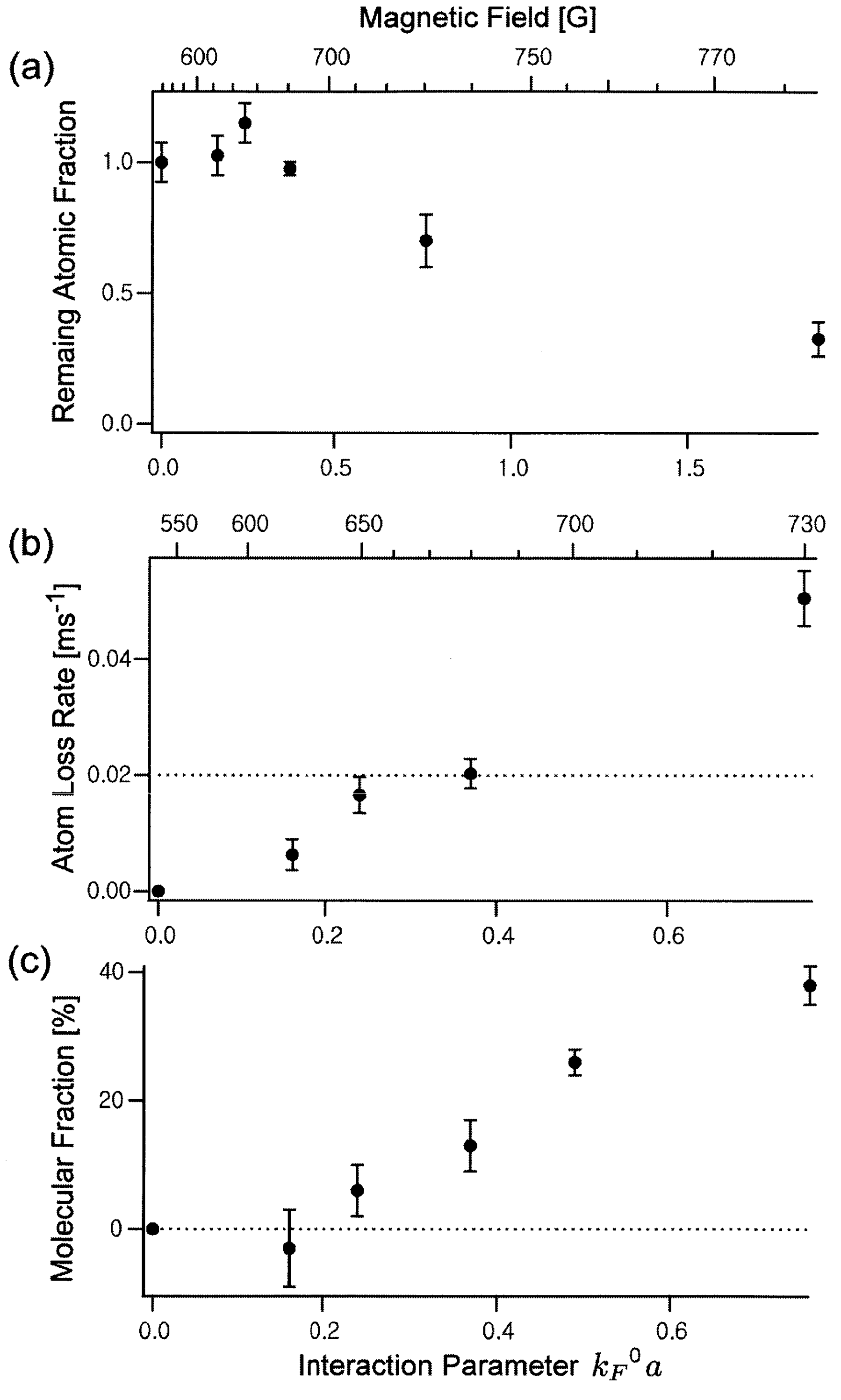

Figure 5-1: Characterizing atomic loss for increasing repulsive interactions. (a) Remaining fraction of atom number immediately after the fastest possible ramp to the target field. (b) Atom loss rates at the target fields. Dashed line shows the estimated maximum tolerable loss rate of 0.02 /ms. (c) Molecular fraction after the 50 ms ramp and 30 ms wait time, corresponding to when we measure equilibrium atomic density profiles.

itself as a perturbative term in the equation of state. Here we measure this perturbative interaction effect by measuring the derivative of density with chemical potential, the isothermal compressibility of the gas. We prepare the system at the lowest temperature, but due to heating of the cloud by molecule formation, we have to apply a correction for the measured finite temperature.

5.3.1 Measurement Method

Using the experimental procedure discussed above we prepared equilibrated clouds at various magnetic fields and measured line-of-sight integrated profiles of column density using in situ phase-contrast imaging [64]. The signal-to-noise was improved by averaging the column density along equipotential lines (which are ellipses for the anisotropic harmonic oscillator potential). The averaging region was restricted to an axial sector of ±60° to avoid corrections due to transverse anharmonicities [63]. Three-dimensional density profiles $n(r)$ were reconstructed by applying the inverse Abel transformation to the column densities $\tilde{n}(r)$ [64].

The isothermal compressibility is obtained from a spatial derivative of $n(r)$, since in the local density approximation, the local chemical potential is $\mu = \mu_o - m\omega^2 x^2/2$, where μ_o is the global chemical potential and ω the trap frequency. The compressibility is defined as

$$\kappa = \frac{1}{n^2}\frac{\partial n}{\partial \mu}. \tag{5.1}$$

We normalize the compressibility κ by the compressibility of an ideal gas at the given density and zero temperature $\kappa_o = \frac{n^{1/3}}{n^2}\frac{3m}{\hbar^2(6\pi^2)^{2/3}}$, and obtain the normalized compressibility,

$$\tilde{\kappa} = \frac{\kappa}{\kappa_o} = \frac{\hbar^2(6\pi^2)^{2/3}}{2m}\frac{\partial n^{2/3}}{\partial \mu}. \tag{5.2}$$

Here n is density, and m is the atomic mass. The normalized compressibility is obtained as the slope in a plot of $n^{2/3}$ vs. μ (Fig. 2). This plot is in essence the observed density profile plotted with the central region to the left and the spatial wings to the right. Experimentally, we find the slope to be constant over an extended range of the density profile. Compressibilities were determined from fits to the slope in the region of 90 to 50 % of the peak density. The region near the center of the cloud was excluded since the center is singular for the inverse Abel transformation leading to excessive noise. These compressibilities should be regarded as average values over the density range used in the fit. The uncertainty of fitting the slope to a single profile was 4.5 %. By averaging the profiles obtained from 20 images, the uncertainty was improved to 1.3 %.

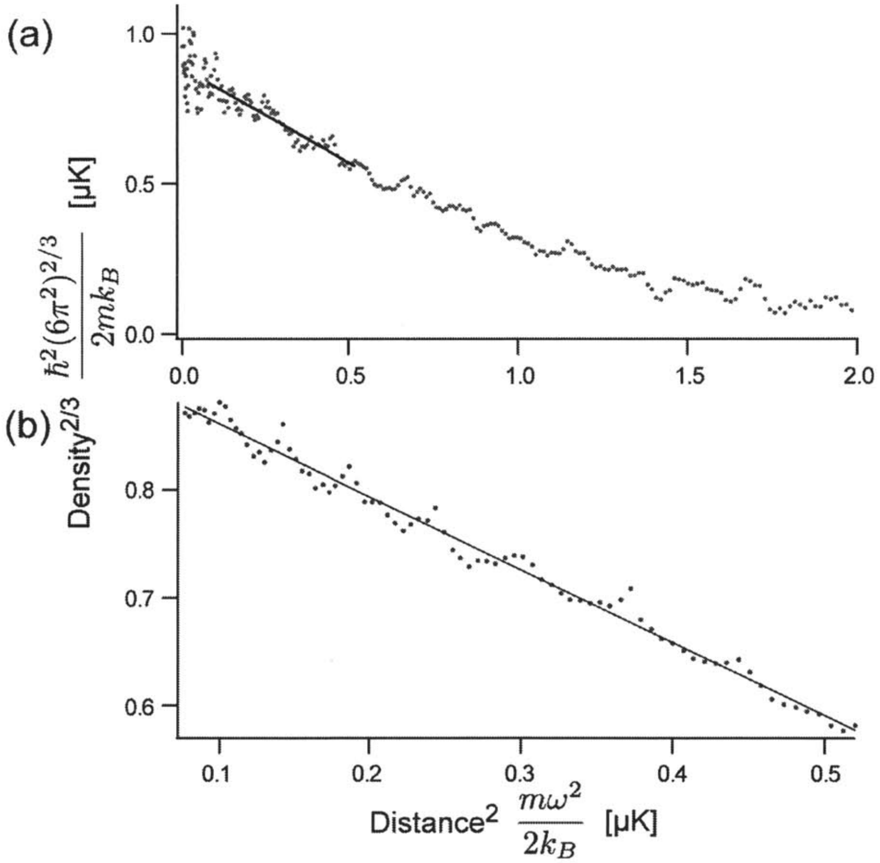

Figure 5-2: Determination of the compressibility of repulsively interacting Fermi gases. The compressibility is the slope of a graph showing the density to the power 2/3 versus the square of the distance from the center. (a) Single shot density profile. (b) Close-up of the region used for determining the compressibility for a plot showing the average of 20 density profiles.

5.3.2 Temperature Measurement

The normalized compressibility is a function of T/T_F and $k_F a$. At finite temperature and scattering length a, T/T_F and $k_F a$ change across a single density profile because T_F and k_F depend on the local density. However, this density dependence is small near the center of the cloud. Simulated density profiles showed that the average compressibility determined in the way described above agrees to within 0.6 % with the compressibility at T/T_F and $k_F a$ at the density in the center of the selected range.

Compressibility decreases for stronger repulsion, but also for higher temperature. To identify the effect of repulsive interaction requires a careful consideration of finite temperature effects. First, the temperature of the cloud had to be accurately determined. This can be done without any special assumptions by fitting the wings of the cloud using a virial expansion [67], by thermometry with another co-trapped atom [44], or for population imbalanced clouds by fitting the wings of the majority component which is an ideal Fermi gas [73]. Here we chose to determine temperature using a virial expansion,

$$p\frac{\lambda^3}{k_B T} = e^{\beta\mu} + b_2 e^{2\beta\mu} + O(e^{3\beta\mu}), \tag{5.3}$$

where $\lambda=\sqrt{\frac{2\pi\hbar^2}{mk_BT}}$ is the thermal de Broglie wavelength, b_2 is the virial coefficient, and $e^{\beta\mu}$ is the fugacity. The virial coefficient for the Fermi gas with repulsive interaction is $b_2 = -2^{-5/2} - a/\lambda$ [39]. Pressure p was obtained from the doubly-integrated density profiles [27]. Temperature was determined in the wings of the profile where $\beta\mu < -0.5$. Here, the temperature measured with and without the interaction term $-a/\lambda$ in b_2 differ by about 3%. This suggests that higher-order corrections from interaction term will be negligible. Note that the virial expansion up to second order is valid to within 1% for the ideal gas at the density of the fitted wings.

5.3.3 Interaction Effect

The low temperature normalized isothermal compressibility of a non-interacting Fermi gas is given by the Sommerfeld expansion [68],

$$\tilde{\kappa}_{o,T} = \quad 1 - \frac{\pi^2}{12}\left(\frac{T}{T_F}\right)^2 + O\left[\left(\frac{T}{T_F}\right)^4\right], \tag{5.4}$$

where T is temperature and T_F is Fermi temperature. To add the effects of interactions, it is useful to work with the inverse normalized compressibility,

$$\frac{1}{\tilde{\kappa}} = \quad \frac{3}{2}\frac{2m}{\hbar^2(6\pi^2)^{2/3}} n^{1/3} \frac{\partial \mu(n,T,a)}{\partial n}. \tag{5.5}$$

This is a derivative of the chemical potential, which has the following expansion in temperature and scattering length,

$$\mu(n,T,a) = E_F\left[1 - \frac{\pi^2}{12}\left(\frac{T}{T_F}\right)^2 + \frac{4}{3\pi}k_F a + \frac{4(11 - 2\ln 2)}{15\pi^2}(k_F a)^2\right] + CT^2 a^2,$$

where C is constant, independent of density [50]. Therefore the inverse normalized compressibility has additive correction terms for temperature and interactions up to the second order of the interaction effect,

$$\frac{1}{\tilde{\kappa}} = \quad \frac{1}{\tilde{\kappa}_{o,T}} + Y(k_F a). \tag{5.6}$$

This equation defines $Y(k_F a)$, the interaction correction to the inverse compressibility. This term is the derivative of the interaction term of the chemical potential. In second order perturbation theory, one obtains $Y(k_F a) = \frac{2}{\pi}k_F a + \frac{8(11-2ln2)}{15\pi^2}(k_F a)^2$.

Fig. 5-3 shows the normalized compressibility, the temperature T/T_F, and the interaction correction to the inverse compressibility. The temperature increases with $k_F a$ due to the increase in three-body recombination where the binding energy of the molecules ($\hbar^2/ma^2$) is transferred to the remaining atoms. The measured temperature is higher than that in previous experiments on the repulsive side [31,57]. This differ-

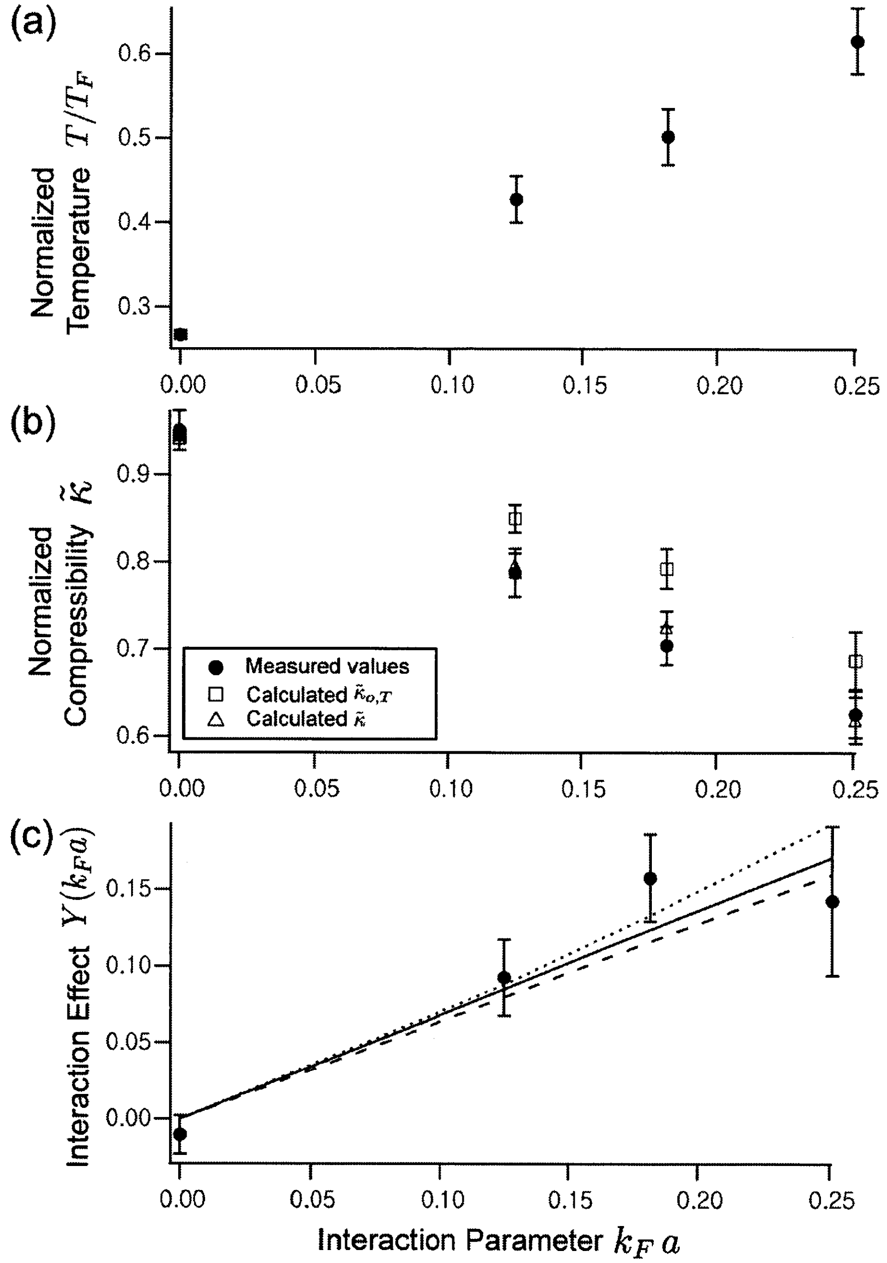

Figure 5-3: Measured temperature, normalized compressibility, and interaction effect on compressibility at various interaction strengths. (a) The measured temperature as a function of interaction strength. (b) Solid circles show the measured normalized compressibility ($\tilde{\kappa}$) and open squares show the calculated normalized compressibility at the measured temperature without interaction ($\tilde{\kappa}_{o,T}$). The difference between the two indicates the effect of interaction. Open triangles show the calculated normalized compressibility using the second order perturbation theory, which is consistent with our measured $\tilde{\kappa}$. (c) The measured interaction correction to the inverse compressibility (solid circle) is compared to a linear fit (solid line), and the first (dashed line) and the second (dotted line) order perturbative result.

ence can be explained by a smaller $k_F a$ since the increase in T/T_F is approximately proportional to $1/k_F a$ [57].

We perform a linear fit of the interaction effect $Y(k_F a)$ versus $k_F a$ (constrained to pass through the origin) and obtain 0.680±0.147 for the slope, in agreement with the perturbative prediction of $\frac{2}{\pi} = 0.637$. This is the first observation of the mean-field term for repulsively interacting fermions in a thermodynamic quantity. The repulsive interaction has been seen as line shifts in RF spectroscopy experiments (which, in contrast to many thermodynamic quantities, are measured independently of the kinetic energy of the atoms) [24, 55]. In principle, it is possible to obtain the mean-field term directly by fitting the density profiles with an extra mean field term. In such fits, we obtained clear evidence for such a term, but with low accuracy. It appears that the averaging over profiles for determining the compressibility(as in Fig. 5-2) is superior. Figure 5-3 (c) shows the predicted effect of the second-order term on $Y(k_F a)$. With some improvements in signal-to-noise ratio, one should be able to observe this term which is analogous to the Lee-Huang-Yang correction for bosons.

5.4 Dispersive Effect in Phase-Contrast Imaging

Phase-contrast imaging has several advantages over resonant absorption imaging. However, for precision studies of density profiles, small dispersive distortions of the density profile cannot be neglected. Previous work including Ref. [61] was not sensitive to this effect. We have developed an experimental technique to correct for dispersion.

Our work features one technical novelty, a novel implementation of phase-contrast imaging to address dispersive distortions of the cloud. All equation of state studies, with one exception [61], were conducted using resonant absorption where dispersion (an index of refraction different from one) is absent. However, this severely limits the cloud size and number of atoms to optical densities of a few. Phase-contrast imaging has many advantages. It can be applied to clouds with much larger optical densities by adjusting the detuning. Due to coherent forward scattering, the heating effect per detected signal photon is reduced by potentially a large number (which is equal to the resonant optical density divided by four [33]). This can e.g. be used for repeated nondestructive imaging. Thus, the phase-contrast imaging has been applied to many studies of cold Bose and Fermi gases [3,64,69]. The standard assumption has been that dispersive imaging is quantitative when the phase shift ϕ across the cloud is less than $\pi/4$. The normalized phase-contrast signal (for negligible absorption) is $3-2\sqrt{2}\cos(\phi\pm\pi/4)$, which is equal to $1\pm 2\phi$ for small phase shifts [33]. The sign depends on laser detuning and the sign of the phase shift imparted by the phase plate.

5.4.1 Phase-Contrast Imaging

All equation of state studies, with one exception [61], were conducted using resonant absorption where dispersion (an index of refraction different from one) is absent. However, this severely limits the cloud size and number of atoms to optical densities of a few. Phase-contrast imaging has many advantages. It can be applied to clouds with much larger optical densities by adjusting the detuning.

Due to coherent forward scattering, the heating effect per detected signal photon is reduced by potentially a large number (which is equal to the resonant optical density divided by four [33]). This can e.g. be used for repeated nondestructive imaging. Thus, the phase-contrast imaging has been applied to many studies of cold Bose and Fermi gases [3, 64, 69]. The standard assumption has been that dispersive imaging is quantitative when the phase shift ϕ across the cloud is less than $\pi/4$. The normalized phase-contrast signal (for negligible absorption) is $3-2\sqrt{2}\cos(\phi\pm\pi/4)$, which is equal to $1\pm 2\phi$ for small phase shifts [33]. The sign depends on laser detuning and the sign of the phase shift imparted by the phase plate.

5.4.2 Compensation for Dispersive Effect

Here, we apply phase-contrast imaging for rather precise quantitative studies of ultracold Fermi gases and found that even for small phase shifts systematic dispersive distortions of the image cannot be neglected. Phase-contrast imaging relies on column density dependent phase shifts. However, if the object is not thin, but extended along the line of sight, some lensing will affect the images. These distortions should vary inversely proportional to the probe light detuning and become negligible for far detuning.

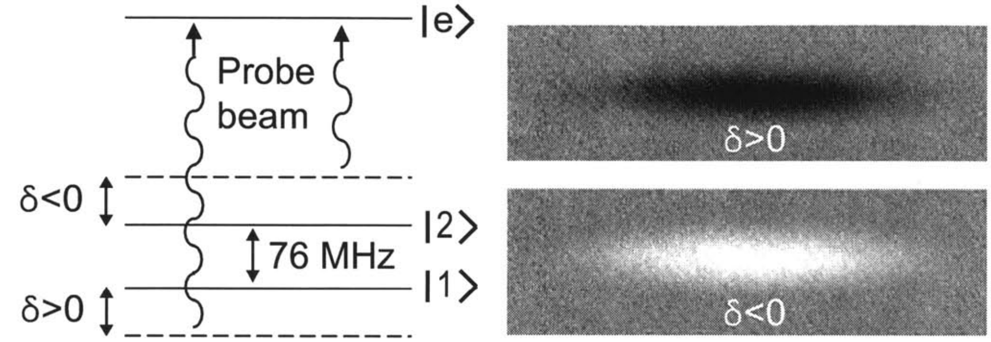

Figure 5-4: Phase-contrast imaging of a balanced spin mixture in states $|1\rangle$ and $|2\rangle$. White images (phase shift $\phi > 0$) were obtained for a probe beam red-detuned from the $|2\rangle \rightarrow |e\rangle$ transition, corresponding to $\delta < 0$. Black images ($\phi < 0$) were obtained for a probe beam blue-detuned from the $|1\rangle \rightarrow |e\rangle$ transition, corresponding to $\delta < 0$.

We investigated positive and negative detuning of 40, 80, and 120 MHz (see Fig. 5-4). The normalized phase contrast image had a maximum signal of 0.35/1.85, 0.55/1.6, and 0.7/1.4 for the three positive/negative detuning. The lensing effect is opposite (focusing vs. defocusing) for positive and negative detuning, and can therefore be identified by comparing profiles obtained with positive and negative detuning. Fig. 5-5 shows that at 40 MHz, the two profiles show a visible difference, but for profiles at 80 MHz and 120 MHz, the differences are smaller than the noise level.

However, the compressibility is determined by the slope of the profiles and very sensitive to small distortions even if they are not perceptible in the profiles. Fig. 5-5(c) shows that even at 120 MHz detuning, the compressibilities obtained from profiles with the two signs of the detuning differ by about 10 %. Since further detuning would have resulted in a smaller signal we evaluated the average value of the compressibility for positive and negative. When the dispersive distortions are small, the effect on the compressibility should be a first-order effect in the phase shift and cancel for

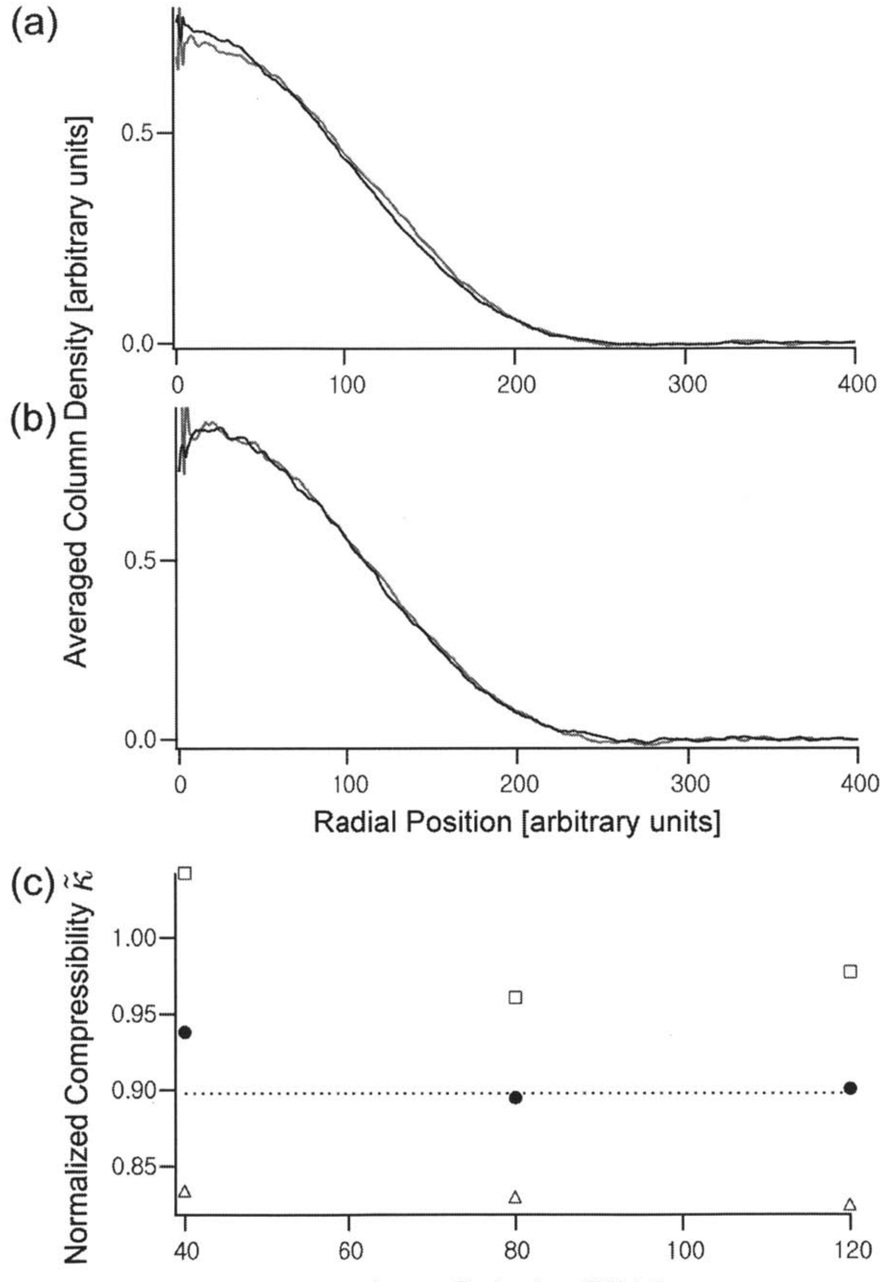

Figure 5-5: Comparison of column density profiles obtained from positive and negative detuning of (a) 40 and (b) 80 MHz, respectively. (c) The measured compressibility (at $k_F a = 0$) from positive (open triangle) and negative (open square) detuned profiles and their averages (solid circle) are shown. The average value stays constant above 80 MHz detuning.

the average. Indeed, the average value stays constant above 80MHz detuning. Our conclusion is that for reasonable signal levels (i.e. 50 % of the baseline set by the probe light) dispersive effects are relevant for quantitative studies, but can be eliminated by performing averages over positive and negative detunings. The best solution would be using double shutter imaging with the positive and negative detunings. Then, we can find both positive and negative detuned profiles from a single atomic sample, so that we can correct the dispersive effect in each profile. However, this is technically complicated because it requires about 240 MHz imaging frequency change in about 10 μs. We use tandem AOM setup for double shutter imaging, but the frequency range is about 80 MHz with 80 MHz AOMs.

5.4.3 Imaging Focus Fine Tuning

We could take advantage of the lensing effect for imaging focus fine tuning. Since positive and negative detuning result in opposite lensing effect, we apply symmetrically positive and negative detuning from the resonance frequency to a single state sample using double shutter technique. We used two steps to tune the focus. For coarse tuning, we used the aspect ratio as a parameter. For our elongated cloud, negative and positive detuning gives different aspect ratio when the image is out of focus. The aspect ratio is the same when the image is in focus. For fine tuning, we divided profiles obtained with negative and positive detuning. The divided profile is flat in focus and has slope or curvature out of focus. Note that the divided profile is not perfectly flat when the detuning is large because the dispersive effect exists even at the perfect focus position.

5.5 Discussion

5.5.1 Molecular Fraction in the Density Profile

We address now to what extent a small molecular fraction contributes to the observed density profiles. The presence of molecules is unavoidable since they form during the

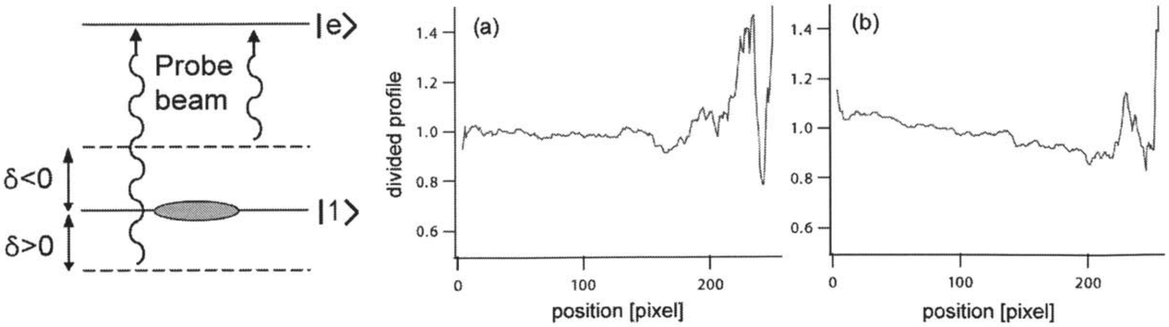

Figure 5-6: Imaging Focus Fine Tuning. We divided the black and white image of a single state sample. (a) shows the flat profile at the focus, and (b) shows slope out of focus.

ramping and equilibration time. At the highest magnetic field used in the experiment, 679 G, the molecular fraction was determined to be ~ 10 % (Fig. 1). Ref. [4] reported that molecules at 650G showed an absorption cross section of about half the value of the atoms for probe light at the atomic resonance. For phase-contrast imaging with large detuning molecules and atoms should contribute equally to the signal.

We performed simulations to address how the presence of molecules would affect the compressibility measurements. We considered as possible scenarios (i) that the molecular fraction is constant throughout the cloud, (ii) that the molecular fraction is proportional to the loss rate ($n^{8/3}$), and (iii) that the molecular fraction is well equilibrated at the same temperature as atoms. The atomic profile is then the difference of the measured density profile minus the simulated molecular density distribution. Scenario (iii) is ruled out since it would result in a rather sharp peak in the density profile which was not observed. The first two scenarios with a 10 % molecular fraction resulted in a value for the normalized compressibility which was increased by 3.3 % and 4.4 % respectively. This shows that for our largest value of $k_F a$ the presence of molecules starts to become a systematic effect. In addition to the contribution to the density profiles, molecules can affect the atomic density distribution through atom-molecule interactions.

5.5.2 Interaction Strength Limitation

Lower density

Our work shows that the interaction effect on the compressibility at the maximum possible values of $k_F a$ is about 15 %. We could identify this effect only by careful thermometry (to distinguish it from thermal effects) and by correcting small dispersive distortions of the cloud. It is desirable to study fermions for stronger repulsive interactions where stronger and non-perturbative effects are predicted. The maximum possible $k_F a$ value for obtaining equilibrium density profiles is determined by the loss rate which is proportional to $n^2 a^6 \max(T, T_F) = (k_F a)^6 n^{2/3}$ [18, 52]. Therefore, the maximum possible $k_F a$ for a given loss rate is proportional to $n^{-1/9}$ and stronger interaction effects can be seen at lower density. This should be accomplished by reducing the radial confinement and not the axial confinement which determines the equilibration time. However, the weak density dependence will allow only modest increases in $k_F a$. A recent experiment used density ten times smaller than ours [57] and reported ramping from ${k_F}^0 a = 0$ to ${k_F}^0 a = 0.35$ in 500 ms losing only 5 % atoms. Assuming the loss happened during the last 50 ms, we can roughly estimate a loss rate of ~ 0.001 ms^{-1} at ${k_F}^0 a = 0.3$ which is lower than our measurement, consistent with the lower density.

Narrow Feshbach Resonance

Longer lifetimes for a given $k_F a$ should be realized using narrow instead of broad Feshbach resonances. For narrow Feshbach resonances the low-lying molecular state has a dominant closed-channel character. Therefore, three body recombination of atoms (which are in the open channel) has a smaller overlap to the molecular state and therefore a reduced loss rate. Recent experiments using RF spectroscopy [26, 35] confirm this. However, for such narrow resonances the zero-range approximation is no longer valid, the interaction is no longer described by the scattering length alone and becomes (through an effective range parameter) momentum dependent. As a result, the narrow Feshbach resonances realize a different Hamiltonian.

5.5.3 Outlook

We have addressed the question to what extent Fermi gases with strong interactions can be studied by observing equilibrium density profiles. The range of sufficiently long metastability to reach equilibrium is limited to values of $k_F a < 0.25$. In this range, interaction effects are comparable to thermal effects, but we were able to observe how interactions reduce the compressibility and obtained quantitative agreement with the first-order mean field term. An observation of the second order Lee-Huang-Yang correction is in experimental reach.

If experiments can be performed at stronger interactions, a natural extension of our work would be a measurement of the spin susceptibility using population imbalanced Fermi systems. This was performed recently for fermions with attractive interactions [45]. Such measurements could address the possible existence of a ferromagnetic transition in a repulsive Fermi gas [31] for which the spin susceptibility would diverge at the phase transition [54].

Chapter 6

Conclusion

Ultracold Fermi gases with repulsive interaction live on an excited branch of the states coupled by a Feshbach resonance. This branch is unstable against molecular formation. Nevertheless, the theoretical predictions of itinerant ferromagnetism in a two-component Fermi gas with repulsive interaction drew attention to this excited branch. By simulating the Stoner model, we observed the nonmonotonic features in a two-component Fermi gas near a Feshbach resonance, which agree with signatures of ferromagnetic transition. These features were not definitive evidences, and we were not able to observe ferromagnetic domains, the direct evidence of ferromagnetism. Even though it turned out later that the features were not caused by ferromagnetic transition, this pioneering experiment attracted attention to the repulsive side of the Feshbach resonance.

Since the spin susceptibility would diverge at the ferromagnetic phase transition, quantitative measurement of spin susceptibility could provide a convincing evidence for the ferromagnetic phase. This lead us to quantitative study of ultracold Fermi gases with repulsive interaction. First, we started with a non-interacting case. We could simulate the free electron gas system with ultracold atoms and measured susceptibility of ideal gas. This measured susceptibility showed excellent agreement with the calculation. This couldn't be done in condensed matter experiments because even the simplest materials still include defects or complicated interaction effect.

Then, we introduced weak repulsive interaction to the system. We checked possible window for metastability, which turned out to be $k_F a < 0.25$. Within this window, we could observe equilibrated clouds and characterize the repulsive interactions by obtaining the compressibility from observed profiles. We observe the linear term in $k_F a$ corresponding to mean-field energy for the first time in density profiles. The maximum possible $k_F a$ for a given loss rate is proportional to $n^{-1/9}$ and stronger interaction effects can be seen at lower density. The density dependence may be too small to reach sufficiently strong interaction, but at least an observation of the second order Lee-Huang-Yang correction is in experimental reach. If it is possible to reach sufficiently strong interaction, measuring the spin susceptibility could provide possible evidence of a ferromagnetic phase transition.

One of the important findings of this thesis work is the dispersive effect in the phase-contrast imaging. We found that the dispersive effect was inevitable even at very large detunings for quantitative studies. The averaging method correcting for the dispersion could be improved by double shutter imaging. This would require fast switching technique between two probe beam frequencies which are far detuned to each other.

Appendix A

Tips for Precise Imaging

I list a few tips for precise imaging which can be easily overlooked.

- Fine tweak the polarization of the imaging beam.
- Block all stray light along the beam/image path.
- Carefully find the center of the phase spot, so that the phase plate does not create any fringes.
- Tilt all the optics slightly, so that no back reflection creates any fringes.
- Be careful with the imaging beam intensity (see details in the following section).

A.1 Imaging Beam Intensity

For careful imaging of atom clouds, we need to be careful with the intensity of the probe beam and the total number of photons absorbed by each atom during probing.

The intensity of the light has to be much smaller than the saturation intensity, I_{SAT}. For resonant probe beam, the saturation intensity is

$$I_{SAT} = \frac{\hbar\omega\Gamma}{2\sigma_o}, \tag{A.1}$$

where $\sigma_o = \frac{3}{2\pi}\lambda^2$. Since Γ is $2\pi\times$ 6 MHz for lithium, I_{SAT} is about 2.6 mW/cm^2. For probe beam with detuning δ (as in phase-contrast imaging), the saturation intensity is

$$I_{SAT} = \frac{\hbar\omega\Gamma}{2\sigma_o}(1 + (\frac{2\delta}{\Gamma})^2). \tag{A.2}$$

This assumes that the polarization of the light matches the transition polarization. If not, only the useful portion of the polarization should be considered. In addition, this is valid only for the cycling transition.

We need to consider the total number of photons absorbed by each atom because the absorption of photons results in atoms' recoil. The recoil velocity can be calculated from

$$mv_{recoil} = \frac{\hbar\omega}{c}. \tag{A.3}$$

For lithium, v_{recoil} is about 10 cm/s. The mean velocity in one direction is

$$\overline{v}_{recoil} = \frac{\sqrt{N}}{3}v_{recoil}, \tag{A.4}$$

where N is the number of recoils. If we limit the recoil displacement of atoms to 1 μm during 10 μs of probing, 10 photon absorption per atom is allowed. Assuming random walk, the number of recoil can be determined by

$$N_{recoil} = I\frac{\sigma_o}{1 + (\frac{2\delta}{\Gamma})^2}t_{probe}, \tag{A.5}$$

where I is intensity of the probe beam and t_{probe} is probing time.

Appendix B

Exact Breit-Rabi Formula for the Ground States of ^{6}Li

In order to know the exact rf frequencies for single-photon transitions between ground states of ^{6}Li, we use the Breit-Rabi formula,

$$E(m_F) = -\frac{1}{2}\frac{\Delta E}{2I+1} - g_I \mu_B B m_F \pm \frac{\Delta E}{2}\sqrt{1 + \frac{4 m_F x}{2I+1} + x^2}, \tag{B.1}$$

where the + sign is from $F = I + 1/2$, and the − sign is for $F = I - 1/2$, ΔE is the zero field energy separation, $ah\left(\frac{2I+1}{2}\right)$, and $x = \frac{(g_e + g_I)\mu_B B}{\Delta E}$.

For the ground states of ^{6}Li, useful numbers for the calculation are summarized in Table B.1. Physical constants from Ref. [43] and ^{6}Li magnetic moment from Ref. [29] are used.

Table B.1: Constants for ^{6}Li Breit-Rabi formula

Quantity	**Numerical value**
g_I	4.47701×10^{-4}
g_e	2.0023193043622
μ_B	1.399624604 MHz/G
ΔE	228.20527 MHz

Appendix C

RF Antenna in BEC3's Main Chamber

The main chamber of BEC3 was originally designed for RF evaporation. Thus, the antenna inside the chamber was designed with the resonant frequency being around 30 MHz. In order to optimize the antenna for lithium hyperfine state transitions, we tried to match the resonant frequency of the antenna to around 80 MHz by impedance matching. We could shift the resonant frequency using capacitors and inductors with a toy antenna which has the same dimension as the one in the chamber. However, this was not successful for the antenna in the vacuum chamber probably due to various structures and connections in the chamber.

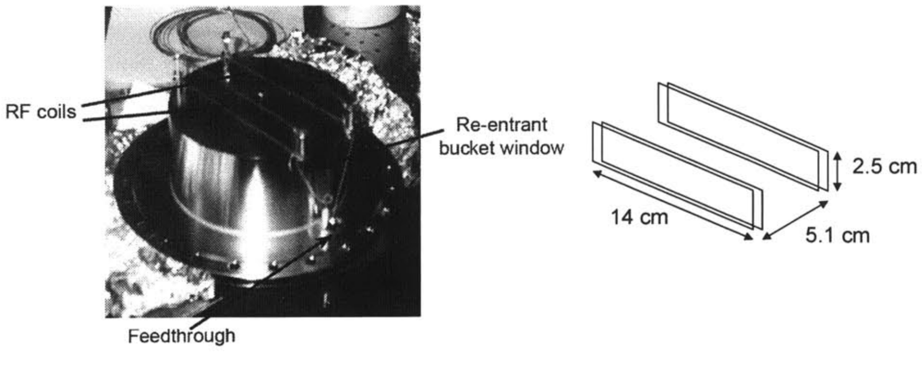

Figure C-1: Dimensions of RF antenna in BEC3's main chamber.

Appendix D

Itinerant Ferromagnetism in a Fermi Gas of Ultracold Atoms

This appendix contains a reprint of Ref. [31]: Gyu-Boong Jo, Ye-Ryuoung Lee, Jae-Hoon Choi, Caleb A. Christensen, Tony H. Kim, Joseph H. Thywissen, David E. Pritchard and Wolfgang Ketterle, *Itinerant Ferromagnetism in a Fermi Gas of Ultracold Atoms*, Science **325** , 1521-1524 (2009).

ble spectra could easily push this effect to higher frequencies that are beneficial for a variety of practical applications (*30*).

References and Notes

1. D. Schurig, J. B. Pendry, D. R. Smith, *Opt. Express* **15**, 14772 (2007).
2. A. V. Kildishev, W. Cai, U. K. Chettiar, V. M. Shalaev, *N. J. Phys.* **10**, 115029 (2008).
3. J. B. Pendry, D. Schurig, D. R. Smith, *Science* **312**, 1780 (2006).
4. Z. Liu, H. Lee, Y. Xiong, C. Sun, X. Zhang, *Science* **315**, 1686 (2007).
5. H.-T. Chen *et al.*, *Appl. Phys. Lett.* **93**, 091117 (2008).
6. J. N. Gollub, J. Y. Chin, T. J. Cui, D. R. Smith, *Opt. Express* **17**, 2122 (2009).
7. H.-T. Chen *et al.*, *Nature Photon.* **2**, 295 (2008).
8. I. Gil *et al.*, *Electron. Lett.* **40**, 1347 (2004).
9. M. M. Qazilbash *et al.*, *Appl. Phys. Lett.* **92**, 241906 (2008).
10. W. J. Padilla, A. J. Taylor, C. Highstrete, L. Mark, R. D. Averitt, *Phys. Rev. Lett.* **96**, 107401 (2006).
11. A. Degiron, J. J. Mock, D. R. Smith, *Opt. Express* **15**, 1115 (2007).
12. T. Driscoll *et al.*, *Appl. Phys. Lett.* **93**, 024101 (2008).
13. I. V. Shadrivov, N. A. Zharova, A. A. Zharov, Y. S. Kivshar, *Phys. Rev. E Stat. Nonlin. Soft Matter Phys.* **70**, 046615 (2004).
14. T. Driscoll *et al.*, *Appl. Phys. Lett.* **91**, 062511 (2007).
15. M. Di Ventra, Y. V. Pershin, L. O. Chua, *Proc. IEEE* **97**, 1371 (2009).
16. Materials and methods are available as supporting material on *Science* Online.
17. A. Zylbersztejn, N. F. Mott, *Phys. Rev. B Solid State* **11**, 4383 (1975).
18. B.-G. Chae, H.-T. Kim, D.-H. Youn, K.-Y. Kang, *Physica B* **369**, 76 (2005).
19. S. Lysenko *et al.*, *Appl. Surf. Sci.* **252**, 5512 (2006).
20. M. M. Qazilbash *et al.*, *Science* **318**, 1750 (2007).
21. T. Driscoll, H. T. Kim, B. G. Chae, M. Di Ventra, D. N. Basov, *Appl. Phys. Lett.* **95**, 043503 (2009).
22. R. Lopez, L. A. Boatner, T. E. Haynes, R. F. Haglund Jr., L. C. Feldman, *Appl. Phys. Lett.* **85**, 1410 (2004).
23. G. V. Eleftheriades, O. Siddiqui, A. K. Iyer, *Microwave Wireless Compon. Lett. IEEE* **13**, 51 (2003).
24. J. D. Baena *et al.*, *Microwave Theory Tech. IEEE Trans.* **53**, 1451 (2005).
25. S. Tretyakov, http://arxiv.org/abs/cond-mat/0612247 (2006).
26. J. J. Yang *et al.*, *Nat. Nanotechnol.* **3**, 429 (2008).
27. Y. Muraoka, Z. Hiroi, *Appl. Phys. Lett.* **80**, 583 (2002).
28. H.-T. Kim *et al.*, *N. J. Phys.* **6**, 52 (2004).
29. I. Shadrivov, *SPIE Newsroom* doi:10.1117/2.1200811.1390 (2008).
30. V. M. Shalaev, *Nature Photon.* **1**, 41 (2007).

31. This work is supported by the U.S. Department of Energy (DOE), the Air Force Office of Scientific Research (AFOSR), and ETRI. Work at UCSD on VO_2 was supported by DOE–Basic Energy Sciences and the metamaterials work was supported by AFOSR and ETRI. M.D. acknowledges partial support from NSF. H.K. acknowledges research support from a project of the Ministry of Knowledge Economy in Korea.

Supporting Online Material

www.sciencemag.org/cgi/content/full/1176580/DC1
Materials and Methods
Fig. S1
Table S1
References

20 May 2008; accepted 4 August 2009
Published online 20 August 2009;
10.1126/science.1176580
Include this information when citing this paper.

Itinerant Ferromagnetism in a Fermi Gas of Ultracold Atoms

Gyu-Boong Jo,[1]* Ye-Ryoung Lee,[1] Jae-Hoon Choi,[1] Caleb A. Christensen,[1] Tony H. Kim,[1] Joseph H. Thywissen,[2] David E. Pritchard,[1] Wolfgang Ketterle[1]

Can a gas of spin-up and spin-down fermions become ferromagnetic because of repulsive interactions? We addressed this question, for which there is not yet a definitive theoretical answer, in an experiment with an ultracold two-component Fermi gas. The observation of nonmonotonic behavior of lifetime, kinetic energy, and size for increasing repulsive interactions provides strong evidence for a phase transition to a ferromagnetic state. Our observations imply that itinerant ferromagnetism of delocalized fermions is possible without lattice and band structure, and our data validate the most basic model for ferromagnetism introduced by Stoner.

Magnetism is a macroscopic phenomenon with its origin deeply rooted in quantum mechanics. In condensed-matter physics, there are two paradigms for magnetism: localized spins interacting via tunneling and delocalized spins interacting via an exchange energy. The latter gives rise to itinerant ferromagnetism, which is responsible for the properties of transition metals such as cobalt, iron, and nickel. Both kinds of magnetism involve strong correlations and/or strong interactions and are not yet completely understood. For localized spins, the interplay of magnetism with d-wave superfluidity and the properties of frustrated spin materials are topics of current research. For itinerant ferromagnetism (*1*–*7*), phase transition theories are still qualitative.

We implemented the Stoner model, a textbook Hamiltonian for itinerant ferromagnetism (*8*), by using a two-component gas of free fermions with short-range repulsive interactions, which can capture the essence of the screened Coulomb interaction in electron gases (*8*). However, there is no proof so far that this simple model for ferromagnetism is consistent when the strong interactions are treated beyond mean-field approaches. It is known that this model fails in one dimension, where the ground state is singlet for arbitrary interactions, or for two particles in any dimension (*3*). In our work, cold atoms were used to perform a quantum simulation of this model Hamiltonian in three dimensions, and we showed experimentally that this Hamiltonian leads to a ferromagnetic phase transition (*2*). This model was also realized in helium-3 (*9*), but the liquid turn into a solid phase and not into a ferromagnetic phase at high pressure. It has also been applied to neutrons in neutron stars (*10*).

To date, magnetism in ultracold gases has been studied only for spinor (*11*, *12*) and dipolar (*13*) Bose-Einstein condensates (BECs). In these cases, magnetism is driven by weak spin-dependent interactions, which nevertheless determine the structure of the condensate because of a bosonic enhancement factor. In contrast, here we describe the simulation of quantum magnetism in a strongly interacting Fermi gas.

An important recent development in cold atom science has been the realization of superfluidity and the BEC–Bardeen-Cooper-Schrieffer (BCS) crossover in strongly interacting, two-component Fermi gases near a Feshbach resonance (*14*). These phenomena occur for attractive interactions for negative scattering length and for bound molecules (corresponding to a positive scattering length for two unpaired atoms). Very little attention has been given to the region of atoms with strongly repulsive interactions. One reason is that this region is an excited branch, which is unstable against near-resonant three-body recombination into weakly bound molecules. Nevertheless, many theoretical papers have proposed a two-component Fermi gas near a Feshbach resonance as a model system for itinerant ferromagnetism (*15*–*22*), assuming that the decay into molecules can be sufficiently suppressed. Another open question is the possibility of a fundamental limit for repulsive interactions. Such a limit due to unitarity or many-body physics may be lower than the value required for the transition to a ferromagnetic state. We show that this is not the case and that there is a window of metastability where the onset of ferromagnetism can be observed.

A simple mean-field model captures many qualitative features of the expected phase transition but is not adequate for a quantitative description of the strongly interacting regime. The total energy of a two-component Fermi gas of average density n (per spin component) in a volume V is given by $E_F 2Vn\left\{\frac{3}{10}\left[(1+\eta)^{5/3}+(1-\eta)^{5/3}\right]+\frac{2}{3\pi}k_F a(1+\eta)(1-\eta)\right\}$, where E_F is the Fermi energy of a gas, k_F is the Fermi wave vector of a gas, a is the scattering length characterizing short-range interactions between the two components, and $\eta = \Delta n/n = (n_1 - n_2)/(n_1 + n_2)$ is the magnetization of the Fermi gas. The local magnetization of the Fermi gas is nonzero when the gas separates into two volumes, where the densities n_1 and n_2 of the two spin states differ

---

[1] Massachusetts Institute of Technology–Harvard Center for Ultracold Atoms, Research Laboratory of Electronics, Department of Physics, Massachusetts Institute of Technology, Cambridge, MA 02139, USA. [2] Department of Physics, University of Toronto, Toronto, Ontario M5S1A7, Canada.

*To whom correspondence should be addressed. E-mail: gyuboong@mit.edu

Downloaded from www.sciencemag.org on May 31, 2011

by $2\Delta n$. We studied an ensemble in which the number of atoms in each spin state is conserved. This is equivalent to a free electron gas at zero external magnetic field where the total magnetization is zero. The interaction term represents any short-range spin-independent potential. When the gas is fully polarized, it avoids the repulsive interaction but increases its kinetic energy by a factor of $2^{2/3}$. The phase transition occurs when the minimum in energy is at nonzero magnetization (Fig. 1A) at $k_\mathrm{F}a = \pi/2$. This onset was previously discussed in the context of phase separation in a two-component Fermi gas (*15–18*). Figure 1B shows several consequences of the phase transition for a system at constant pressure. First, for increasing repulsive interactions, the gas expands, lowering its density and Fermi energy; kinetic energy is therefore reduced. When the gas enters the ferromagnetic phase, kinetic energy increases rapidly because of the larger local density per spin state. Furthermore, the volume has a maximum value at the phase transition. This can be understood by noting that pressure in our model is $(2/3)E_\mathrm{kin}/V + E_\mathrm{int}/V$, where E_kin is kinetic energy and E_int is interaction energy. At the phase transition, the system increases its kinetic energy and reduces its interaction energy, thus reducing the pressure. This maximum in pressure at constant volume turns into a maximum in volume for a system held at constant pressure or in a trapping potential. We have observed three predictions of this model: (i) the onset of local magnetization through the suppression of inelastic collisions, (ii) the minimum in kinetic energy, and (iii) the maximum in the size of the cloud. These qualitative features are generic for the ferromagnetic phase transition and should also be present in more-advanced models (*19*).

We start with an atom cloud consisting of an equal mixture of ^{6}Li atoms in the lowest two hyperfine states, held at 590 G in an optical dipole trap with additional magnetic confinement (*23*). The number of atoms per spin state is approximately 6.5×10^5, which corresponds to a Fermi temperature T_F of ~1.4 μK. The effective temperature T could be varied between $T/T_\mathrm{F} = 0.1$ and $T/T_\mathrm{F} = 0.6$ and was determined immediately after the field ramp by fitting the spatial distribution of the cloud with a finite temperature Thomas-Fermi profile. We define k_F° as the Fermi wave vector of the noninteracting gas calculated at the trap center. Applying the procedure discussed in (*24*) to repulsive interactions, we estimate that the real temperature is approximately 20% larger than the effective one. The effective temperature did not depend on $k_\mathrm{F}^\circ a$ for $k_\mathrm{F}^0 a < 6$. At higher temperatures, additional shot-to-shot noise was caused by large fluctuations in the atom number. From the starting point at 590 G, the magnetic field was increased toward the Feshbach resonance at 834 G, thus providing adjustable repulsive interactions. Because of the limited lifetime of the strongly interacting gas, it was necessary to apply the fastest possible field ramp, limited to 4.5 ms by eddy currents. The ramp time is approximately equal to the inverse of the axial trap frequency (*23*) and therefore only marginally adiabatic. Depending on the magnetic field during observation, either atoms or atoms and molecules were detected by absorption imaging as described in fig. S1 (*25*).

The emergence of local spin polarization can be observed by the suppression of (either elastic or inelastic) collisions, because the Pauli exclusion principle forbids collisions in a fully polarized cloud. We monitored inelastic three-body collisions, which convert atoms into molecules. The rate (per atom) is proportional to $f(a,T)n_1n_2$ or $f(a,T)\ n^2(1 - \eta^2)$ and is therefore a measure of the magnetization η. For $k_\mathrm{F}a \ll 1$, the rate coefficient $f(a,T)$ is proportional to $a^6 \max(T,T_\mathrm{F})$ (*26*). This rate can be observed by monitoring the initial drop in the number of atoms during the first 2 ms after the field ramp. We avoided longer observation times, because the increasing molecule fraction could modify the properties of the sample.

A sharp peak appears in the atom loss rate around $k_\mathrm{F}^0 a \cong 2.5$ at $T/T_\mathrm{F} = 0.12$ (Fig. 2), indicating a transition in the sample to a state with local magnetization. The gradual decrease is consistent with the inhomogeneous density of the cloud, where the transition occurs first in the center. The large suppression of the loss rate indicates a large local magnetization of the cloud.

The kinetic energy of the cloud was determined by suddenly switching off the optical trap and the Feshbach fields immediately after the field ramp and then imaging state $|1\rangle$ atoms at zero field using the cycling transition after a ballistic expansion time of $\Delta t = 4.6$ ms. The kinetic energy was obtained from the Gaussian radial width σ_x as $E_\mathrm{kin} = [(3m\sigma_x^2)/(2\Delta t^2)]$ where m is the mass of the ^{6}Li atom. A minimum of the kinetic energy at $k_\mathrm{F}^0 a \cong 2.2$ for the coldest temperature $T/T_\mathrm{F} = 0.12$ nearly coincided with the onset of local polarization (Fig. 3). The peak in the atom loss rate occurs slightly later than the minimum of kinetic energy, probably because $f(a,T)$ increases with a (*22*). Because the temperature did not change around $k_\mathrm{F}^0 a \cong 2.2$, the increase in kinetic energy is not caused by heating but by a sudden change in the properties of the gas, which is consistent with the onset of ferromagnetism. The observed increase in kinetic energy is approximately 20% at $T/T_\mathrm{F} = 0.12$, smaller than the value $(2^{2/3} - 1) = 0.59$ predicted for a fully polarized gas. This discrepancy could be due to the absence of polarization or partial polarization in the wings of the cloud. Also, it is possible that the measured kinetic energy of the strongly interacting gas before the phase transition includes some interaction energy if the Feshbach fields are not suddenly switched off. For the current switch-off time of ~100 μs, this should be only a 5% effect, but the magnetic field decay may be slower because of eddy currents.

Finally, Fig. 4 shows our observation of a maximum cloud size at the phase transition, in agreement with the prediction of the model. The cloud size may not have fully equilibrated, because our ramp time was only marginally adiabatic, but this alone cannot explain the observed maximum.

The suppression of the atom loss rate, the minimum in kinetic energy, and the maximum in cloud size show a strong temperature dependence between $T/T_\mathrm{F} = 0.12$ and 0.22. The properties of a normal Fermi gas approaching the unitarity limit with $k_\mathrm{F}^\circ a \gg 1$ should be insensitive to temperature variations in this range; therefore, the observed temperature dependence provides further evidence for a transition to a new phase.

At higher temperature (e.g., $T/T_\mathrm{F} = 0.39$ as shown in Fig. 3), the observed nonmonotonic behavior becomes less pronounced and shifts to larger values of $k_\mathrm{F}^0 a$ for $3 \le k_\mathrm{F}^0 a \le 6$. For all three observed properties (Figs. 2 to 4), a nonmonotonic behavior is no longer observed at $T/T_\mathrm{F} = 0.55$ (*27*). One interpretation is that at this temperature and

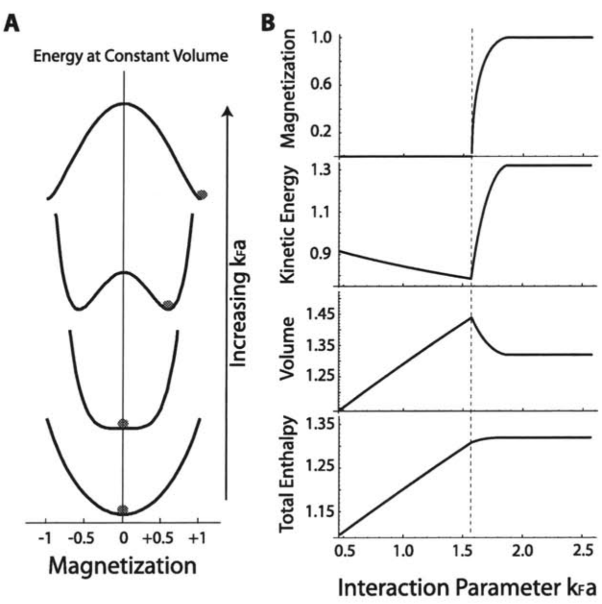

Fig. 1. Ferromagnetic phase transition at $T = 0$, according to the mean-field model described in the text. The onset of itinerant ferromagnetism occurs when the energy as a function of magnetization flips from a U shape to a W shape (**A**). (**B**) Enthalpy, volume, and kinetic energy, normalized to their values for the ideal Fermi gas, and magnetization as a function of the interaction parameter $k_\mathrm{F}a$. k_F is defined by the density of the gas. The dotted line marks the phase transition.

Downloaded from www.sciencemag.org on May 31, 2011

above, there is no longer a phase transition. In a mean-field approximation, a ferromagnetic phase would appear at all temperatures but for increasing values of $k_\mathrm{F}^0 a$. Our observations may imply that the interaction energy saturates around $k_\mathrm{F}^0 a \approx 5$.

The spin-polarized ferromagnetic state should not suffer from inelastic collisions. However, typical lifetimes were 10 to 20 ms, which were probably related to a small domain size and three-body recombination at domain walls.

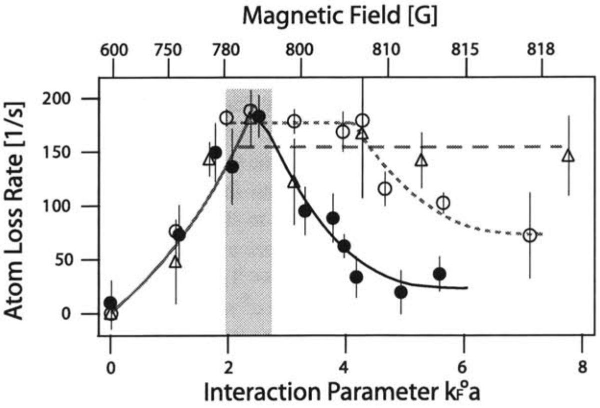

Fig. 2. Atom loss rate as a probe for local spin polarization, for different temperatures. $T/T_\mathrm{F} = 0.55$ (triangles, dashed curve), $T/T_\mathrm{F} = 0.22$ (open circles, dotted curve), and $T/T_\mathrm{F} = 0.12$ (solid circles, solid black curve). The curves are guides to the eye, based on the assumption of a loss rate that saturates for increasing *a* in the normal state. The shaded area around the phase transition at $T/T_\mathrm{F} = 0.12$ highlights the same region as in Figs. 3 and 4.

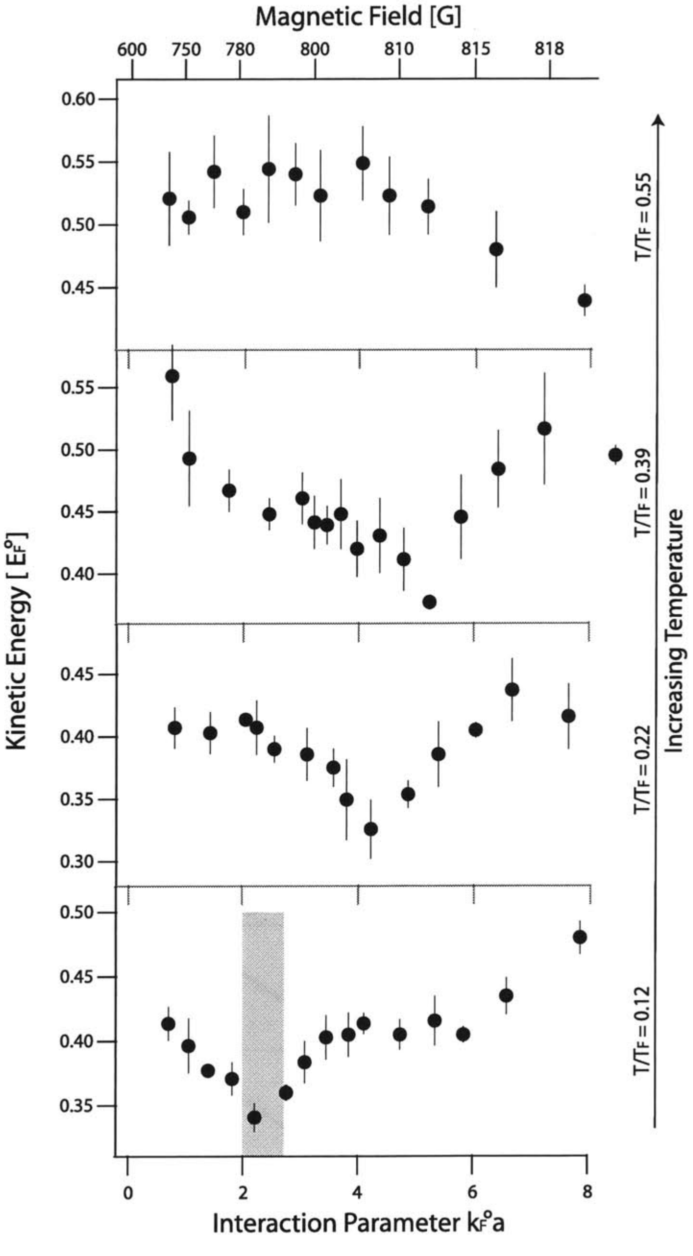

Fig. 3. Kinetic energy of a repulsively interacting Fermi gas determined for different interaction parameters $k_\mathrm{F}^0 a$ and temperatures. The measured kinetic energy is normalized by the Fermi energy E_F^0 of the noninteracting Fermi gas at $T = 0$, calculated at the trap center with the same number of atoms per spin state. Each data point represents the average of three or four measurements.

We were unsuccessful in imaging ferromagnetic domains using differential in situ phase-contrast imaging (*28*). A signal-to-noise level of ~ 10 suggests that there were at least 100 domains in a volume given by our spatial resolution of ~3 μm and by the radial size of the cloud. This implies that the maximum volume of the spin domains is ~5 μm^3, containing ~50 spin-polarized atoms. We suspect that the short lifetime prevented the domains from growing to a larger size and eventually adopting the equilibrium texture of the ground state, which has been predicted to have the spins pointing radially outward, like a hedgehog (*20*, *22*). All our measurements are sensitive only to local spin polarization and are independent of domain structure and texture.

The only difference between our experiment and the ideal Stoner model is a molecular admixture of 25% (Fig. 4). The molecular fraction was constant for $k_\mathrm{F}^0 a > 1.8$ for all temperatures and therefore cannot be responsible for the sudden change of behavior of the gas at $k_\mathrm{F}^0 a \cong 2.2$ at the coldest temperature $T/T_\mathrm{F} = 0.12$. This prediction was confirmed by repeating the kinetic energy measurements with a molecular admixture of 60%. The minimum in the kinetic energy occurred at the same value of $k_\mathrm{F}^0 a$ within experimental accuracy.

For a comparison of the observed phase transition at $k_\mathrm{F}^0 a \cong 2.2$ to the theoretical predictions, the ideal gas k_F^0 has to be replaced by the value for the interacting gas, which is smaller by ~15% because of the expansion of the cloud (Fig. 4), resulting in a critical value for $k_\mathrm{F}a \cong 1.9 \pm 0.2$. At $T/T_\mathrm{F} = 0.12$, the finite temperature correction in the critical value for $k_\mathrm{F}a$ is predicted to be less than 5% (*19*). The observed value for $k_\mathrm{F}a$ is larger than both the mean-field prediction of π/2 and the second-order prediction of 1.054 at zero temperature (*19*). Depending on the theoretical approach, the phase transition has been predicted to be first or second order. This could not been discerned in our experiment because of the inhomogeneous density of the cloud.

It has been speculated (*19*) that earlier experiments on the measurement of the interaction energy (*29*) and radio frequency spectroscopy of Fermi gases (*30*) showed evidence for the transition to a ferromagnetic state at or below $k_\mathrm{F}a = 1$. This interpretation seems to be ruled out by our experiment.

Our work demonstrates a remarkable asymmetry between positive and negative scattering length. Early work (*15*) predicted that for $k_\mathrm{F}|a| = \pi/2$, both an attractive and a repulsive Fermi gas become mechanically unstable (against collapse and phase separation, respectively). In an attractive Fermi gas, however, the mechanical instability does not occur [due to pairing (*31*)], in contrast to our observations in a repulsive Fermi gas. This suggests that the maximum total repulsive energy [in units of $3/5(2Vn)E_\mathrm{F}$] is larger than the maximum attractive energy |β| of 0.59 (*32*) that is realized for infinite *a* (*23*).

The interpretation of our results in terms of a phase transition to itinerant ferromagnetism is based on the agreement with the prediction of simplified models [Fig. 1, (*15*–*22*)]. Future

Downloaded from www.sciencemag.org on May 31, 2011

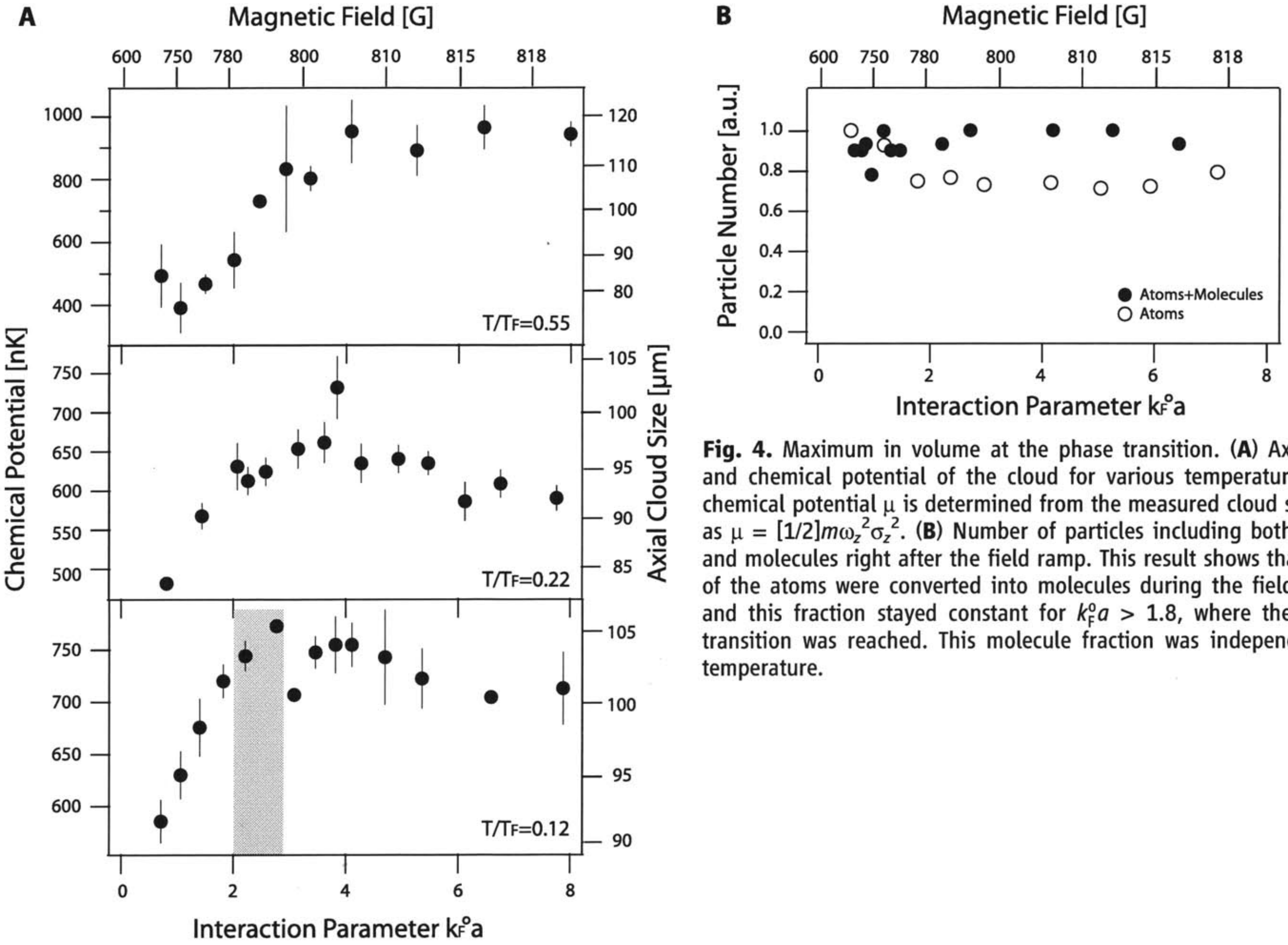

Fig. 4. Maximum in volume at the phase transition. (**A**) Axial size and chemical potential of the cloud for various temperatures. The chemical potential μ is determined from the measured cloud size, σ_z, as $\mu = [1/2]m\omega_z^2\sigma_z^2$. (**B**) Number of particles including both atoms and molecules right after the field ramp. This result shows that 25% of the atoms were converted into molecules during the field ramp, and this fraction stayed constant for $k_F^0a > 1.8$, where the phase transition was reached. This molecule fraction was independent of temperature.

Downloaded from www.sciencemag.org on May 31, 2011

work should address how the observed signatures are modified by strong interactions and correlations. Additional insight can be obtained by varying the magnetic field ramp time over a wide range and studying the relaxation toward an equilibrium state (*33*).

Heisenberg and Bloch's explanation for ferromagnetism was based on exchange energy; that is, the Pauli principle and spin-independent repulsive interactions between the electrons. However, it was unknown what other "ingredients" were needed for itinerant ferromagnetism. It was not until 1995 (*6*, *7*) that a rigorous proof was given that, in certain lattices, spin-independent Coulomb interactions can give rise to ferromagnetism in itinerant electron systems. Our finding suggests that Heisenberg's idea does not require a lattice and band structure but already applies to a free gas with short-range interactions. Our experiment can be regarded as quantum simulation of a Hamiltonian for which even the existence of a phase transition was unproven. This underlines the potential of cold atom experiments as quantum simulators for many-body physics.

References and Notes

1. F. Bloch, *Z. Phys.* **57**, 545 (1929).
2. E. Stoner, *Philos. Mag.* **15**, 1018 (1933).
3. E. Lieb, D. Mattis, *Phys. Rev.* **125**, 164 (1962).
4. P. W. Brouwer, Y. Oreg, B. I. Halperin, *Phys. Rev. B* **60**, R13977 (1999).
5. D. Vollhardt, N. Blumer, K. Held, M. Kollar, *Metallic Ferromagnetism–An Electronic Correlation Phenomenon*. vol. 580 of *Lecture Notes in Physics* (Springer, Heidelberg, Germany, 2001).
6. H. Tasaki, *Phys. Rev. Lett.* **75**, 4678 (1995).
7. A. Tanaka, H. Tasaki, *Phys. Rev. Lett.* **98**, 116402 (2007).
8. D. W. Snoke, *Solid State Physics: Essential Concepts* (Addison-Wesley, San Francisco, CA, 2008).
9. D. Vollhardt, *Rev. Mod. Phys.* **56**, 99 (1984).
10. J. Pfarr, *Z. Phys.* **251**, 152 (1972).
11. J. Stenger *et al.*, *Nature* **396**, 345 (1998).
12. L. E. Sadler, J. M. Higbie, S. R. Leslie, M. Vengalattore, D. M. Stamper-Kurn, *Nature* **443**, 312 (2006).
13. T. Lahaye *et al.*, *Nature* **448**, 672 (2007).
14. M. Inguscio, W. Ketterle, C. Salomon, *Ultracold Fermi Gases, Proceedings of the International School of Physics Ënrico Fermi, Course CLXIV* (IOS Press, Amsterdam, 2008).
15. M. Houbiers *et al.*, *Phys. Rev. A* **56**, 4864 (1997).
16. L. Salasnich, B. Pozzi, A. Parola, L. Reatto, *J. Phys. At. Mol. Opt. Phys.* **33**, 3943 (2000).
17. M. Amoruso, I. Meccoli, A. Minguzzi, M. Tosi, *Eur. Phys. J. D* **8**, 361 (2000).
18. T. Sogo, H. Yabu, *Phys. Rev. A* **66**, 043611 (2002).
19. R. A. Duine, A. H. MacDonald, *Phys. Rev. Lett.* **95**, 230403 (2005).
20. I. Berdnikov, P. Coleman, S. H. Simon, *Phys. Rev. B* **79**, 224403 (2009).
21. S. Zhang, H. Hung, C. Wu, preprint available at http://arxiv.org/abs/0805.3031v4 (2008).
22. L. J. LeBlanc, J. H. Thywissen, A. A. Burkov, A. Paramekanti, *Phys. Rev. A* **80**, 013607 (2009).
23. Materials and methods are available as supporting material on *Science* Online.
24. J. Kinast *et al.*, *Science* **307**, 1296 (2005).
25. M. W. Zwierlein *et al.*, *Phys. Rev. Lett.* **91**, 250401 (2003).
26. J. P. D'Incao, B. D. Esry, *Phys. Rev. Lett.* **94**, 213201 (2005).
27. The interpretation of the loss rate is complicated because $f(a,T)$ is unkown for $k_Fa \geq 1$. The three-body rate $f(a,T)$ is expected to be unitarity saturated for $k_Fa >> 1$ (*34*). The lines in Fig. 2 indicate that the observed loss rate is consistent with unitarity saturation and a sudden drop at the phase transition, which occurs at large values of k_Fa at higher temperature.
28. Y. Shin, M. W. Zwierlein, C. H. Schunck, A. Schirotzek, W. Ketterle, *Phys. Rev. Lett.* **97**, 030401 (2006).
29. T. Bourdel *et al.*, *Phys. Rev. Lett.* **91**, 020402 (2003).
30. S. Gupta *et al.*, *Science* **300**, 1723 (2003).
31. P. Nozières, S. Schmitt-Rink, *J. Low Temp. Phys.* **59**, 195 (1985).
32. J. Carlson, S. Reddy, *Phys. Rev. Lett.* **95**, 060401 (2005).
33. M. Babadi, D. Pekker, R. Sensarma, A. Georges, E. Demler, preprint available at http://arxiv.org/abs/0908.3483 (2009).
34. T. Weber, J. Herbig, M. Mark, H.-C. Nägerl, R. Grimm, *Phys. Rev. Lett.* **91**, 123201 (2003).
35. Supported by NSF and the Office of Naval Research, through the Multidisciplinary University Research Initiative program, and under Army Research Office grant no. W911NF-07-1-0493 with funds from the Defense Advanced Research Projects Agency Optical Lattice Emulator program. G.-B.J and Y.-R.L acknowledge additional support from the Samsung Foundation. We thank E. Demler, W. Hofstetter, A. Paramekanti, L. J. LeBlanc, and G. J. Conduit for useful discussions; T. Wang for experimental assistance; and A. Keshet for development of the computer control system.

Supporting Online Material

www.sciencemag.org/cgi/content/full/325/5947/1521/DC1
Materials and Methods
SOM Text
Fig. S1
References

1 June 2009; accepted 21 July 2009
10.1126/science.1177112

Appendix E

Compressibility of an Ultracold Fermi Gas with Repulsive Interactions

This appendix contains a reprint of Ref. [40]: Ye-Ryoung Lee, Myoung-Sun Heo, Jae-Hoon Choi, Tout T. Wang, Caleb A. Christensen, Timur M. Rvachov, and Wolfgang Ketterle, *Compressibility of an ultracold Fermi gas with repulsive interactions*, Phys. Rev. A **85**, 063615 (2012).

PHYSICAL REVIEW A **85**, 063615 (2012)

Compressibility of an ultracold Fermi gas with repulsive interactions

Ye-Ryoung Lee,[1] Myoung-Sun Heo,[1] Jae-Hoon Choi,[1] Tout T. Wang,[1,2] Caleb A. Christensen,[1] Timur M. Rvachov,[1] and Wolfgang Ketterle[1]

[1]*MIT-Harvard Center for Ultracold Atoms, Research Laboratory of Electronics, Department of Physics, Massachusetts Institute of Technology, Cambridge, Massachusetts 02139, USA*

[2]*MIT-Harvard Center for Ultracold Atoms, Department of Physics, Harvard University, Cambridge, Massachusetts 02138, USA*

(Received 18 April 2012; published 21 June 2012)

Fermi gases with repulsive interactions are characterized by measuring their compressibility as a function of interaction strength. The compressibility is obtained from in-trap density distributions monitored by phase-contrast imaging. For interaction parameters $k_F a > 0.25$, fast decay of the gas prevents the observation of equilibrium profiles. For smaller interaction parameters, the results are adequately described by first-order perturbation theory. We have developed a phase-contrast imaging method that compensates for dispersive distortions of the images.

DOI: 10.1103/PhysRevA.85.063615 PACS number(s): 03.75.Ss, 67.85.Lm, 05.30.Fk

I. INTRODUCTION

Experiments with ultracold atoms explore many-body physics with strong interactions. They have demonstrated long-predicted phenomena like the BEC-BCS crossover [1] and Lee-Huang-Yang corrections to the energy of degenerate gases [2–4]. Experiments have also explored novel quantum phases like fermions with unitarity-limited interactions [1,5], population-imbalanced Fermi gases [6,7], and Hubbard models in optical lattices [8,9]. More recently, they have been used to provide precision tests of many-body theories [5]. Usually, interactions in ultracold gases are fully described by the scattering length, which is a zero-range approximation greatly simplifying the theoretical description. This approximation is valid since the diluteness of the atomic gases implies a particle separation much larger than the short range of the van der Waals interactions. This almost exact characterization of the interactions by a single parameter, the tunability of interaction strength, and precise experimental control over cold-atom systems have made them an ideal test bed for many-body quantum calculations.

A new level of quantitative comparison between theory and experiment was recently reached by careful measurements of density profiles from which the equation of state could be determined. These techniques were first proposed by Chevy [10] and Bulgac and Forbes [11] and implemented by Shin [12]. Further improvements [4,5,13–16] resulted in impressive accuracy without adjustable parameters. These results hinge on accurate measurements of the equilibrium atomic density distribution. Since all cold-atom systems are in a metastable phase, this requires a favorable ratio of lifetime to equilibration time.

Long lifetimes and strong interactions were realized in Fermi gases with strong attractive interactions since the decay to lower-lying molecular states is suppressed by the Pauli exclusion principle [17]. This is different for repulsive interactions which are realized on the so-called upper branch of a Feshbach resonance, where decay is always possible into the so-called lower branch, which consists of weakly bound molecular states with binding energy $\hbar^2/ma^2$ where a is the scattering length.

For bosons, the first beyond-mean-field correction, the so-called Lee-Huang-Yang term, could be observed, but corrections were necessary to account for the nonequilibrium profile, since the time to sweep to strong interactions was not long compared to equilibration times and inverse loss rates [3]. Here we study fermions with repulsive interactions. They have been the focus of much recent work due to the prediction of a phase transition to a ferromagnetic state for sufficiently strong interactions [18,19]. Recent experimental [20,21] and theoretical studies [22] addressed the competition with strong decay to the lower molecular branch.

As expected we find only a limited window for metastability where we can observe equilibrated clouds and characterize the repulsive interactions by obtaining the compressibility from observed profiles. We observe the linear term in $k_F a$ corresponding to mean-field energy in density profiles. k_F is the Fermi wave vector. In contrast to a Bose-Einstein condensate, here the mean-field energy is smaller than the kinetic energy and also competes with the thermal energy, and is therefore much more difficult to observe. The signal-to-noise ratio (and some heating) prevented us from discerning the second-order interaction term which is the Lee-Huang-Yang correction for fermions.

Our work employs phase-contrast imaging using two different laser detunings to identify and correct for dispersive distortions of the cloud. All studies mentioned above, with one exception [12], were conducted using resonant absorption where dispersion (an index of refraction different from 1) is absent. However, this severely limits the cloud size and number of atoms to small optical densities. Phase-contrast imaging has many advantages. It can be applied to clouds with much larger optical densities by adjusting the detuning. Due to coherent forward scattering, the heating effect per detected signal photon is reduced by potentially a large number (which is equal to the resonant optical density divided by 4 [23]). This can, e.g., be used for repeated nondestructive imaging. However, for precision studies of density profiles, small dispersive distortions of the density profile cannot be neglected. Previous work including Ref. [12] was not sensitive to this effect. We have developed an experimental technique to correct for dispersion.

II. EXPERIMENTAL SETUP

A spin-polarized Fermi gas of ^{6}Li in the $|F = 3/2; m_F = 3/2\rangle$ state is produced by sympathetic

©2012 American Physical Society

cooling with bosonic ^{23}Na atoms in a magnetic trap as described in [24]. The ^{6}Li atoms are then loaded into a single-beam optical dipole trap and transferred into the lowest hyperfine state $|F = 1/2; m_F = 1/2\rangle$ by a Landau-Zener radio-frequency (rf) sweep. Additional axial confinement is provided by magnetic field curvature. An equal mixture of $|1\rangle$ and $|2\rangle$ spin states (corresponding to the $|F = 1/2; m_F = 1/2\rangle$ and $|F = 1/2; m_F = -1/2\rangle$ states at low magnetic field) is prepared by a rf sweep at 300 G, followed by 500 ms wait time for decoherence and evaporative cooling in the optical trap. The Feshbach resonance at 834 G [1] is used to tune the repulsive interactions between $|1\rangle$ and $|2\rangle$. We increase the magnetic field in 200 ms to 528 G, where the scattering length is zero and our Fermi gas is noninteracting. The final trap has a depth of 4.1 μK and frequencies of $\omega_x = \omega_y = 390$ Hz and $\omega_z = 34.7$ Hz. The number of atoms per spin state is 8×10^5, which corresponds to a Fermi temperature T_F of 1.4 μK. The temperature of the atoms is $0.3T_F$ at this point. For loss rate measurements, the magnetic field is quickly ramped to the target field. For compressibility measurements, the field is ramped up over 50 ms and held for 30 ms to ensure thermal equilibrium before imaging. The molecular fraction in the density profile is determined by dissociating molecules with a magnetic field jump to 20 G above the Feshbach resonance, and comparing with the atom number after jumping to 528 G where the cross section for imaging molecules vanishes (see Ref. [25]).

III. LOSS RATE

To obtain thermodynamic parameters from atomic density profiles requires equilibration. One time scale for equilibration is set by the longest trap period, which is 30 ms for the axial direction. The authors of Ref. [3] studied the distortions of profiles of bosonic ^{7}Li due to nonadiabatic ramping of the scattering length. The authors found that ramping times longer than $\approx 6\pi/\omega$ (which is 90 ms for our parameters) led to only small deviations from equilibrium profiles. Here, ω is the smallest of the trapping frequencies, which sets the time scale for equilibration. Assuming that losses sharply increase during the last 5 ms of the ramp towards stronger interactions and limiting tolerable losses to 10% leads to an estimate of a maximum tolerable loss rate of about 0.02/ms. The fastest relaxation time for excitations created during a nonadiabatic ramp is $1/\omega$ (the damping time for a harmonic oscillator at critical damping). Allowing $\sim$10% loss during this time leads to an identical estimate for the tolerable loss rate of $\sim$0.02/ms.

We measured loss rate as a function of interaction strength $k_F^0 a$. Note that k_F^0 is the Fermi wave vector of the zero-temperature noninteracting gas calculated at the trap center using total atom number. The real k_F is somewhat smaller because repulsive interactions and nonzero temperature lower the density.

First, in Fig. 1(a) we measured the number of atoms right before and after the fastest possible ramp (limited to 7 ms by eddy currents) to the target magnetic field. During the ramp to the target magnetic field of $k_F^0 a \approx 0.8$, $\sim$35% of the sample is lost. Measuring the loss rate at higher $k_F^0 a$ is difficult because most of the sample is lost even before reaching the target fields. The loss rate was determined by monitoring the drop in the number of atoms immediately after the field ramp. The results in Fig. 1(b) show that the measured loss rate reaches the maximum tolerable value of 0.02/ms at $k_F^0 a \approx 0.35$, limiting our measurements of equilibrium density profiles to smaller values of $k_F^0 a$. Furthermore, at the same values of $k_F^0 a$, the molecular fraction when we measure equilibrium density profiles exceeded 10% [see Fig. 1(c)]. As we discuss in Sec. IV the presence of a molecular component affects the compressibility measurement.

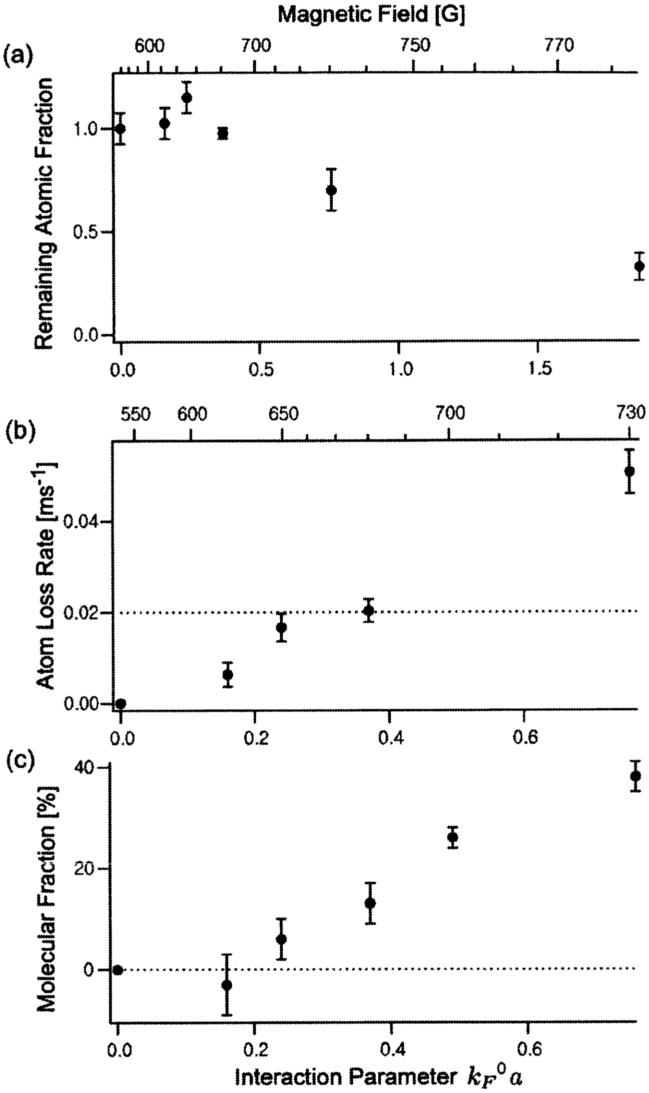

FIG. 1. Characterizing atomic loss for increasing repulsive interactions. (a) Remaining fraction of atom number immediately after the fastest possible ramp to the target field. (b) Atom loss rates at the target fields. Dashed line shows the estimated maximum tolerable loss rate of 0.02/ms. (c) Molecular fraction after the 50 ms ramp and 30 ms wait time, corresponding to when we measure equilibrium atomic density profiles.

IV. COMPRESSIBILITY MEASUREMENT

A system is characterized by its equation of state. The equation of state can be expressed in different forms involving various thermodynamic variables including density, energy, pressure, temperature, and entropy. For cold-atom experiments, density, chemical potential (through the trapping potential), and temperature are directly accessible to measurement. In the weakly interacting regime, the interaction manifests itself as a perturbative term in the equation of state. Here we measure this perturbative interaction effect by measuring the derivative of density with chemical potential, the isothermal compressibility of the gas. We prepare the system at the lowest temperature, but due to heating of the cloud by molecule formation, we have to apply a correction for the measured finite temperature.

Using the experimental procedure discussed above, we prepared equilibrated clouds at various magnetic fields and measured line-of-sight integrated profiles of column density using *in situ* phase-contrast imaging [26]. The signal-to-noise ratio was improved by averaging the column density along equipotential lines (which are ellipses for the anisotropic harmonic oscillator potential). The averaging region was restricted to an axial sector of ±60° to avoid corrections due to transverse anharmonicities [27]. Three-dimensional density profiles $n(r)$ were reconstructed by applying the inverse Abel transformation to the column densities $\tilde{n}(r)$ [26].

The isothermal compressibility is obtained from a spatial derivative of $n(r)$, since in the local density approximation, the local chemical potential is $\mu = \mu_0 - m\omega^2 x^2/2$, where μ_0 is the global chemical potential and ω the trap frequency. The compressibility is defined as

$$\kappa = \frac{1}{n^2}\frac{\partial n}{\partial \mu}. \tag{1}$$

We normalize the compressibility κ by the compressibility of an ideal gas at the given density and zero temperature $\kappa_0 = \frac{n^{1/3}}{n^2}\frac{3m}{\hbar^2(6\pi^2)^{2/3}}$, and obtain the normalized compressibility

$$\tilde{\kappa} = \frac{\kappa}{\kappa_0} = \frac{\hbar^2(6\pi^2)^{2/3}}{2m}\frac{\partial n^{2/3}}{\partial \mu}. \tag{2}$$

Here n is density, and m is the atomic mass. The normalized compressibility is obtained as the slope in a plot of $n^{2/3}$ vs μ (Fig. 2). This plot is in essence the observed density profile plotted with the central region to the left and the spatial wings to the right. Experimentally, we find the slope to be constant over an extended range of the density profile. Compressibilities were determined from fits to the slope in the region of 90% to 50% of the peak density. The region near the center of the cloud was excluded since the center is singular for the inverse Abel transformation, leading to excessive noise. These compressibilities should be regarded as average values over the density range used in the fit. The uncertainty of fitting the slope to a single profile was 4.5%. By averaging the profiles obtained from 20 images, the uncertainty was improved to 1.3%.

The normalized compressibility is a function of T/T_F and $k_F a$. At finite temperature and scattering length a, T/T_F and $k_F a$ change across a single density profile because T_F and k_F depend on the local density. However, this density dependence is small near the center of the cloud. Simulated density profiles showed that the average compressibility determined in the way described above agrees to within 0.6% with the compressibility at T/T_F and $k_F a$ at the density in the center of the selected range.

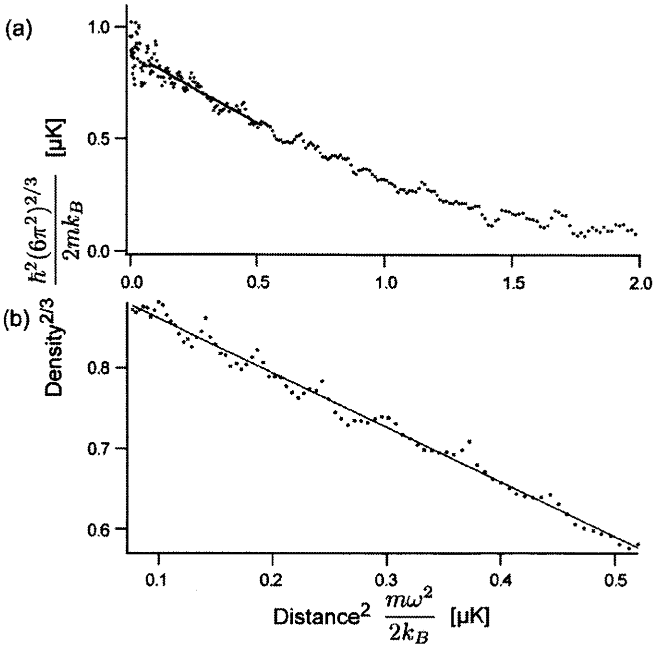

FIG. 2. Determination of the compressibility of repulsively interacting Fermi gases. The compressibility is the slope of a graph showing the density to the power 2/3 versus the square of the distance from the center. (a) Single-shot density profile. (b) Closeup of the region used for determining the compressibility for a plot showing the average of 20 density profiles.

Compressibility decreases for stronger repulsion, but also for higher temperature. To identify the effect of repulsive interaction requires a careful consideration of finite temperature effects. First, the temperature of the cloud had to be accurately determined. This can be done without any special assumptions by fitting the wings of the cloud using a virial expansion [28], by thermometry with another cotrapped atom [14], or for population imbalanced clouds by fitting the wings of the majority component which is an ideal Fermi gas [29]. Here we chose to determine temperature using a virial expansion,

$$p\frac{\lambda^3}{k_B T} = e^{\beta\mu} + b_2 e^{2\beta\mu} + O(e^{3\beta\mu}), \tag{3}$$

where $\lambda = \sqrt{\frac{2\pi\hbar^2}{mk_B T}}$ is the thermal de Broglie wavelength, b_2 is the virial coefficient, and $e^{\beta\mu}$ is the fugacity. The virial coefficient for the Fermi gas with repulsive interaction is $b_2 = -2^{-5/2} - a/\lambda$ [30]. The pressure p was obtained from the doubly integrated density profiles [13]. The temperature was determined in the wings of the profile where $\beta\mu < -0.5$. Here, the temperature measured with and without the interaction term $-a/\lambda$ in b_2 differ by about 3%. This suggests that higher-order corrections from the interaction term will be negligible. Note that the virial expansion up to second order is valid to within 1% for the ideal gas at the density of the fitted wings.

The low-temperature normalized isothermal compressibility of a noninteracting Fermi gas is given by the Sommerfeld expansion [31]

$$\tilde{\kappa}_{0,T} = 1 - \frac{\pi^2}{12}\left(\frac{T}{T_F}\right)^2 + O\left[\left(\frac{T}{T_F}\right)^4\right], \tag{4}$$

where T is the temperature and T_F is the Fermi temperature. To add the effects of interactions, it is useful to work with the inverse normalized compressibility

$$\frac{1}{\tilde{\kappa}} = \frac{3}{2}\frac{2m}{\hbar^2(6\pi^2)^{2/3}}n^{1/3}\frac{\partial\mu(n,T,a)}{\partial n}. \tag{5}$$

This is a derivative of the chemical potential, which has the following expansion in temperature and scattering length:

$$\mu(n,T,a) = E_F\left[1 - \frac{\pi^2}{12}\left(\frac{T}{T_F}\right)^2 + \frac{4}{3\pi}k_F a + \frac{4(11-2\ln 2)}{15\pi^2}(k_F a)^2\right] + CT^2a^2, \tag{6}$$

where C is a constant, independent of density [32]. Therefore the inverse normalized compressibility has additive correction terms for temperature and interactions up to the second order of the interaction effect,

$$\frac{1}{\tilde{\kappa}} = \frac{1}{\tilde{\kappa}_{0,T}} + Y(k_F a). \tag{7}$$

This equation defines $Y(k_F a)$, the interaction correction to the inverse compressibility. This term is the derivative of the interaction term of the chemical potential. In second-order perturbation theory, one obtains $Y(k_F a) = \frac{2}{\pi}k_F a + \frac{8(11-2\ln 2)}{15\pi^2}(k_F a)^2$.

Figure 3 shows the normalized compressibility, the temperature T/T_F, and the interaction correction to the inverse compressibility. The temperature increases with $k_F a$ due to the increase in three-body recombination where the binding energy of the molecules ($\hbar^2/ma^2$) is transferred to the remaining atoms. The measured temperature is higher than that in previous experiments on the repulsive side [20,21]. This difference can be explained by a smaller $k_F a$ since the increase in T/T_F is approximately proportional to $1/k_F a$ [21].

We perform a linear fit of the interaction effect $Y(k_F a)$ versus $k_F a$ (constrained to pass through the origin) and obtain 0.680 ± 0.147 for the slope, in agreement with the perturbative prediction of $\frac{2}{\pi} = 0.637$. Thus we have observed the mean-field term for repulsively interacting fermions in a thermodynamic quantity. The repulsive interaction has been seen as line shifts in rf spectroscopy experiments (which, in contrast to many thermodynamic quantities, are measured independently of the kinetic energy of the atoms) [33,34]. In principle, it is possible to obtain the mean-field term directly by fitting the density profiles with an extra mean-field term. In such fits, we obtained clear evidence for such a term, but with low accuracy. It appears that the averaging over profiles for determining the compressibility (as in Fig. 2) is superior. Figure 3(c) shows the predicted effect of the second-order term on $Y(k_F a)$. With some improvements in signal-to-noise ratio, one should be able to observe this term, which is analogous to the Lee-Huang-Yang correction for bosons.

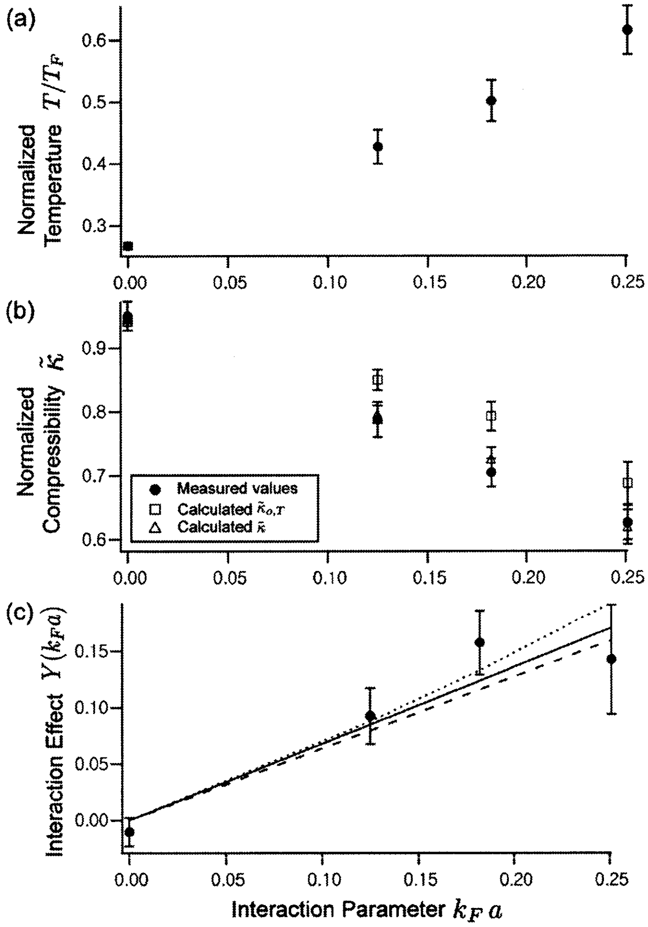

FIG. 3. Measured temperature, normalized compressibility, and interaction effect on compressibility at various interaction strengths. (a) The measured temperature as a function of interaction strength. (b) Solid circles show the measured normalized compressibility ($\tilde{\kappa}$) and open squares show the calculated normalized compressibility at the measured temperature without interaction ($\tilde{\kappa}_{0,T}$). The difference between the two indicates the effect of interaction. Open triangles show the calculated normalized compressibility using the second-order perturbation theory, which is consistent with our measured $\tilde{\kappa}$. (c) The measured interaction correction to the inverse compressibility (solid circle) is compared to a linear fit (solid line), and the first- (dashed line) and the second- (dotted line) order perturbative results.

V. DISPERSIVE EFFECT IN PHASE-CONTRAST IMAGING

As mentioned in the Introduction, phase-contrast imaging has several advantages over resonant absorption imaging, and it has been applied to many studies of cold Bose and Fermi gases [26,35,36]. Absorption imaging is usually done with absorptively dilute clouds, typically with 10% to 70% absorption (or optical densitites below 1). The standard assumption has been that dispersive imaging is quantitative when the phase shift ϕ across the cloud is less than $\pi/4$. The normalized phase-contrast signal (for negligible absorption) is $3 - 2\sqrt{2}\cos(\phi \pm \pi/4)$, which is equal to $1 \pm 2\phi$ for small phase shifts [23]. The sign depends on the laser detuning and the sign of the phase shift imparted by the phase plate.

Here, we applied phase-contrast imaging for rather precise quantitative studies of ultracold Fermi gases and found that

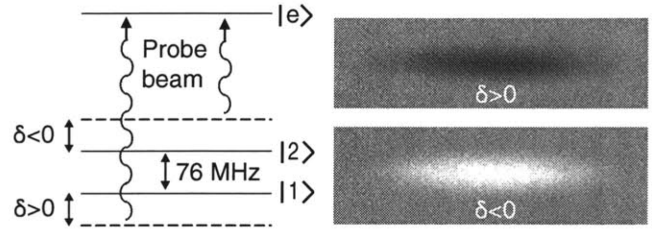

FIG. 4. Phase-contrast imaging of a balanced spin mixture in states $|1\rangle$ and $|2\rangle$. White images (phase shift $\phi > 0$) were obtained for a probe beam red detuned from the $|2\rangle \rightarrow |e\rangle$ transition, corresponding to $\delta < 0$. Black images ($\phi < 0$) were obtained for a probe beam blue detuned from the $|1\rangle \rightarrow |e\rangle$ transition, corresponding to $\delta < 0$.

even for small phase shifts systematic dispersive distortions of the image cannot be neglected. Phase-contrast imaging relies on column-density-dependent phase shifts. However, if the object is not thin, but extended along the line of sight, some lensing will affect the images. These distortions should vary in inverse proportion to the probe light detuning and become negligible for far detuning.

We investigated positive and negative detunings (δ) of 40, 80, and 120 MHz (see Fig. 4). The normalized phase-contrast image had a maximum signal of 0.35 (1.85), 0.55 (1.6), and 0.7 (1.4) for the three positive (negative) detunings. The lensing effect is opposite (focusing vs defocusing) for positive and negative detuning, and can therefore be identified by comparing profiles obtained with positive and negative detunings. Figure 5 shows that at 40 MHz, the two profiles have a visible difference, but for profiles at 80 and 120 MHz, the differences are smaller than the noise level.

However, the compressibility is determined by the slope of the profiles and very sensitive to small distortions even if they are not perceptible in the profiles. Figure 5(c) shows that, even at 120 MHz detuning, the compressibilities obtained from profiles with the two signs of the detuning differ by about 10%. Since further detuning would have resulted in a smaller signal, we evaluated the average value of the compressibility for positive and negative detuning. When the dispersive distortions are small, the effect on the compressibility should be a first-order effect in the phase shift and cancel for the average. Indeed, the average value stays constant above 80 MHz detuning. Our conclusion is that for reasonable signal levels (i.e., 50% of the baseline set by the probe light) dispersive effects are relevant for quantitative studies, but can be eliminated by performing averages over positive and negative detunings.

VI. DISCUSSION

We address now to what extent a small molecular fraction contributes to the observed density profiles. The presence of molecules is unavoidable since they form during the ramping and equilibration time. At the highest magnetic field used in the experiment, 679 G, the molecular fraction was determined to be ~10% (Fig. 1). The authors of Ref. [37] reported that molecules at 650 G showed an absorption cross section of about half the value of that of the atoms for probe light at the atomic resonance. For phase-contrast imaging with large detuning, molecules and atoms should contribute equally to the signal.

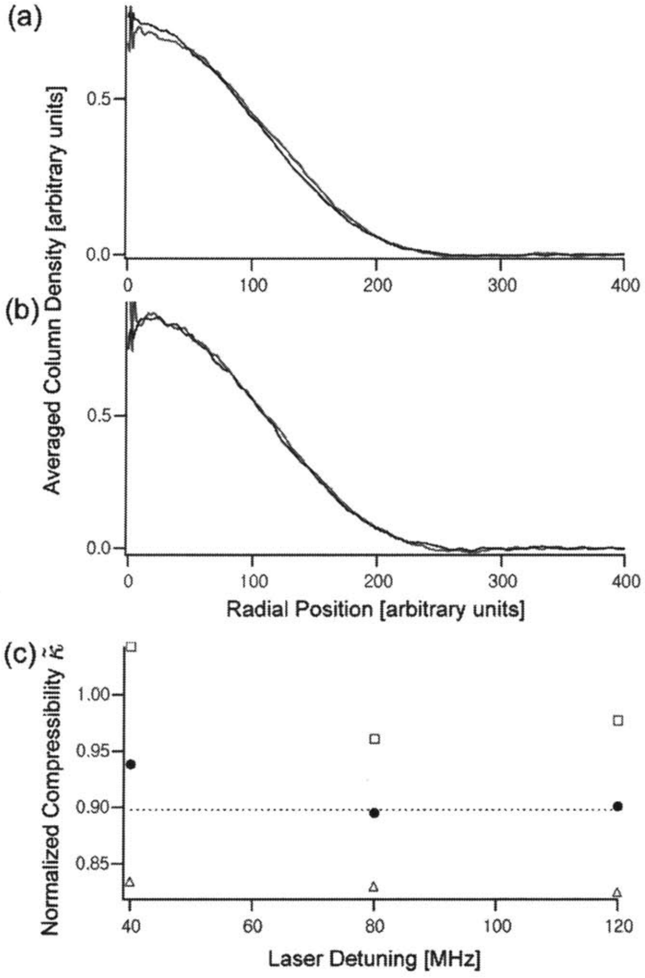

FIG. 5. Comparison of column density profiles obtained from positive and negative detunings of (a) 40 and (b) 80 MHz, respectively. (c) The measured compressibility (at $k_F a = 0$) from positive- (open triangle) and negative- (open square) detuned profiles and their averages (solid circle) are shown. The average value stays constant above 80 MHz detuning.

We performed simulations to address how the presence of molecules would affect the compressibility measurements. We considered as possible scenarios (i) that the molecular fraction is constant throughout the cloud, (ii) that the molecular fraction is proportional to the loss rate ($n^{8/3}$), and (iii) that the molecular fraction is well equilibrated at the same temperature as atoms. The atomic profile is then the difference of the measured density profile and the simulated molecular density distribution. Scenario (iii) is ruled out since it would result in a rather sharp peak in the density profile, which was not observed. The first two scenarios with a 10% molecular fraction resulted in a value for the normalized compressibility which was increased by 3.3% and 4.4%, respectively. This shows that for our largest value of $k_F a$ the presence of molecules starts to become a systematic effect. In addition to the contribution to the density profiles, molecules can affect the atomic density distribution through atom-molecule interactions.

Our work shows that the interaction effect on the compressibility at the maximum possible values of $k_F a$ is about 15%. We could identify this effect only by careful thermometry (to distinguish it from thermal effects) and by correcting small dispersive distortions of the cloud. It is desirable to study fermions for stronger repulsive interactions where stronger and nonperturbative effects are predicted. The maximum possible $k_F a$ value for obtaining equilibrium density profiles is determined by the loss rate, which is proportional to $n^2 a^6 \max(T,T_F) = (k_F a)^6 n^{2/3}$ [38,39]. Therefore, the maximum possible $k_F a$ for a given loss rate is proportional to $n^{-1/9}$ and stronger interaction effects can be seen at lower density. This should be accomplished by reducing the radial confinement and not the axial confinement which determines the equilibration time. However, the weak density dependence will allow only modest increases in $k_F a$. A recent experiment used a density ten times smaller than ours [21] and reported ramping from $k_F^0 a = 0$ to $k_F^0 a = 0.35$ in 500 ms, losing only 5% of the atoms. Assuming the loss happened during the last 50 ms, we can roughly estimate a loss rate of $\sim 0.001\ \mathrm{ms}^{-1}$ at $k_F^0 a = 0.3$, which is lower than our measurement, consistent with the lower density.

Longer lifetimes for a given $k_F a$ should be realized using narrow instead of broad Feshbach resonances. For narrow Feshbach resonances the low-lying molecular state has a dominant closed-channel character. Therefore, three-body recombination of atoms (which are in the open channel) has a smaller overlap to the molecular state and therefore a reduced loss rate. Recent experiments using rf spectroscopy [40,41] confirm this. However, for such narrow resonances the zero-range approximation is no longer valid; the interaction is no longer described by the scattering length alone and becomes (through an effective range parameter) momentum dependent. As a result, the narrow Feshbach resonances realize a different Hamiltonian.

In conclusion, in this paper we have addressed the question to what extent Fermi gases with strong interactions can be studied by observing equilibrium density profiles. The range of sufficiently long metastability to reach equilibrium is limited to values of $k_F a < 0.25$. In this range, interaction effects are comparable to thermal effects, but we were able to observe how interactions reduce the compressibility and obtained quantitative agreement with the first-order mean-field term. An observation of the second-order Lee-Huang-Yang correction is within experimental reach.

If experiments can be performed at stronger interactions, a natural extension of our work would be a measurement of the spin susceptibility using population-imbalanced Fermi systems. This was performed recently for fermions with attractive interactions [15]. Such measurements could address the possible existence of a ferromagnetic transition in a repulsive Fermi gas [20] for which the spin susceptibility would diverge at the phase transition [42].

ACKNOWLEDGMENTS

This work was supported by the NSF and ONR, an AFOSR MURI grant, and by ARO Grant No. W911NF-07-1-0493 with funds from the DARPA Optical Lattice Emulator program. Y.-R.L. acknowledges support from the Samsung Scholarship. T.T.W. acknowledges support from NSERC. We are thankful to David E. Pritchard, Christophe Salomon, Christian Sanner, Ariel Sommer, Mark Ku, and Martin Zwierlein for valuable discussions, and Gregory Lau for experimental assistance.

---

[1] W. Ketterle and M. W. Zwierlein, in *Ultracold Fermi Gases*, Proceedings of the International School of Physics Enrico Fermi, Course CLXIV, edited by M. Inguscio, W. Ketterle, and C. Salomon (IOS Press, Amsterdam, 2008).

[2] Y. I. Shin, A. Schirotzek, C. H. Schunck, and W. Ketterle, Phys. Rev. Lett. **101**, 070404 (2008).

[3] N. Navon, S. Piatecki, K. Günter, B. Rem, T. C. Nguyen, F. Chevy, W. Krauth, and C. Salomon, Phys. Rev. Lett. **107**, 135301 (2011).

[4] N. Navon, S. Nascimbene, F. Chevy, and C. Salomon, Science **328**, 729 (2010).

[5] M. J. H. Ku, A. T. Sommer, L. W. Cheuk, and M. W. Zwierlein, Science **335**, 563 (2012).

[6] M. W. Zwierlein, A. Schirotzek, C. H. Schunck, and W. Ketterle, Science **311**, 492 (2006).

[7] G. B. Partridge, W. Li, R. I. Kamar, Y.-A. Liao, and R. G. Hulet, Science **311**, 503 (2006).

[8] M. Greiner, O. Mandel, T. Esslinger, T. W. Hänsch, and I. Bloch, Nature (London) **415**, 39 (2002).

[9] I. Bloch, J. Dalibard, and W. Zwerger, Rev. Mod. Phys. **80**, 885 (2008).

[10] F. Chevy, Phys. Rev. A **74**, 063628 (2006).

[11] A. Bulgac and M. M. Forbes, Phys. Rev. A **75**, 031605 (2007).

[12] Y. I. Shin, Phys. Rev. A **77**, 041603 (2008).

[13] T.-L. Ho and Q. Zhou, Nat. Phys. **6**, 131 (2009).

[14] S. Nascimbene, N. Navon, K. Jiang, F. Chevy, and C. Salomon, Nature (London) **463**, 1057 (2010).

[15] S. Nascimbene, N. Navon, S. Pilati, F. Chevy, S. Giorgini, A. Georges, and C. Salomon, Phys. Rev. Lett. **106**, 215303 (2011).

[16] M. Horikoshi, S. Nakajima, M. Ueda, and T. Mukaiyama, Science **327**, 442 (2010).

[17] D. S. Petrov, C. Salomon, and G. V. Shlyapnikov, Phys. Rev. Lett. **93**, 090404 (2004).

[18] R. A. Duine and A. H. MacDonald, Phys. Rev. Lett. **95**, 230403 (2005).

[19] E. Stoner, Philos. Mag. **15**, 1018 (1933).

[20] G.-B. Jo, Y.-R. Lee, J.-H. Choi, C. A. Christensen, T. H. Kim, J. H. Thywissen, D. E. Pritchard, and W. Ketterle, Science **325**, 1521 (2009).

[21] C. Sanner, E. J. Su, W. Huang, A. Keshet, J. Gillen, and W. Ketterle, arXiv:1108.2017 [Phys. Rev. Lett. (to be published)].

[22] D. Pekker, M. Babadi, R. Sensarma, N. Zinner, L. Pollet, M. W. Zwierlein, and E. Demler, Phys. Rev. Lett. **106**, 050402 (2011).

[23] W. Ketterle, D. Durfee, and D. Stamper-Kurn, in *Bose-Einstein Condensation in Atomic Gases*, Proceedings of the International School of Physics Enrico Fermi, Course CXL, edited by M. Inguscio, S. Stringari, and C. E. Wieman (IOS Press, Amsterdam, 1999).

[24] Z. Hadzibabic, S. Gupta, C. A. Stan, C. H. Schunck, M. W. Zwierlein, K. Dieckmann, and W. Ketterle, Phys. Rev. Lett. **91**, 160401 (2003).

[25] M. W. Zwierlein, C. A. Stan, C. H. Schunck, S. M. F. Raupach, S. Gupta, Z. Hadzibabic, and W. Ketterle, Phys. Rev. Lett. **91**, 250401 (2003).

[26] Y. Shin, M. W. Zwierlein, C. H. Schunck, A. Schirotzek, and W. Ketterle, Phys. Rev. Lett. **97**, 030401 (2006).

[27] Y. Shin, C. H. Schunck, A. Schirotzek, and W. Ketterle, Nature (London) **451**, 689 (2008).

[28] A. Sommer, M. Ku, G. Roati, and M. W. Zwierlein, Nature (London) **472**, 201 (2011).

[29] M. W. Zwierlein, C. H. Schunck, A. Schirotzek, and W. Ketterle, Nature (London) **442**, 54 (2006).

[30] T. D. Lee and C. N. Yang, Phys. Rev. **116**, 25 (1959).

[31] A. Sommerfeld, Z. Phys. **47**, 43 (1928).

[32] R. K. Pathria and M. P. Kawatra, Prog. Theor. Phys. **27**, 638 (1962).

[33] S. Gupta, Z. Hadzibabic, M. W. Zwierlein, C. A. Stan, K. Dieckmann, C. H. Schunck, E. G. M. van Kempen, B. J. Verhaar, and W. Ketterle, Science **300**, 1723 (2003).

[34] C. A. Regal and D. S. Jin, Phys. Rev. Lett. **90**, 230404 (2003).

[35] M. R. Andrews, C. G. Townsend, H.-J. Miesner, D. S. Durfee, D. M. Kurn, and W. Ketterle, Science **275**, 637 (1997).

[36] D. M. Stamper-Kurn, H.-J. Miesner, S. Inouye, M. R. Andrews, and W. Ketterle, Phys. Rev. Lett. **81**, 500 (1998).

[37] M. Bartenstein, A. Altmeyer, S. Riedl, S. Jochim, C. Chin, J. H. Denschlag, and R. Grimm, Phys. Rev. Lett. **92**, 120401 (2004).

[38] D. S. Petrov, Phys. Rev. A **67**, 010703 (2003).

[39] J. P. D'Incao and B. D. Esry, Phys. Rev. Lett. **94**, 213201 (2005).

[40] C. Kohstall, M. Zaccanti, M. Jag, A. Trenkwalder, P. Massignan, G. M. Bruun, F. Schreck, and R. Grimm, arXiv:1112.0020.

[41] E. L. Hazlett, Y. Zhang, R. W. Stites, and K. M. O'Hara, Phys. Rev. Lett. **108**, 045304 (2012).

[42] A. Recati and S. Stringari, Phys. Rev. Lett. **106**, 080402 (2011).

Bibliography

[1] J. R. Abo-Shaeer, C. Raman, J. M. Vogels, and W. Ketterle. Observation of vortex lattices in bose-einstein condensates. *Science*, 292(5516):476–479, 2001.

[2] M.H. Anderson, J.R. Ensher, M.R. Matthews, C.E. Wieman, and E.A. Cornell. Observation of bose-einstein condensation in a dilute atomic vapor. *science*, 269(5221):198–201, 1995.

[3] M. R. Andrews, C. G. Townsend, H.-J. Miesner, D. S. Durfee, D. M. Kurn, and W. Ketterle. Observation of interference between two bose condensates. *Science*, 275(5300):637–641, 1997.

[4] M. Bartenstein, A. Altmeyer, S. Riedl, S. Jochim, C. Chin, J. Hecker Denschlag, and R. Grimm. Crossover from a molecular bose-einstein condensate to a degenerate fermi gas. *Phys. Rev. Lett.*, 92:120401, Mar 2004.

[5] Ilya Berdnikov, P. Coleman, and Steven H. Simon. Itinerant ferromagnetism in an atom trap. *Phys. Rev. B*, 79:224403, Jun 2009.

[6] J. Billy, V. Josse, Z. Zuo, A. Bernard, B. Hambrecht, P. Lugan, D. Clément, L. Sanchez-Palencia, P. Bouyer, and A. Aspect. Direct observation of anderson localization of matter waves in a controlled disorder. *Nature*, 453(7197):891–894, 2008.

[7] I. Bloch, TW Hänsch, and T. Esslinger. Measurement of the spatial coherence of a trapped bose gas at the phase transition. *Nature*, 403(6766):166–170, 1900.

[8] Immanuel Bloch, Jean Dalibard, and Wilhelm Zwerger. Many-body physics with ultracold gases. *Rev. Mod. Phys.*, 80:885–964, Jul 2008.

[9] S.N. Bose. Plancks gesetz und lichtquantenhypothese. *Z. phys*, 26(3):178, 1924.

[10] Aurel Bulgac and Michael McNeil Forbes. Zero-temperature thermodynamics of asymmetric fermi gases at unitarity. *Phys. Rev. A*, 75:031605, Mar 2007.

[11] S.Y. Chang, M. Randeria, and N. Trivedi. Ferromagnetism in the upper branch of the feshbach resonance and the hard-sphere fermi gas. *Proceedings of the National Academy of Sciences*, 108(1):51–54, 2011.

[12] F. Chevy. Universal phase diagram of a strongly interacting fermi gas with unbalanced spin populations. *Phys. Rev. A*, 74:063628, Dec 2006.

[13] Ananth P. Chikkatur. *Colliding and Moving Bose-Einstein Condensates: Studies of superfluidity and optical tweezers for condensate transport.* PhD thesis, Massachusetts Institute of Technology, 2011.

[14] Caleb A Christensen. *Ultracold Molecules from Ultracold Atoms: Interactions in Sodium and Lithium Gas.* PhD thesis, Massachusetts Institute of Technology, 2011.

[15] G. J. Conduit and B. D. Simons. Repulsive atomic gas in a harmonic trap on the border of itinerant ferromagnetism. *Phys. Rev. Lett.*, 103:200403, Nov 2009.

[16] KB Davis, M.O. Mewes, M.R. Andrews, NJ Van Druten, DS Durfee, DM Kurn, and W. Ketterle. Bose-einstein condensation in a gas of sodium atoms. *Physical Review Letters*, 75(22):3969–3973, 1995.

[17] B. DeMarco and DS Jin. Onset of fermi degeneracy in a trapped atomic gas. *Science*, 285(5434):1703–1706, 1999.

[18] J. P. D'Incao and B. D. Esry. Scattering length scaling laws for ultracold three-body collisions. *Phys. Rev. Lett.*, 94:213201, Jun 2005.

[19] R. A. Duine and A. H. MacDonald. Itinerant ferromagnetism in an ultracold atom fermi gas. *Phys. Rev. Lett.*, 95(23):230403, Nov 2005.

[20] W. D. Phillips E. Arimondo and F. Strumia (editors). *Laser Manipulation of Atoms and Ions, Proceedings of the International School of Physics "Enrico Fermi", Course CXVIII.* IOS Press, Amsterdam, 1992.

[21] A. Einstein. *Quantentheorie des einatomigen idealen Gases.* Akademie der Wissenshaften, in Kommission bei W. de Gruyter, 1924.

[22] R.P. Feynman. Simulating physics with computers. *International journal of theoretical physics*, 21(6):467–488, 1982.

[23] M. Greiner, O. Mandel, T. Esslinger, T. W. Hänsch, and I. Bloch. Quantum phase transition from a superfluid to a mott insulator in a gas of ultracold atoms. *Nature*, 415(6867):39–44, 2002.

[24] S. Gupta, Z. Hadzibabic, M. W. Zwierlein, C. A. Stan, K. Dieckmann, C. H. Schunck, E. G. M. van Kempen, B. J. Verhaar, and W. Ketterle. Radio-frequency spectroscopy of ultracold fermions. *Science*, 300(5626):1723–1726, 2003.

[25] Zoran Hadzibabic. *Studies of a Quantum Degenerate Fermionic Lithium Gas.* PhD thesis, Massachusetts Institute of Technology, 2003.

[26] E. L. Hazlett, Y. Zhang, R. W. Stites, and K. M. O'Hara. Realization of a resonant fermi gas with a large effective range. *Phys. Rev. Lett.*, 108:045304, Jan 2012.

[27] Tin-Lun Ho and Q. Zhou. Obtaining the phase diagram and thermodynamic quantities of bulk systems from the densities of trapped gases. *Nature Physics*, 6(2):131–134, 2009.

[28] Munekazu Horikoshi, Shuta Nakajima, Masahito Ueda, and Takashi Mukaiyama. Measurement of universal thermodynamic functions for a unitary fermi gas. *Science*, 327(5964):442–445, 2010.

[29] K. Homann N. Kallay I. Mills, T. Cvitas and K. Kuchitsu. *Quantities, Units and Symbols in Physical Chemistry.* Blackwell Scientific Publications, Oxford, 1988.

[30] Gyu-Boong Jo. *Quantum Coherence and Magnetism in Bosonic and Fermionic Gases of Ultracold Atoms.* PhD thesis, Massachusetts Institute of Technology, 2009.

[31] Gyu-Boong Jo, Ye-Ryoung Lee, Jae-Hoon Choi, Caleb A. Christensen, Tony H. Kim, Joseph H. Thywissen, David E. Pritchard, and Wolfgang Ketterle. Itinerant ferromagnetism in a fermi gas of ultracold atoms. *Science*, 325(5947):1521–1524, 2009.

[32] J. A. Kaeck. Electron-spin susceptibilities of the liquid binary alkali metal alloys. *Physical Review*, 175:897, 1968.

[33] W. Ketterle, DS Durfee, and DM Stamper-Kurn. *Bose-Einstein condensation in atomic gases, Proceedings of the International School of Physics "Enrico Fermi", Course CXL.* IOS Press, Amsterdam, 1999.

[34] W. Ketterle and M. W. Zwierlein. *Ultracold Fermi Gases, Proceedings of the International School of Physics Enrico Fermi, Course CLXIV.* IOS Press, Amsterdam, 2008.

[35] C. Kohstall, M. Zaccanti, M. Jag, A. Trenkwalder, P. Massignan, G. M. Bruun, F. Schreck, and R. Grimm. Metastability and coherence of repulsive polarons in a strongly interacting fermi mixture. *e-print arXiv:1112.0020 [cond-mat.quantgas]*, 2011.

[36] Mark J. H. Ku, Ariel T. Sommer, Lawrence W. Cheuk, and Martin W. Zwierlein. Revealing the superfluid lambda transition in the universal thermodynamics of a unitary fermi gas. *Science*, 335:563, 2012.

[37] L. J. LeBlanc, J. H. Thywissen, A. A. Burkov, and A. Paramekanti. Repulsive fermi gas in a harmonic trap: Ferromagnetism and spin textures. *Phys. Rev. A*, 80:013607, Jul 2009.

[38] T. D. Lee and C. N. Yang. Many-body problem in quantum mechanics and quantum statistical mechanics. *Phys. Rev.*, 105(3):1119–1120, Feb 1957.

[39] T. D. Lee and C. N. Yang. Many-body problem in quantum statistical mechanics. ii. virial expansion for hard-sphere gas. *Phys. Rev.*, 116:25–31, Oct 1959.

[40] Ye-Ryoung Lee, Myoung-Sun Heo, Jae-Hoon Choi, Tout T. Wang, Caleb A. Christensen, Timur M. Rvachov, and Wolfgang Ketterle. Compressibility of an ultracold fermi gas with repulsive interactions. *Phys. Rev. A*, 85:063615, Jun 2012.

[41] K. W. Madison, F. Chevy, W. Wohlleben, and J. Dalibard. Vortex formation in a stirred bose-einstein condensate. *Phys. Rev. Lett.*, 84:806–809, Jan 2000.

[42] M. R. Matthews, B. P. Anderson, P. C. Haljan, D. S. Hall, C. E. Wieman, and E. A. Cornell. Vortices in a bose-einstein condensate. *Phys. Rev. Lett.*, 83:2498–2501, Sep 1999.

[43] Peter J. Mohr, Barry N. Taylor, and David B. Newell. Codata recommended values of the fundamental physical constants: 2006. *Rev. Mod. Phys.*, 80:633–730, Jun 2008.

[44] S. Nascimbene, N. Navon, KJ Jiang, F. Chevy, and C. Salomon. Exploring the thermodynamics of a universal fermi gas. *Nature*, 463(7284):1057–1060, 2010.

[45] S. Nascimbene, N. Navon, S. Pilati, F. Chevy, S. Giorgini, A. Georges, and C. Salomon. Fermi-liquid behavior of the normal phase of a strongly interacting gas of cold atoms. *Phys. Rev. Lett.*, 106(21):215303, May 2011.

[46] N. Navon, S. Nascimbene, F. Chevy, and C. Salomon. The equation of state of a low-temperature fermi gas with tunable interactions. *Science*, 328(5979):729–732, 2010.

[47] Nir Navon, Swann Piatecki, Kenneth Günter, Benno Rem, Trong Canh Nguyen, Frédéric Chevy, Werner Krauth, and Christophe Salomon. Dynamics and thermodynamics of the low-temperature strongly interacting bose gas. *Phys. Rev. Lett.*, 107:135301, Sep 2011.

[48] Guthrie B. Partridge, Wenhui Li, Ramsey I. Kamar, Yean-An Liao, and Randall G. Hulet. Pairing and phase separation in a polarized fermi gas. *Science*, 311(5760):503–505, 2006.

[49] R. K. Pathria and Paul D. Beale. *Statistical Mechanics.* Academic Press, 1972.

[50] R. K. Pathria and M. P. Kawatra. Quantum statistical mechanics of a many-body system with square-well interaction. *Prog. Theor. Phys.*, 27(4):638, 1962.

[51] David Pekker, Mehrtash Babadi, Rajdeep Sensarma, Nikolaj Zinner, Lode Pollet, Martin W. Zwierlein, and Eugene Demler. Competition between pairing and ferromagnetic instabilities in ultracold fermi gases near feshbach resonances. *Phys. Rev. Lett.*, 106:050402, 2011.

[52] D. S. Petrov. Three-body problem in fermi gases with short-range interparticle interaction. *Phys. Rev. A*, 67(1):010703, Jan 2003.

[53] S. Pilati, G. Bertaina, S. Giorgini, and M. Troyer. Itinerant ferromagnetism of a repulsive atomic fermi gas: A quantum monte carlo study. *Physical review letters*, 105(3):30405, 2010.

[54] Alessio Recati and Sandro Stringari. Spin fluctuations, susceptibility, and the dipole oscillation of a nearly ferromagnetic fermi gas. *Phys. Rev. Lett.*, 106(8):080402, Feb 2011.

[55] C. A. Regal and D. S. Jin. Measurement of positive and negative scattering lengths in a fermi gas of atoms. *Phys. Rev. Lett.*, 90:230404, Jun 2003.

[56] G. Roati, C. DErrico, L. Fallani, M. Fattori, C. Fort, M. Zaccanti, G. Modugno, M. Modugno, and M. Inguscio. Anderson localization of a non-interacting bose–einstein condensate. *Nature*, 453(7197):895–898, 2008.

[57] C. Sanner, E. J. Su, W. Huang, A. Keshet, J. Gillen, and W. Ketterle. Correlations and pair formation in a repulsively interacting fermi gas. *e-print arXiv:1108.2017 [cond-mat.quantgas]*, 2011.

[58] Sheldon Schultz and Gerald Dunifer. Observation of spin waves in sodium and potassium. *Phys. Rev. Lett.*, 18:283, 1967.

[59] R. T. Schumacher and W. E. Vehse. The paramagnetic susceptibility of sodium metal. *J. Phys. Chem. Solids*, 24:297–307, 1963.

[60] Robert T. Schumacher and Charles P. Slichter. Electron spin paramagnetism of lithium and sodium. *Physical Review*, 101:58, 1956.

[61] Y. Shin. Determination of the equation of state of a polarized fermi gas at unitarity. *Phys. Rev. A*, 77(4):041603, Apr 2008.

[62] Y. Shin, Andre Schirotzek, Christian H. Schunck, and Wolfgang Ketterle. Realization of a strongly interacting bose-fermi mixture from a two-component fermi gas. *Phys. Rev. Lett.*, 101:070404, 2008.

[63] Y. Shin, C. H. Schunck, A. Schirotzek, and W. Ketterle. Phase diagram of a two-component fermi gas with resonant interactions. *Nature*, 451(7179):689–693, 2008.

[64] Y. Shin, M. W. Zwierlein, C. H. Schunck, A. Schirotzek, and W. Ketterle. Observation of phase separation in a strongly interacting imbalanced fermi gas. *Phys. Rev. Lett.*, 97:030401, Jul 2006.

[65] Inti Sodemann, D. A. Pesin, and A. H. MacDonald. Density, spin, and pairing instabilities in polarized ultracold fermi gases. *Phys. Rev. A*, 85:033628, Mar 2012.

[66] T. Sogo and H. Yabu. Collective ferromagnetism in two-component fermi-degenerate gas trapped in a finite potential. *Phys. Rev. A*, 66:043611, Oct 2002.

[67] A. Sommer, M. Ku, G. Roati, and M. W. Zwierlein. Universal spin transport in a strongly interacting fermi gas. *Nature*, 472(7342):201–204, 2011.

[68] A. Sommerfeld. Zur elektronen theorie der metalle auf grund der fermischen statistik. *Z Phys*, 47:43, 1928.

[69] D. M. Stamper-Kurn, H.-J. Miesner, S. Inouye, M. R. Andrews, and W. Ketterle. Collisionless and hydrodynamic excitations of a bose-einstein condensate. *Phys. Rev. Lett.*, 81:500–503, Jul 1998.

[70] E.C. Stoner. Lxxx. atomic moments in ferromagnetic metals and alloys with non-ferromagnetic elements. *The London, Edinburgh, and Dublin Philosophical Magazine and Journal of Science*, 15(101):1018–1034, 1933.

[71] Shizhong Zhang, Hsiang-hsuan Hung, and Congjun Wu. Proposed realization of itinerant ferromagnetism in optical lattices. *Phys. Rev. A*, 82:053618, Nov 2010.

[72] Wilhelm Zwerger. Itinerant ferromagnetism with ultracold atoms. *Science*, 325(5947):1507–1509, 2009.

[73] M. W. Zwierlein, C. H. Schunck, A. Schirotzek, and W. Ketterle. Direct observation of the superfluid phase transition in ultracold fermi gases. *Nature*, 442(7098):54–58, 2006.

[74] M. W. Zwierlein, C. A. Stan, C. H. Schunck, S. M. F. Raupach, S. Gupta, Z. Hadzibabic, and W. Ketterle. Observation of bose-einstein condensation of molecules. *Phys. Rev. Lett.*, 91:250401, Dec 2003.

[75] Martin W. Zwierlein, Andre Schirotzek, Christian H. Schunck, and Wolfgang Ketterle. Fermionic superfluidity with imbalanced spin populations. *Science*, 311(5760):492–496, 2006.